Spring 1-1-2016

Roll-To-Roll Atomic Layer Deposition of Ultrabarriers

Alexander Yersak

University of Colorado at Boulder, alye8732@colorado.edu

Roll-to-Roll Atomic Layer Deposition for Ultrabarriers

by

Alexander Yersak

B.S. Mechanical Engineering, The College of New Jersey, 2012

M.S. Mechanical Engineering, University of Colorado at Boulder, 2014

A thesis proposal submitted to the

Faculty of the Graduate School of the

University of Colorado in partial fulfillment

of the requirements for the degree of

Doctor of Philosophy

Department of Mechanical Engineering

2016

This thesis entitled:

Roll-to-Roll Atomic Layer Deposition for Ultrabarriers

written by Alexander Yersak

has been approved for the Department of Mechanical Engineering

_____

Y.C. Lee

_____

Markus Groner

_____

Steve George

_____

Ronggui Yang

_____

Kurt Maute

Date_____

The final copy of this thesis has been examined by the signatories, and we find that both the

content and the form meet acceptable presentation standards of scholarly work in the above

mentioned discipline.

Alexander Yersak (Ph.D., Mechanical Engineering, 2016)

Roll-to-Roll Atomic Layer Deposition for Ultrabarriers

Thesis directed by Professor Y.C. Lee, Dr. Markus Groner, Professor Steve George, Professor Ronggui Yang, and Professor Kurt Maute.

Abstract

Atomic layer deposition (ALD) is a bottom-up, gas phase, thin film deposition technique based on sequential, self-limiting binary surface reactions. The precise sub-nanometer film thickness control and conformal nature of this process have led to various commercial applications of ALD. However, ALD films are most commonly deposited in batch processes at low pressures, which raises throughput and/or cost concerns for many otherwise promising applications. This problem can be solved by spatial ALD (S-ALD) which is a version of the ALD technique where the precursors are separated in space rather than time. We have demonstrated the first atmospheric pressure roll-to-roll (R2R) ALD web coating system. A thickness uniformity of $\pm 2\%$ was achieved across the web. ALD cycle times as low as 76 ms were demonstrated with a web speed of 1 m/s and a vertical gap height of 0.5 mm. Extrinsic defects in the ALD films were investigated, and a predictive cluster model was proposed, and was demonstrated with a residual (i.e. difference between the actual defect counts and those predicted by the cluster model) of <10%. A R2R ALD web coating tool with molecular layer deposition (MLD) capabilities was investigated and achieved a defect density <10 /cm^2. A hyperbaric corrosion chamber with in situ monitoring of film thickness was demonstrated with the ability to characterize R2R ALD films using water dissolution as a metric. ALD SiO$_2$ films were determined to be dissolution-predictable with a predicted dissolution rate of ~3.7 nm/year at physiological temperatures. ALD TiO$_2$ films were observed with no measurable dissolution in 150 °C water over the measurement period of 12 days.

Dedication

To my family.

Acknowledgments

I would like to thank all the people who influenced me and gave me advice which made this dissertation possible.

I would like to thank my committee members Prof. Y.C. Lee, Dr. Markus Groner, Prof. Steve George, Prof. Ronggui Yang, and Prof. Kurt Maute.

I would also like to thank my current and former group members, colleagues, and contributors for their support. I would like to thank Dr. Ryan Lewis, Dr. Li-Anne Liew, Dr. Ray Wu, Dr. Biddut Bhattacharjee, Ching-Yi Lin, Collin Coolidge, Dan Kim, and Jenny Tran in Prof. Y.C. Lee's group; Dr. Daniel Higgs and Dr. Kashish Sharma in Steve George's group; Dr. Shikhar Jha and Dr. John Francis in Prof. Raj's group; Dr. Markus Groner, Dr. Robert Hall, Dr. Karen Buechler, Joe Spencer, Kassie Trujillo-Sullivan, and Chris Gump at ALD Nanosolutions; William Sin and Menno Bouman at FILMETRICS, and Dr. Natalie Veraska and Dr. Tim Porcelli at the Nanomaterials Characterization Facility University of Colorado-Boulder

Contents

Tables

Figures

Chapter 1 Introduction

1.1 Preface

1.1.1 Background and Motivation

Thin ceramic films are attractive for use as ultrabarriers against moisture permeation and/or corrosion. For example, low-cost, flexible, ultrabarriers for organic electronic devices have attracted considerable consumer attention with a projected market value reaching over ~$3 billion in 2019.[1] Examples of these organic electronics and polymeric-based devices are organic light-emitting pixels (OLEDs), organic solar cells, liquid crystal displays (LCDs), sensors, and medical and food packaging. A major concern for organic electronic technology is that the organic and metal components will experience a rapid degradation and corrosion with exposure to liquid water and/or water vapor, respectively. Degradation and corrosion is a result of the direct contact of the organic and metal components with oxygen and water moisture.[2] Hermetic, thin, glass films are an alternative moisture barrier technology for flexible and electronic devices.[3,4] Flash evaporation of metal films, such as aluminum, is another alternative moisture barrier technology, and is able to reduce the permeability of polymers by 1000 times.[5] Thin coatings comprised of inorganic and organic structures are under development. A good, thin, barrier film by ALD has the following qualities:

- Good adhesion to the substrate,[6,7]
- Optical transparency for displays,[6]
- Low temperature process for polymeric substrates,[6–9]
- Low hydrogen content,[10]
- High material density,[9]

- Featureless structure,[8]

- Good mechanical behavior (i.e. toughness),[6,11]

- Low pinhole defects,[12]

- Corrosion resistance,[6–8,11] and

- Erosion resistance.[7]

Film coating technologies produce different levels of hermetic sealing and corrosion protection, and are suitable for different moisture barrier applications as shown in Figure 1.1.
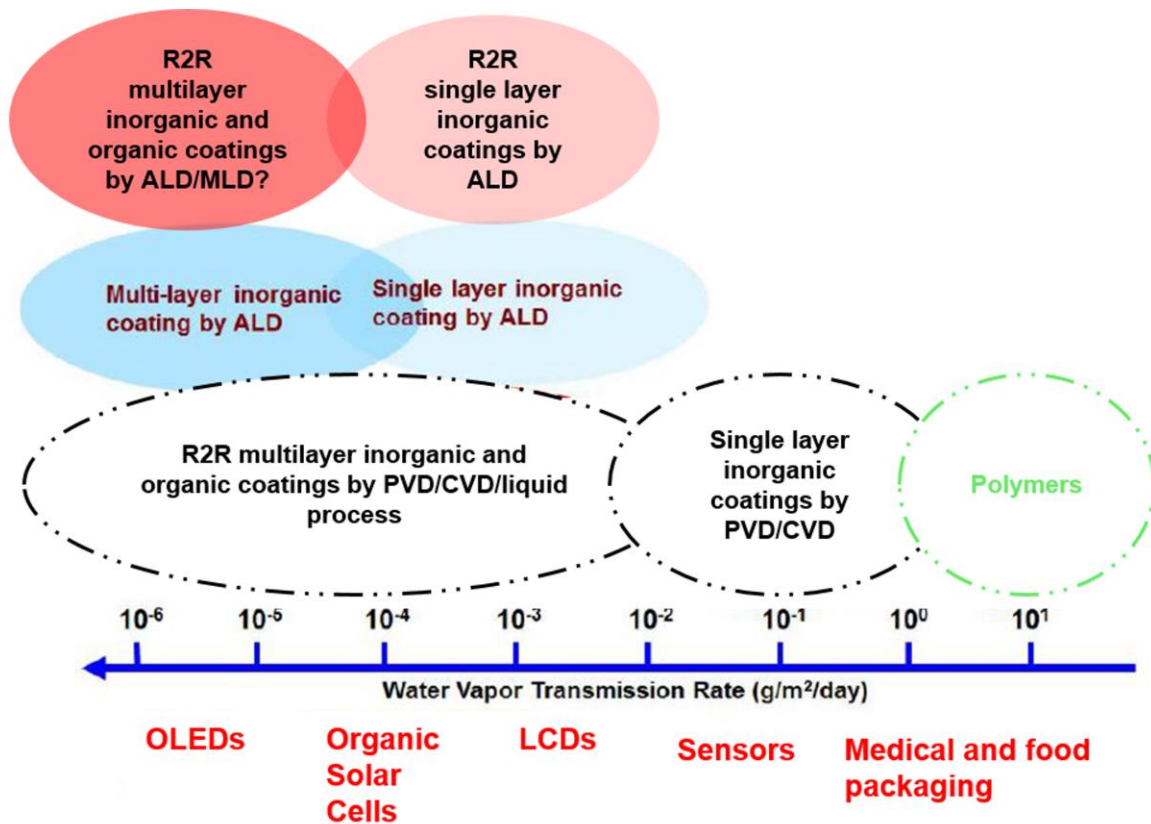
Figure 1.1. Barrier technology is shown. WVTR device requirements are based on reports by industry.[13,14] WVTR are plotted for typical polymers,[15] single-layer inorganic coatings by PVD/CVD,[6,7,16,17] R2R multilayer organic and inorganic coatings by PVD/CVD/liquid processes,[14,18–20] single-layer inorganic coatings by ALD,[21] multilayer inorganic coating by

ALD,[8,9,11,22,23] R2R single-layer inorganic coatings by ALD,[24–26] and R2R multilayer inorganic and organic coatings by ALD/MLD. Illustration and new data was modified from Zhang.[27]

For corrosion barrier applications in water, ALD thin films allow for low pinhole density[28] and a featureless conformal coating.[21,29] Other technologies such as PVD and CVD contain more defects and are not featureless.[28] Thin corrosion barriers can be used in devices such as micro/nano heat exchangers that use water as a fluid to protect thin copper metals.[30–33] ALD films are not only attractive for thin ultrabarriers against permeation and corrosion, but have played a crucial role in the development of nanodevices in general.[34]

Typically, ALD technology is considered a slow process that is intrinsically incompatible with industry standards.[35,36] To solve this problem, R2R spatial ALD systems have been developed with high throughput, up to ~1 m/s which demonstrates ALD as a manufacturable technology. Compared to conventional ALD methods, spatial R2R ALD systems have the following well known and attractive advantages:

- Continuous manufacturing process,
- No vacuum equipment if operating under atmospheric pressure conditions,[26]
- Compatible with inline web processes,
- Low-cost,
- High throughput,

A R2R ALD system is critical for the goal of delivering low-cost and manufacturable ALD coatings. As stated before, a barrier structure is required to have the following properties: Good adhesion to the substrate,[6,7] optical transparency for displays,[6] low temperature process for polymeric substrates,[6–9] low hydrogen content,[10] high material density,[9] amorphous structure,[8]

good mechanical behavior,[6,11] low pinhole defects,[12] corrosion resistance,[6–8,11] and erosion resistance.[7]

1.1.2 Problem Statement and Objectives

The purpose of this dissertation work is to investigate the feasibility of low-cost, high throughput R2R ALD coatings. This work focuses on critical issues of operating a R2R ALD system under atmospheric pressure and also focuses on critical issues of depositing a good R2R ALD barrier film. For an atmospheric pressure ALD system, we address ALD precursor carrier gas flows, web speeds, and coating uniformity. For ALD barriers, we develop new characterization tools to investigate both extrinsic and intrinsic defects in thin films.

For atmospheric pressure ALD systems with a large conductance gap, >500 μm, we investigate process gas flow rates, web speeds, and web temperatures, which are all major variables that dictate the quality and uniformity of the deposited thin film. Too fast web speeds with high purge flows will reduce the precursor residence times and growth per cycle. Mixing of the precursor gases will occur for low purge gas flows and fast web speeds. Mixing of precursor gases will produce a CVD contribution towards the total film growth per cycle. Underdosing the precursor gases may result in a low growth per cycle and non-uniformity across the web width. To understand the variables in this atmospheric pressure ALD system that affect the growth per cycle, we use a reflectometer to monitor the film thickness in situ and in real time. To address the need for future manufacturing quality control for R2R ALD web coating systems, we investigate the stability of in situ reflectometry measurements.

For barrier applications using ALD coatings, we investigated extrinsic defects in the ALD films. Extrinsic pinhole defects create short circuit pathways for permeation of water vapor and/or liquids in thin ceramic films. Extrinsic defect partial footprints are the result of faults such as small

(<1 μm) and large (>1 μm) particulates embedded in the film due to the deposition process. A random and cluster model were investigated. To attempt to suppress damaging particulates in the ALD coating, a MLD coating was investigated and used to smooth the substrate surface and arrest particulates in a thick (~1 μm) MLD film.

For barrier applications using ALD coatings, we investigate intrinsic defects in the films. Bulk permeation of moisture and/or gases through a barrier is dominant when the extrinsic pinhole defect density is negligible.[23] The following ALD reactor parameters that have the potential to affect bulk moisture and/or gas permeation and the intrinsic quality of the film are listed as: Operating pressure, substrate temperature, precursor dosing, purge gas flow, web speed, purge window, precursor window, and substrate material. We investigate the intrinsic quality of thin films using the dissolution rates of materials in liquid water as a metric. We demonstrate in situ reflectometry as a method to measure nm-scale reductions of optically transparent coatings in water.

1.1.3 Contributions and Publications

Contributions to ALD films:

- We demonstrated a ~90% reduction in extrinsic pinhole defects ($8.8/cm^2$) for ALD Al_2O_3 coating grown on a MLD polyamide coating on PEN Q51 as compared to a single ALD Al_2O_3 coating on PEN Q51 with a density of ($86.5/cm^2$) .

- We developed a hyperbaric chamber for characterization of thin film dissolution in water with in situ monitoring of film thickness using reflectometry. This tool was used to characterize the intrinsic quality of ALD films by using dissolution in water as a metric.

- We were the first to apply statistical models to extrinsic pinhole defects in ALD films on polymeric materials. Previously, defects were reported as a random defect density.

- We identified multiple faults which were particulate generation and CVD reactions in an atmospheric pressure R2R ALD system at ALD Nanosolutions.

- We demonstrated the feasibility of low-cost, high throughput atmospheric pressure R2R ALD at ALD Nanosolutions.

Peer reviewed journal publications resulting from this dissertation:

- Yersak, A.; Lewis, R.; Tran, J.; Lee, Y.-C. Characterization of Thin Film Dissolution in Water with in Situ Monitoring of Film Thickness Using Reflectometry. *ACS Appl. Mater Interfaces* **2016**.

- Yersak, A.; Lee, Y.-C. Probabilistic Distributions of Pinhole Defects in Atomic Layer Deposited Films on Polymeric Substrates. *J. Vac. Sci. Technol. A Vacuum, Surfaces, Film.* **2016**, *34*, 01A149.

- Yersak, A.; Lee, Y.-C.; Spencer, J.; Groner, M. Atmospheric Pressure Spatial Atomic Layer Deposition Web Coating with in Situ Monitoring of Film Thickness. *J. Vac. Sci. Technol. A Vacuum, Surfaces, Film.* **2014**, *32*, 01A130.

Conferences presentations resulting from this work:

- Yersak, "Defect Density Distributions in Atomic layer Deposited Films on Polymer Webs," InterPACK 2015, San Francisco, California, 2015.

- Yersak, Y. Lee, J. Spencer, M. Groner, "Design for Nanomanufacturability of Atomic Layer Deposition Process: Defect Distributions in ALD Films," ALD 2015, Portland, Oregon, 2015.

- Yersak, "Extrinsic Defect Distributions in Roll-to-Roll Atomic Layer Deposited Films on Polymers," GEARRS, University of Colorado Boulder, 2015.

- Yersak, "Enabling Technology with Roll-to-Roll Atomic Layer Deposition," GEARRS, University of Colorado Boulder, 2013.

Invention disclosures resulting from this work:

- Yersak, A; Lewis, R; Lee, Y.-C. Rapid Characterization of Thin Film Dissolution in Fluids with in Situ Monitoring of Film Thickness Using Reflectometry. 2016

Recognitions and awards resulting from this work:

- The journal article titled, Atmospheric Pressure Spatial Atomic Layer Deposition Web Coating with in Situ Monitoring of Film Thickness, was reported as one of the most read ALD articles from 2014.

- Awarded a fellowship from the Department of Mechanical Enginering at the University of Colorado Boulder in the amount of $7,056.

1.1.4 Dissertation Organization

This dissertation work is organized into five chapters. **Chapter 1** discusses the motivation, research objectives, and relevant background information for this dissertation work. The investigation of an atmospheric pressure R2R ALD system is presented in **Chapter 2**. The R2R ALD system was characterized for precursor dosing, purging, and web speeds by monitoring the film thickness in situ with spectral reflectometry. Barrier properties of the ALD films grown in this atmospheric pressure R2R system are measured. The extrinsic pinhole defect density of a conventional ALD reactor and a R2R ALD and MLD reactor was investigated in **Chapter 3**. Using statistical models, it was demonstrated that defects could be simulated over a large area ~1 m^2. **Chapter 4** investigates the dissolution and corrosion of thin films in water using in situ reflectometry to monitor film thickness reductions. Using this technique it was possible to probe the intrinsic quality of ALD films using water dissolution as a metric. Techniques developed in

this dissertation work to investigate extrinsic defects and intrinsic film quality can be applied to future work on characterizing R2R ALD and MLD coatings. **Chapter 5** summarizes the current work and suggests further studies.

1.2 Background Overview

1.2.1 Atomic Layer Deposition

As introduced in **Chapter 1.1.1,** R2R ALD is an attractive thin film deposition technology for ultrabarrier coatings because it allows for a continuous manufacturing process, compatible with inline web processes, is low-cost, and is high throughput. This section will introduce the concept of conventional and R2R ALD techniques, and will discuss the challenges of engineering a manufacturable ultrabarrier.

The ALD process is a bottom up technique which consists of sequential, self-limiting, binary surface reactions as shown in Figure 1.2. ALD Al_2O_3 surface chemistry can be described as two repeating A and B steps:

$$(\boldsymbol{A})\ AlOH^* + Al(CH_3)_2 \rightarrow AlOAl(CH_3)_2{}^* + CH_4 \tag{1.1}$$

$$(\boldsymbol{B})\ AlCH_3{}^* + H_2O \rightarrow AlOH^* + CH_4 \tag{1.2}$$

$$(\boldsymbol{Total})\ 2Al(CH_3)_3 \rightarrow Al_2O_3 + 3CH_4 \tag{1.3}$$
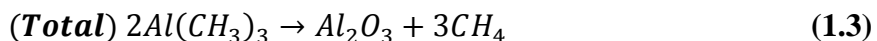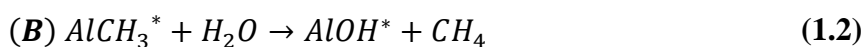
The ALD Al_2O_3 chemistry is one of the most exothermic ALD processes, and has been reported with a reaction enthalpy of -376 kcal.[37] As a result, Al_2O_3 coatings are often used as adhesion layers for other ALD chemistries.[38]
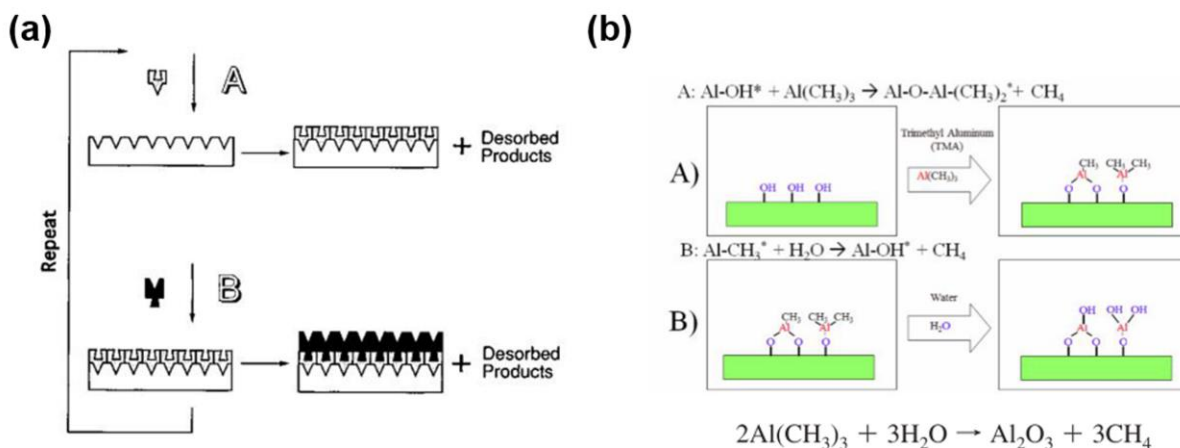
Figure 1.2 (a) Generic ALD process is shown.[39] (b) ALD Al_2O_3 process is shown.[27]

During each A and B step the ALD reaction is driven to completion and no further surface reactions will occur. Each A and B step is followed by a purge of the reaction byproducts and unreacted precursors to ensure no unwanted reactions. The bottom up growth of ALD allows for the coating of high aspect ratio structures with sub-nanometer control of the film thickness as shown in Figure 1.3.
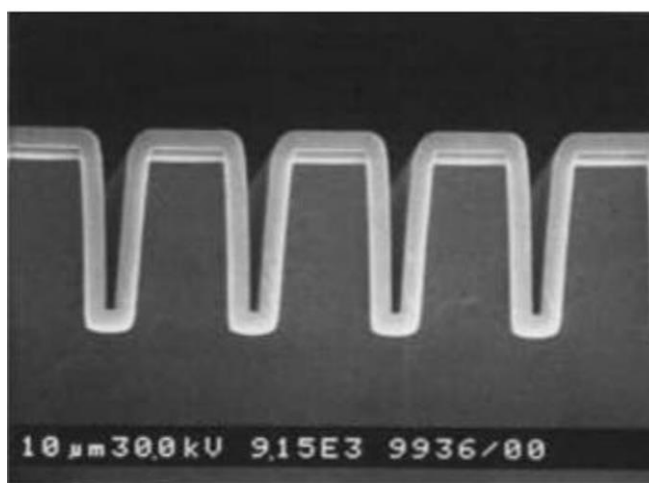
Figure 1.3. 300 nm of Al_2O_3 deposited on a Si trench structure.[40]

ALD on inert polymers (i.e. no functional surface species) is possible as shown in Figure 1.4. In the case of ALD Al_2O_3, the reaction proceeds first by TMA and water reacting in a bimolecular fashion to create $Al(OH)_4$ particle clusters inside the subsurface of the polymer material. ALD growth is achieved when the bimolecular reactions are suppressed because the TMA can no longer easily diffuse into the polymer through the nucleated thin film.
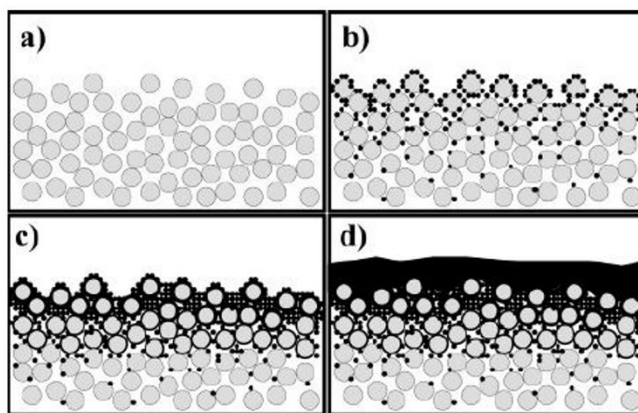
Figure 1.4. ALD on polymer concept is shown. (a) Bare polymer. (b) Bimolecular reactions are dominate. (c) Bimolecular reactions stop. (d) ALD reactions proceed.[41]

Typically, ALD films are deposited using thermally activated and/or plasma assisted conventional reactors under vacuum conditions. For slow conventional ALD processes, precursor exposures are separated by time-based precursor pulses and pumping. For a spatial ALD processes, a substrate is repeatedly translated through fixed zones of precursor separated by an inert gas curtain as shown in Figure 1.5.
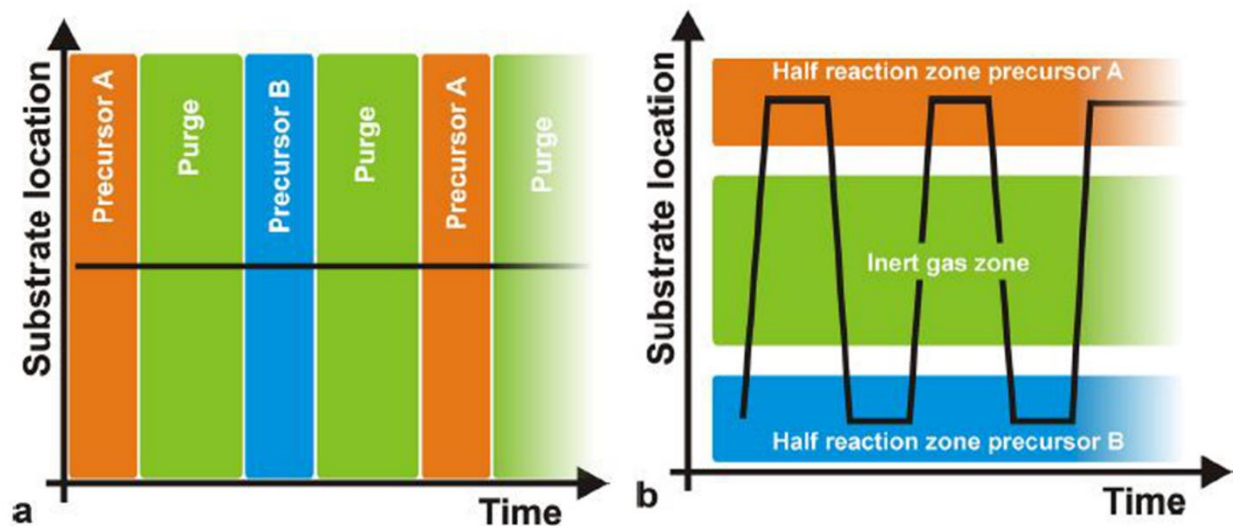
Figure 1.5. (a) Conventional ALD concept. (b) Spatial ALD concept.[36]

Spatial ALD reactor concepts are listed in Table 1.1 based on the substrate type, motion, and operational pressure. Spatial ALD reactors are designed for rigid substrates (i.e. glass and wafers) and flexible web substrates. Motion for the ALD reactors are categorized as reciprocated, spinning, translational, rotary drum, endless web, and R2R. No other web coating system operating under atmospheric pressure to date has reported WVTR values for ALD coatings on polymeric materials.

Table 1.1. Spatial ALD reactor designs are summarized.

Group	Substrate	Motion	Pressure	Comments
Eastman Kodak Company[42,43]	Glass	Reciprocating	Atm.	
UCB[44]	Wafer	Reciprocating	Atm.	
University of Cambridge[45]	Wafer	Reciprocating	Atm.	
Cambridge NanoTech[46]	Wafer, web (rigid)	Reciprocating	Atm.	
TNO[47–51]	Wafer	Spinning	Atm.	
Seoul National University[52]	Wafer	Spinning	Vac.	
Levitech/ASM[36]	Wafer	Translational	Atm.	Double gas bearing
SoLayTec/TNO[36]	Wafer	Reciprocating	Atm.	Double gas bearing
Beneq TFS 200R, ASTRaL[53,54]	Web (mounted)	Rotary drum	Vac.	
Lotus Applied Technology[24]	Web	Endless web, R2R	Vac.	Serpentine web path
Beneq WCS, ASTRaL[55]	Web	R2R	Vac.	Rocking coating head
TNO[48]	Web	R2R		Counter-rotating coating drum
ALDN/ UCB[26]	Web	Endless web	Atm.	In situ reflectometry.
UCB[56]	Web	Rotary drum, R2R	Vac.	Push-pull coating head

R2R ALD technology enables ALD hermetic coatings for low-cost devices, but has the following

disadvantages/challenges compared to conventional ALD tools as listed below:

- Web handling,[24,26,57,58]

- Mechanical surface scratching,[26,57,58]

- Surface contaminates,[26,58,59] and

- Winding,[25,26,57,59,60]

Lahtinen and coworkers[57], reported that surface contaminates and winding may reduce a thin film barrier's performance by 7-17% and ~26%, respectively.

Many spatial ALD reactors have been demonstrated with atmospheric pressure conditions as shown in Table 1.1, but none have targeted polymeric substrates. Lotus applied technology has demonstrated a web coating R2R ALD system that operated under coarse vacuum conditions, and with good barrier propertites.[24] In contrast, in this dissertation work, we investigate the feasibility of R2R ALD under atmospheric pressure. Atmospheric pressure ALD using water precursors is challenging due to the following:[61]

- Excess physisorbed water,

- Fluid boundary layer thickness,

- Product desorption,

- Product diffusivity,

- Hydroxyl concentrations in the film, and

- Purge gas velocity,

Mousa and coworkers[61] experimentally showed that increasing gas purge velocities were more effective at removing excess physisorbed water molecules than increasing N_2 purge times in a conventional atmospheric pressure ALD reactor as shown in Figure 1.6.
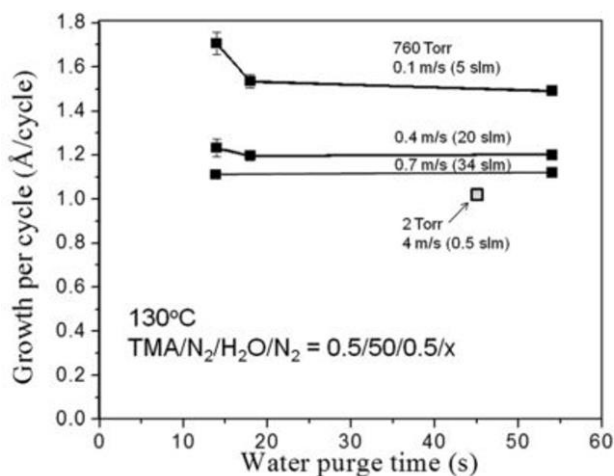
Figure 1.6. Effects of N_2 purge gas velocities and water purge times on the growth per cycle for Al_2O_3 by TMA and water under atmospheric pressure deposition conditions.[61]

The difficulty of operating a spatial ALD reaction under atmospheric pressure conditions is also illustrated in Figure 1.7 for a spatial ALD system. An increase in growth per cycle was reported for slow substrate speeds.[51]
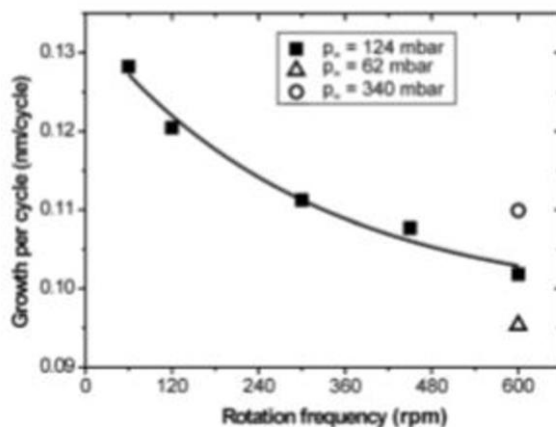
Figure 1.7. Effects of substrate speed on the growth per cycle of Al_2O_3 by TMA and water for an atmospheric pressure ALD reactor at a fixed N_2 purge velocity.[51]

In contrast, many low-pressure spatial ALD processes have not shown an increase in growth per cycle of Al_2O_3 by TMA and water. Dickey and Barrow reported no increased growth per cycle for

water Al_2O_3 using a R2R ALD system that operated at a base pressure of ~2 mbar and high N_2 flow rates of ~5 slpm as shown in Figure 1.8.[24]
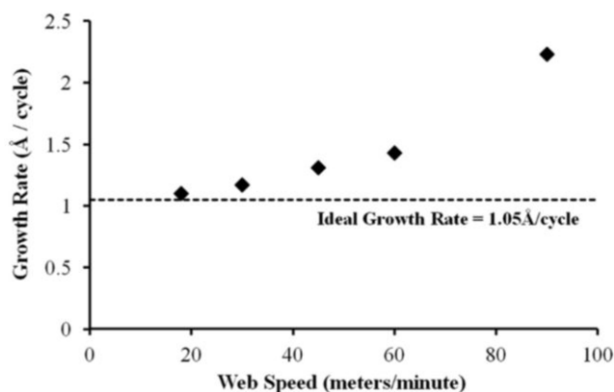
Figure 1.8. Effects of substrate speed on the growth per cycle of water Al_2O_3 for a low-pressure (~11 Torr) ALD reactor at a fixed N_2 purge velocities.[24]

A waterless spatial ALD Al_2O_3 processes using O_3 and at low processing pressures has been reported[56], and achieved no signs of increasing growth per cycle with decreasing substrate motion at a fixed N_2 purge gas velocity as shown in Figure 1.9. However, too fast web speeds above 100 rpm resulted in a decrease in the growth per cycle. Sharma[56] attributed the decrease in growth per cycle to incomplete reaction times for the ALD process to occur.
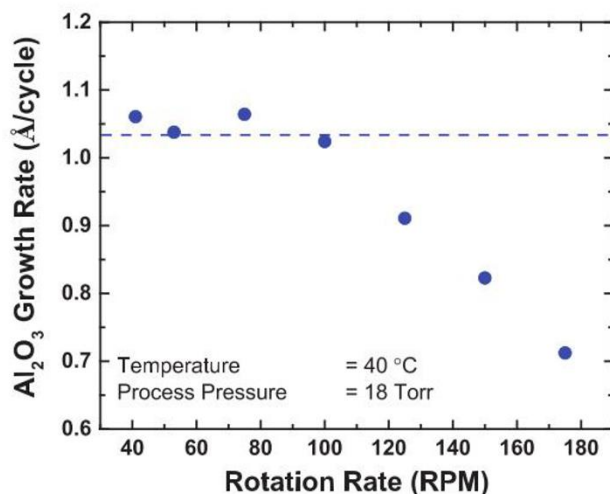
Figure 1.9. Effects of substrate speed on the growth per cycle of waterless Al_2O_3 for a low-pressure ALD reactor at a fixed N_2 purge velocities.[56]

The effects of rotation rate/web speed, process pressure, and precursors on the growth per cycle is summarized in Table 1.2. Atmospheric pressure ALD systems using water precursors show an increase in growth rate per cycle with slow webs speeds as compared to vacuum pressure ALD systems. Issues with purging excess reactants and byproducts may affect the quality of atmospheric pressure ALD films.

Table 1.2. Effects of growth per cycle on variables for atmospheric pressure and low-pressure ALD processes. A check mark, check with a plus, check with a minus indicates expected, higher than expected, and lower than expected ALD growth per cycle.

	Fast substrate motion (>1 m/s)	Slow substrate motion (<1 m/s)	Substrate motion (~1 m/s)
Atmospheric pressure (TMA and water)[26,51]	✔-	✔+	✔
Low-pressure (TMA and water)[24]	✔+	✔	✔
Low-pressure (TMA and O_3)[56]	✔-	✔	✔

Operating under atmospheric pressure is attractive for lowering the capitol and operational costs of an ALD reactor system, and can be operated at web speeds that produce an expected growth rate per cycle. However, atmospheric pressure ALD films may contain hydroxyl defects and excess adsorbed water molecules which may adversely affect barrier properties.[61] We characterize the quality of these atmospheric pressure deposited films in terms of intrinsic and extrinsic defects in this dissertation work.

1.2.2 Thin Film Moisture and Gas Barriers

In this section experimental data for water permeation of single-layer and cutting edge multilayer inorganic and organic barrier structures will be discussed. An explanation of the limitations and assumptions used for WVTR measurements will be provided. As stated in **Chapter 1.1.1**, an ultrabarrier structure is required to have the following properties: Good adhesion to the substrate,[6,7] optical transparency for displays,[6] low temperature process for polymeric substrates,[6–9] low hydrogen content,[10] high material density,[9] amorphous structure,[8] good mechanical behavior,[6,11] low pinhole defects,[12] corrosion resistance,[6–8,11] and erosion resistance.[7]

Typically, calcium sensors, coulometric sensors (i.e. MOCON), and tritium tests are used to report WVTR of barrier structures. WVTR reported in the literature for multilayer barriers do not necessarily represent equilibrium permeation rates because of long lag times.[5] Schubert and coworkers[62], determined that permeation rates measured using the electrical calcium test underestimate steady-state permeation rates when the resistance of the electrodes are not taken into account when deriving the steady-state permeation rates. Klumbies and coworkers[63] reported that the electrical calcium test, when used correctly, will produce a correct WVTR with an error of ±30%. The optical calcium test was determined to be able to provide an upper and lower bound on the WVTR depending on the calculation method used.[63] Klumbies and coworkers[63] reported that

calcium corrosion is not homogenous, which is an assumption used when calculating the WVTR using this method. The two types of Ca test methods have been reported to be able to measure to 10^{-5} g/m^2/day, and is limited by edge sealing.[62] Tritium transmission rate measurements, used to calculate WVTR, assumes all tritium diffuses through the ALD barrier film as molecular HTO, but it has been reported that atomic tritium diffusion may also occur.[22] MOCON has developed the Aquatran® Model 2 with the sensitivity to measure to 5×10^{-5} g/m^2/day using a coulometric phosphorous pentoxide coulometric sensor. As a result, care should be taken when comparing WVTR for some studies reported in this chapter.

Deposition technologies for moisture barriers can be separated into deposition processes that are comprised of series of sequential, self-limited reactions, that produce featureless films, and processes that do not. ALD and MLD processes are self-limiting deposition processes. Physical vapor deposition (PVD), chemical vapor deposition (CVD) coating processes are not. Material properties and barrier performances of thin film structures both depend on the nature of deposition process.[6] A barrier film grown by ALD has been experimentally and theoretically reported to achieve a bounded steady-state permeation rate of ~10^{-4} g/m^2/day.[5,23] Thus, it is vital to acknowledge both defect assisted permeation and bulk permeation through the films as important mechanisms.

Without any form of a barrier film, polymeric substrates are not suitable for applications requiring a WVTR lower than ~10^{-1} g/m^2/day. Typical WVTR values for polymeric materials are as shown in Table 1.3.

Table 1.3. WVTR for different polymer films.[15]

Material	WVTR (g/m^2/day) (37.8-40 ^{o}C)
Polyethylene (PE)	1.2-5.9
Polypropylene (PP)	1.5-5.9
Polystyrene (PS)	7.9-40
Poly(ethylene terephthalate) (PET)	3.9-17
PEN	14
Polyimide	7.3

PVD and CVD films deposited in single-layer structures cannot achieve barriers better than ~10^{-2} g/m^2/day because of grain boundaries, columnar structures, impurities, and pinholes in the films that make water permeation easy.[21,64,65] For food packaging and sensor applications requiring a WVTR of 10^{-1}-10^1 g/m^2/day, single-layer inorganic coatings deposited by conventional PVD/CVD batch processes are good enough. Table 1.4 lists conventional inorganic CVD and PVD barrier coatings. No barrier using single-layer PVD/CVD films has been reported to achieve WVTR values below ~10^{-2} g/m^2/day.

Table 1.4. Barrier films deposited using conventional CVD processes are organized by

individual reports as shown.[6]

Deposition process	Substrate	Precursors	Barrier structure	WVTR (g/m^2/day)
CVD and PVD[2]	OLED	Not reported	1-5 bilayers of CF$_x$ (1.8 µm)/SiN$_x$ (0.25 µm)	5×10^{-2}
PECVD[16]	Polycarbonate	SiN$_x$ (SiH$_4$, N$_2$, Ar)	SiN$_x$ (100 nm)	5×10^{-2} (38 °C, 100% RH)
PECVD[6,7]	PEN	SiN$_x$ (SiH$_4$, NH$_3$, and N$_2$)	SiN$_x$	4×10^{-2} (85 °C, 85% RH)
PECVD[6,17]	PEN	SiNx (SiH$_4$, NH$_3$, and N$_2$)	SiN$_x$ (500 nm)	3×10^{-2} (85 °C, 85% RH)
PECVD[66]	Polycarbonate	(SiH$_4$, Ar, NH$_3$, and N$_2$O)	SiO$_x$ (50 nm)/SiN$_x$ (50 nm)	1×10^{-2}

Multilayers using inorganic and organic layers are used to improve upon the limitations of single-layer barrier structures deposited using PVD and CVD. As a result, a tortuous path for permeation is created, and barriers down to ~10^{-6} g/m^2/day can be achieved due to theoretical non-equilibrium permeation (i.e. lag time in permeation).[5] Organic and inorganic multilayer structures also reduce extrinsic defects by arresting particulates in the structure as shown in Figure 1.10.
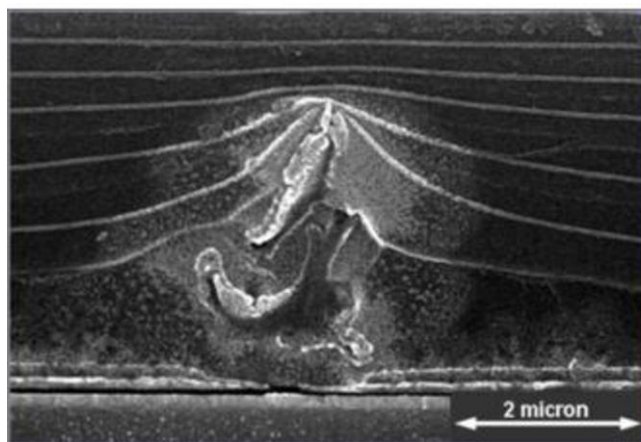
Figure 1.10. Organic and inorganic multilayer structure with arrested particulate is shown.[67]

To scale up conventional PVD, CVD batch systems, R2R operation has been used. R2R systems have been built with PVD, CVD, and liquid processes by industrial groups. These R2R processes developed by Samsung, GE, and other companies have adopted multilayer structures with organic and inorganic coatings with WVTR of 10^{-6} g/m^2/day, and listed in Table 1.5. The WVTR of the barrier coatings were thus reduced by ~4 orders of magnitude as compared to single-layer PVD and CVD films. As a result, the WVTR requirements of OLEDs of 10^{-6} g/m^2/day can be satisfied. WVTR values reported for the barrier structures may be for transient permeation rates and not steady-state permeation rates.[5]

Table 1.5. Industrial R2R PVD, CVD, liquid, and other processes for ultrabarrier films.

Group	Deposition Process	Substrate	Motion	Pressure	Barrier Structure	WVTR (g/m^2/day)
Vitex/ Samsung[20]	PVD, liquid process	PEN	Linear, R2R	Vac.	4-5 units of Al_2O_3 (~nm) and acrylic (~µm)	2.2×10^{-6} (60 °C, 90% RH)[*]
GE[18]	PECVD	Poly-carbonate	R2R	Not reported	SiOxCy and SiOxNy	10^{-5} (23 °C, 50% RH)[*]
Fraunhofer POLO[19]	PVD and liquid process	PET	R2R	Vac.	Inorganic and inorganic/ organic hybrid	$<2 \times 10^{-4}$, 8×10^{-5} (38 °C, 90% RH, 23 °C, 50% RH)[*&]
NanoGlobe Pte Ltd[14]	Not reported	Not reported	R2R?	Not reported	Oxide and nano particle multilayers	10^{-6} (60 °C, 90% RH)[*]
CKC[68]	PVD	Poly-ethersulfone (PES)	R2R	Vac.	SiON (101 nm)/Ag multilayers	$3.1 \times 10^{-2+}$

[*]Ca test, [&]MOCON Aquatran test, and [+]MOCON PERMATRAN-W test

Other techniques to deposit barrier films, such as conventional single-layer and multilayer inorganic coatings by ALD have been demonstrated with ~3 orders of magnitude reduction in WVTR as compared to single-layer CVD and PVD processes. WVTR for the conventional ALD films are listed in Table 1.6. The maximum reported WVTR was ~10^{-5} g/m^2/day, and is good enough for organic solar cell applications, but does not meet the requirements of 10^{-6} g/m^2/day.

Table 1.6. Conventional ALD and hybrid thin film processes for ultrabarrier films is shown.[6]

Deposition process	Substrate	Precursors	Barrier structure	WVTR (g/m^2/day)
PEALD[8]	PEN	Al$_2$O$_3$ (TMA, O$_2$ plasma) and TiO$_2$ (TDMAT, O$_2$ plasma	TiO$_2$ (50 nm), Al$_2$O$_3$ (50 nm), and Al$_2$O$_3$&TiO$_2$ multilayers (50 nm)	6.23×10^{-4}, 3.75×10^{-4}, and 1.81×10^{-4} (38 °C, 90% RH)*
ALD[21]	PEN	Al$_2$O$_3$ (TMA, H$_2$O)	Al$_2$O$_3$ (26 nm)	~$1\times10^{-3\&}$
ALD[11]	Ca	Al$_2$O$_3$ (TMA, H$_2$O) and ZrO$_2$ [TDMA(Zr), H$_2$O]	Al$_2$O$_3$&ZrO$_2$ multilayers (40 nm)	3.2×10^{-4} (80 °C, 80% RH)*
ALD[9]	Ca	Al$_2$O$_3$ (TMA, H$_2$O) and ZrO$_2$ [TDMA(Zr), H$_2$O]	Al$_2$O$_3$ (130 nm) and Al$_2$O$_3$&ZrO$_2$ multilayers (130 nm)	9.9×10^{-5} and 4.7×10^{-5} (70 °C, 70% RH)*
ALD[22]	Kapton	Al$_2$O$_3$ (TMA, H$_2$O) and SiO$_2$ [(*tert*-pentoxy)silanol, TMA)]	Al$_2$O$_3$ (26 nm)/SiO$_2$ (60 nm)/Al$_2$O$_3$ (26 nm)/SiO$_2$ (60 nm)	5×10^{-5} (RT, 100% RH) $^\&$
ALD, PECVD, and Spin coating[23]	Ca	Not reported	Al$_2$O$_3$&HfO$_x$ multilayers (20 nm)/ Al$_2$O$_3$ (20 nm)/SiN$_x$ (100 nm)/CYTOP (200nm)	1.89×10^{-4} (50 °C, 85% RH)*

*Ca test and $^\&$Tritium test

To scale up conventional ALD processes, R2R ALD systems with single-layer barrier films have been demonstrated. These R2R ALD systems have not achieved the WVTR levels of the R2R systems with coatings deposited by PVD, CVD, and liquid processes. The ~2 orders of magnitude higher WVTR for the R2R ALD systems as compared to the R2R PVD, CVD, and liquid processes systems, is likely due to no R2R ALD system having been reported with a multilayer structure. The low permeation rates of 10^{-6} g/m^2/day for the PVD, CVD, and liquid processes multilayer barriers may be because of steady-state conditions not being reached due to lag times in permeation because of a tortuous path mechanism for permeation.[5] The lowest WVTR reported for R2R ALD was ~10^{-4} g/m^2/day as seen in Table 1.7. A R2R ALD and MLD web coating system with organic and inorganic film deposition capabilities will be discussed in **Chapter 3**.

Table 1.7. R2R ALD and other web coating systems for ultrabarrier films are shown.

Group	Deposition Process	Substrate	Motion	Pressure	Barrier Structure	WVTR (g/m^2/day)
Lotus Applied Technology[24]	PEALD	Web (PET)	Endless web	Vac.	TiO$_2$ (20 nm)	~10^{-4} (38 °C, 90% RH) $^{\&}$
Lotus Applied Technology[24]	PEALD	Web (PET)	R2R	Vac.	TiO$_2$ (20 nm)	10^{-3} (38 °C, 90% RH) $^{\&}$
Lotus Applied Technology[25]	PEALD	Web (PET)	Endless web	Vac.	Al$_2$O$_3$ (20 nm)	10^{-3} (38 °C, 90% RH) $^{\&}$
Beneq TFS 200R, ASTRaL[53,54]	ALD	Web (mounted)	Rotary drum	Vac.		Not reported
Beneq WCS, ASTRaL[55]	ALD	Web	R2R	Vac.		Not reported
TNO[48]	ALD	Web	R2R			Not reported
ALDN/ UCB[26]	ALD	Web (PEN Q51)	Endless web	Atm.	Al$_2$O$_3$ (50 nm)	10^{-2} (37.8 °C, 100% RH) $^{\&}$
UCB[56] (ALD)	ALD	Web	Rotary drum, R2R	Vac.		Not reported

$^{\&}$MOCON Aquatran test

1.2.3 Thin Film Corrosion Barriers

In this section significant experimental dissolution rates for ALD films in water and other solutions will be discussed. Each study will be discussed separately, and a summary of the dissolution reports for ALD chemistries will be provided at the end of this section. ALD Al$_2$O$_3$, TiO$_2$, ZnO, and SiO$_2$ films have been investigated in water.[28,29,69] Dissolution mechanisms for ALD Al$_2$O$_3$, TiO$_2$, ZnO films in water have not been reported. However, a reaction pathway for SiO$_2$ dissolution in water has been proposed, and will be discussed.[70]

ALD films grown on copper were shown to decrease in thickness over time in hot water for ALD Al_2O_3, TiO_2, and ZnO as shown in Figure 1.11.[69] Abdulagatov and coworkers[69] reported that ALD Al_2O_3 and ZnO films suffer from rapid failure in terms of adequately protecting the copper surface, with surface coverage below 30% after less than 1 day in 90 °C water. ALD TiO_2 films in 90 °C water will not suffer surface coverage problems up to 80 days, which corresponded to a few nanometers of film remaining on the copper.[69]
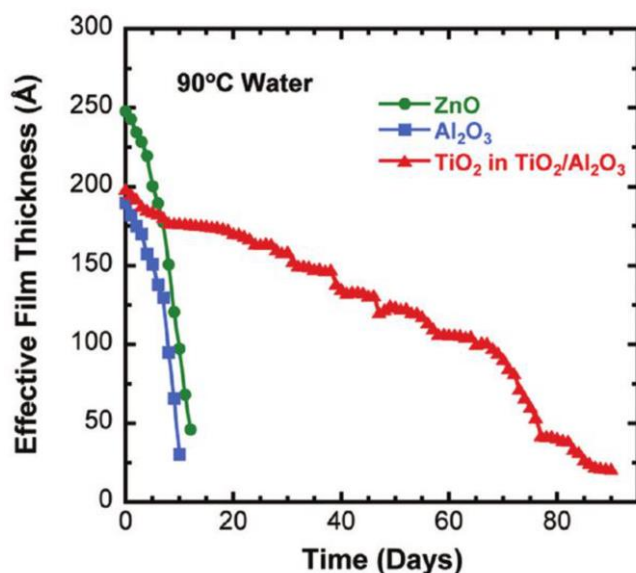
Figure 1.11 Dissolution of thin ALD TiO_2, Al_2O_3, and ZnO in water at 90 °C.[69]

ALD TiO_2 films deposited at 150 °C, were reported with no observable dissolution in water at room temperature as shown in Figure 1.12.[29] In contrast to Abdulagatov and coworkers,[69] ALD Al_2O_3 films were observed with no dissolution by Correa and coworkers.[29] Al_2O_3 films were observed to have a significant increase in refractive index,[29] which was not observed by Abdulagatov and coworkers.[69] Correa and coworkers[29] suggested that the Al_2O_3 coatings were chemically changing to gibbsite due to back-deposition.[29]
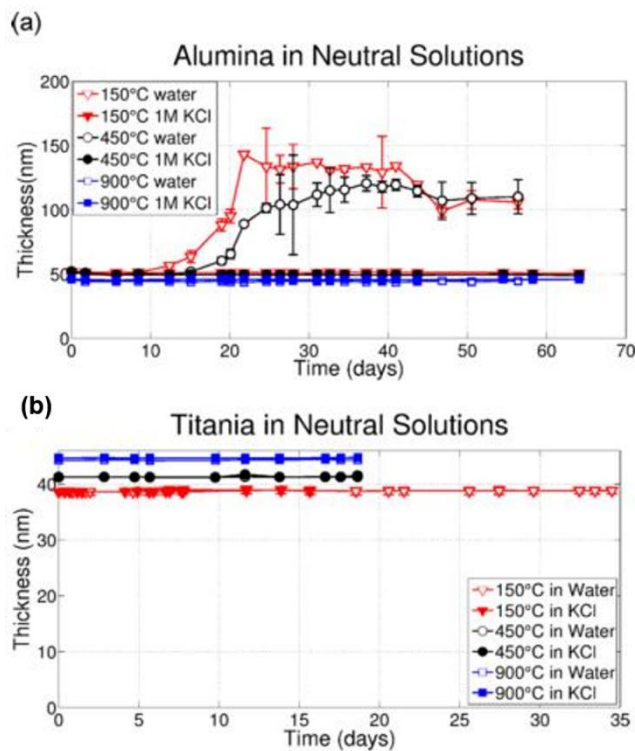
Figure 1.12. Effects of substrate deposition temperatures and annealing for (a) ALD Al_2O_3 and (b) ALD TiO_2 in room temperature water.[29]

For ALD TiO_2 films attacked in hot sulphuric acid, deposition temperatures >175 °C showed no measurable dissolution as shown in Figure 1.13.[71] Sammelselg and coworkers[71] reported that the crystallization of ALD TiO_2 films begins at ∼135-150 °C, and is likely responsible for reduced dissolution rates as compared to fast dissolution rates for low temperature amorphous films. No dependence of film thickness on the dissolution rate was observed.[71]
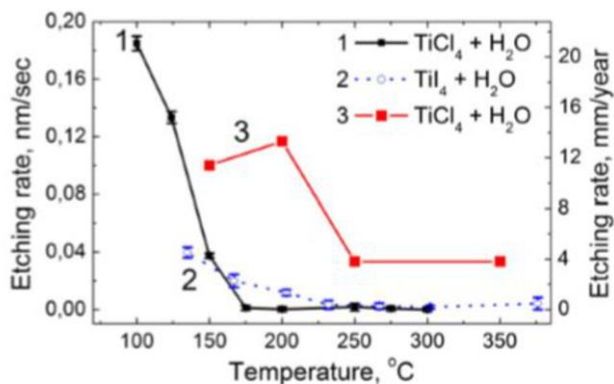
Figure 1.13. Effects of substrate deposition temperatures for ALD TiO_2 attacked in hot sulphuric acid is shown.[71]

For ALD SiO_2 films <1 nm of dissolution was observed in water at physiological temperatures for 15 days as shown in Figure 1.14.[28] Dissolution rates for SiO_2 films by other deposition techniques showed a linear dissolution rate in water.[28]
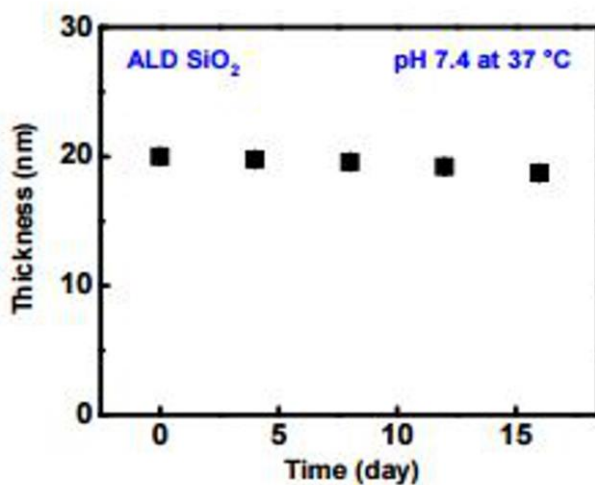
Figure 1.14. Dissolution of ALD SiO_2 in water is shown.[28]

The reaction pathway for dissolution of ALD SiO_2 in water has been reported by Leplan and coworkers, and is shown in Figure 1.15.[70]
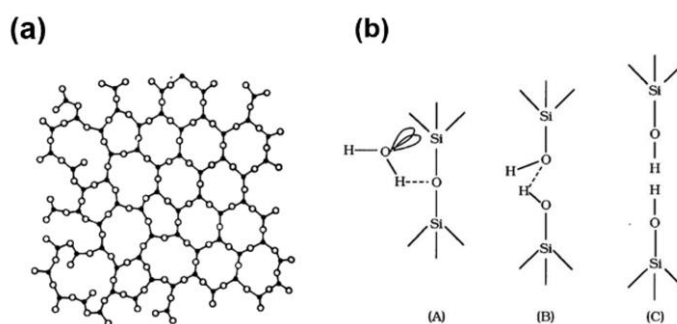
Figure 1.15. (a) Amorphous glass structure with Si (solid black circle) and O (open circle) is shown.[72] (b) Reaction pathway for dissolution of ALD SiO_2 in water is described as (A) physical adsorption of water molecules on glass surface, (B) dissociation of water molecule and reaction with glass, (C) and severance of weak hydrogen bond.[70]

Dissolution rates for the ALD Al_2O_3, TiO_2, ZnO, and SiO_2 and surface coverage qualities are summarized in Table 1.8. ALD SiO_2, TiO_2, and Al_2O_3 dissolution in water measured in this dissertation work will be discussed in **Chapter 4**. In the next chapter we will characterize atmospheric pressure ALD films.

Table 1.8. Summary of ALD films immersed in water is shown.

ALD chemistry	Dissolution rate (nm/day)	Surface coverage
Al_2O_3	~1.75 (90 °C)[69]	Poor[29,69]
ZnO	~1.6 (90 °C)[69]	Poor[69]
TiO_2	~0.19 (90 °C)[69]	Good[69]
SiO_2	0.08 (37 °C)[28]	Good[28]

Chapter 2 Atmospheric Pressure Spatial Atomic Layer Deposition Web Coating With in situ Monitoring of Film Thickness

2.1 Introduction

As previously mentioned in **Chapter 1**, atomic layer deposition (ALD) is a gas phase, thin film deposition technique based on sequential, self-limiting binary surface reactions. The precise subnanometer film thickness control and conformal nature of this process[37] have led to various commercial applications of ALD, primarily in the semiconductor industry. However, ALD films are most commonly deposited in batch processes at low-pressures, which raises throughput and/or cost concerns for many otherwise promising applications. Spatial ALD (S-ALD) is a version of the ALD technique where the precursors are separated in space rather than time. This concept was first proposed in a patent by Suntola and Antson in 1977[73]. Over the past few years, various S-ALD systems have been demonstrated for the coating of wafers as well as flexible polymer web substrates.[24,36,42–56,74] Table 2.1 summarizes the recent S-ALD studies based on the substrate type, substrate motion, and pressure. Some of these systems have been designed to operate at atmospheric pressure. However, the ALD web coating systems have been designed to operate under vacuum.[24,53–55]

In this dissertation work, a simple, low-cost atmospheric pressure ALD web coating system was developed using an in situ measurement technique to monitor film growth on a moving flexible substrate. The web coating system was arranged in an "endless web" configuration, as illustrated in Figure 2.1.

Table 2.1. Spatial ALD reactor designs are summarized.

Group	Substrate	Motion	Pressure	Comments
Eastman Kodak Company[42,43]	Glass	Reciprocating	Atm.	
UCB[44]	Wafer	Reciprocating	Atm.	
University of Cambridge[45]	Wafer	Reciprocating	Atm.	
Cambridge NanoTech[46]	Wafer, web (rigid)	Reciprocating	Atm.	
TNO[47–51]	Wafer	Spinning	Atm.	
Seoul National University[52]	Wafer	Spinning	Vac.	
Levitech/ASM[36]	Wafer	Translational	Atm.	Double gas bearing
SoLayTec/TNO[36]	Wafer	Reciprocating	Atm.	Double gas bearing
Beneq TFS 200R, ASTRaL[53,54]	Web (mounted)	Rotary drum	Vac.	
Lotus Applied Technology[24]	Web	Endless web, R2R	Vac.	Serpentine web path
Beneq WCS, ASTRaL[55]	Web	R2R	Vac.	Rocking coating head
TNO[48]	Web	R2R		Counter-rotating coating drum
ALDN/ UCB[26]	Web	Endless web	Atm.	In situ reflectometry.
UCB[56]	Web	Rotary drum, R2R	Vac.	Push-pull coating head

Figure 2.1. This diagram shows a schematic representation of the atmospheric pressure ALD web coating reactor.

Operating the system with the web in a loop [instead of in roll-to-roll (R2R) mode] allows for the deposition of thick films while employing a small coating head. The ALD coating head design was initially evaluated using computational fluid dynamics (CFD) modeling. These results indicated that operating at atmospheric pressure with a relatively large vertical gap height should be feasible. Compared to similar coating heads used in previous work,[42,44] the construction and operation of this system was significantly simplified via the omission of pumping channels.

This dissertation work demonstrated Al_2O_3 S-ALD using trimethylaluminum (TMA) and H_2O precursors on polyethylene naphthalate (PEN) substrates, deposited at atmospheric pressure and temperatures ~100 °C. The use of a spectral reflectometry technique provided an in situ measurement technique for optimizing process parameters such as web speed, nozzle configuration, precursor flow rate, coating head temperature, coating head gap height, and flexible substrate material.

The demonstration of this modular atmospheric pressure design suggests the feasibility of low capital cost scaled up ALD R2R systems. In the future, reflectometry may be used in manufacturing quality control to monitor S-ALD processes.

2.2 Experiment

2.2.1 Endless Web Coating System

The S-ALD coating system was configured in an endless web configuration, as shown in Figure 2.1. The web was fastened in a loop using longitudinal pieces of Kapton tape. The web substrate most commonly used in this dissertation work was polyethylene naphthalate (HS-PEN Q51, Dupont-Teijin) with dimensions 4m x 100mm. Polyethylene terephthalate (Melinex S200) was also used successfully as a substrate. The web tension was typically ~5–15 N, as monitored with the tension sensor in roller number 3. The web was circulated in a loop using a belt driven motor system on roller number 4. The web speed was typically 1 m/s, with a maximum web speed of 2 m/s. The edge sensor and web guide system installed on rollers 1 and 2 ensured that the web passed through the coating head with proper alignment. The ALD system was enclosed in a cabinet with clean air supplied using a high-efficiency particulate absorption filter. The air was exhausted to a chemical hood. To further minimize contaminants and scratching, the web was cleaned with isopropyl alcohol prior to deposition.

2.2.2 Modular ALD Coating Head

A modular ALD gas source head was designed using CFD modeling to deposit ALD films on a moving web substrate at atmospheric pressure. As shown in Figure 2.2, the gas source head was comprised of a series of 30 nozzles spaced 19 mm apart, with the capability to deliver precursor or purge gas as desired.
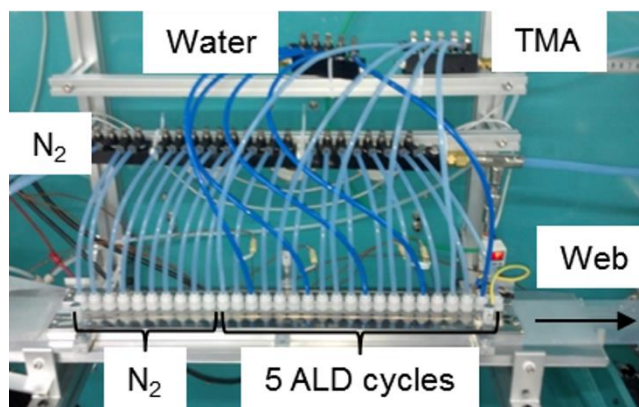
Figure 2.2. Image depicts the ALD coating head configured for five ALD cycles. As the polymer web moves from left to right, it is exposed to ten N_2 purge nozzles followed by five sets of TMA/N_2/H_2O/N_2 bands. The dark colored H_2O lines originate from a manifold on the top center, while the light colored TMA lines stem from the manifold on the top right.

The design creates parallel bands of either precursor or purge gas over the polymer web. This modular coating head could be configured for 1–5 ALD cycles. The first ten nozzles were N_2 (to allow for heating and purging) followed by sets of TMA/N_2/H_2O/N_2 bands to define the number of ALD cycles per pass. The width of each gas band was defined by one or more adjacent nozzles. The vertical gas conductance gap between the web and coating head was adjusted with micrometers. The N_2 provided a gas bearing between the coating head and polymer web. Heating elements were attached to the bottom of the coating sled and to the top of the coating head.

TMA (Aldrich, 97%) and H_2O (distilled) precursors were delivered by N_2 carrier gas flowing through each bubbler, controlled by 1 slpm mass flow controllers. The carrier gas was sourced from a liquid N_2 dewar and then dried to sub-ppb H_2O levels using a purifier filter (Entegris Gate Keeper) to minimize reaction with the TMA. This precursor/N_2 gas stream was then further diluted to match the N_2 flows/pressures of the other N_2 purge gas bands (multiple slpm each). These gas flows were directed down through the nozzles and onto the center of the moving polymer web.

Gases then flowed in across the web and out to the sides of the coating head in roughly parallel gas streams. Unlike in most other S-ALD systems, no pumping channels were used between the precursor and purge bands. This design greatly simplifies the operation of the ALD web coating system. The excess TMA exited out the sides and reacted with atmospheric moisture to form Al_2O_3 dust. Particulates in this R2R ALD system were monitored using an in situ particulate counter (HandiLaz Mini); with a maximum count level of $7x10^7$ particulates/m^3, 50% ±20% at 0.3 µm counting efficiency, and three thresholds of 0.3, 0.5, and 5.0 µm. The XX (web longitude) and YY axes (web width) of the coating head/sled were measured with the particulate counter and shown in Figure 2.3.
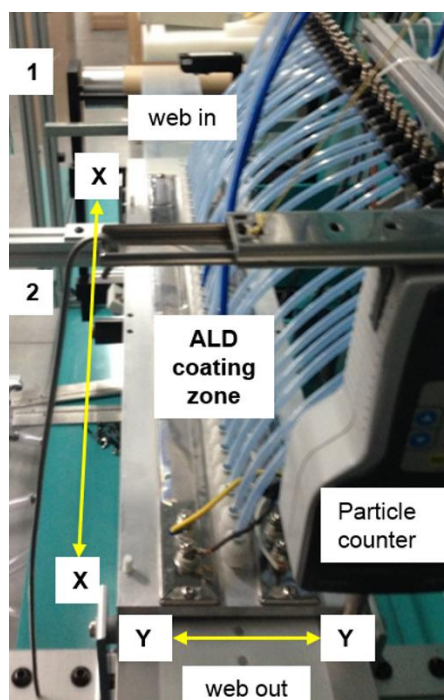
Figure 2.3. In situ particulate counting method is shown. Rollers 1 and 2 are labeled for reference.

CFD modeling was performed to design the ALD coating head and to identify appropriate operating conditions. The gas diffusion properties of the H_2O and TMA precursors were evaluated. Methane was used as an analog for TMA due to its availability in the software. It was assumed

that any mixing of the precursors would react instantaneously, so modeling of the reactions was not necessary. Additional boundary conditions were set as follows: polymer web surface—moving wall at varied speed in web direction; side gaps between web surface and underside of coating head—infinite reservoir boundary condition of 84 kPa (atmospheric pressure in Broomfield, CO); underside of the coating head —fixed wall; temperature—isothermal 120 $^{\circ}$C.

2.2.3 Al$_2$O$_3$ ALD Film Deposition Condition

The gas lines were purged with dried N$_2$ for at least an hour prior to deposition. During this time, the coating head and sled were heated to the desired operating temperature, typically 100 $^{\circ}$C. The coating head rapidly heated the web substrate up to the deposition temperature as it entered the coating head during each revolution. The vertical conductance gap height was typically set to 0.5 mm (but it ranged from 0.25 to 1 mm). The N$_2$ precursor carrier gas flow through the TMA and water bubblers ranged from 0 to 0.25 slpm per dosing nozzle. The reactant gas was then further diluted with additional N$_2$ gas to achieve a flow of 1.5 slpm at 3 atm for each nozzle. The N$_2$ purge gas band between the precursors ranged from one to three adjacent nozzles. ALD cycle times of 76 ms could be achieved with one N$_2$ nozzle between the precursors and a web speed of 1 m/s. This calculation is based on the speed of the substrate and the width, 76 mm, of one ALD cycle, TMA/N$_2$/H$_2$O/N$_2$.

2.2.4 Reflectometry for in Situ Film Thickness Monitoring

This dissertation work demonstrated the use of a reflectometer, as shown in Figure 2.4, for rapid, in situ characterization of an ALD film as it was being deposited on the polymer web that passed repeatedly under the ALD coating head.
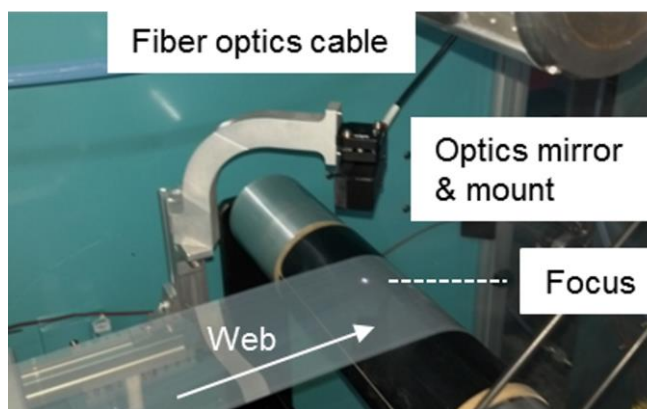
Figure 2.4. Reflectometer measurement setup is shown, with the focused light beam reflecting off of the polymer web just ahead of where it contacts the drive roller.

The reflectometer (FilMetrics F20-UV) is capable of measuring film thicknesses ranging from 2 nm to 40 μm. Light from a broadband source with a wavelength range of 200 to 1100 nm was transmitted via a fiber optic cable bundle and focused onto the substrate at a perpendicular angle. The reflected light was transmitted back to a built in spectrometer, which measured the intensity of the reflected light at 512 different wavelengths. Film thicknesses were then calculated based on the FILMETRICS modeling software.

Prior to a reflectometer measurement, a reference baseline procedure was performed to calibrate the spectral response of the system. In the case of measurements performed on a moving web substrate, this procedure required the acquisition of a baseline on a moving and heated PEN web. The baseline procedure required a reference sample of known reflectance to be acquired, PEN Q51 in this case, and a "dark" background reading to take in account for the current leakage inherent in photodiodes.

Figure 2.4 shows the setup of the in situ reflectometer installed above the web on roller number 4. The light was focused onto the web at a perpendicular angle and ~0.5 cm ahead of where it contacts the drive roller. This location was chosen since it should have the best combination of

low vibrations and planar geometry in this web path configuration. The black matte finish of the drive roller should also help to reduce additional unmodeled backside reflections. The in situ thickness measurements were acquired at a focal distance of ~75 mm from the optical mirror to the web substrate. The growth behavior was typically monitored at 25 mm lateral location with respect to the edge of the web. In addition, postdeposition thickness measurements were obtained using the reflectometer in order to map thickness uniformity profiles of the ALD coating across the web at different locations on the web.

2.2.5 Reflectometry Optical Model and Filtering Methods

The reflectometer operational repeatability and accuracy was verified using a reference Si wafer standard with 724.7 nm of SiO_2. This test produced an average film thickness of 724.0±1.6 nm (0.2%) over the range of the 15 repeated measurements acquired at the same location. The vendor stated error is ±2 nm for films thinner than 500 nm and 0.4% for films thicker than 500 nm.

The optical model used for the reflectometry measurements of Al_2O_3 films was defined by the following layers: Air, 1 nm of surface roughness, amorphous Al_2O_3, PEN Q51, and backside reflections. The refractive index of the Al_2O_3 was initially assumed to be 1.6 but was allowed to vary during the fitting procedure using an amorphous dispersion model. The Filmetrics FILMeasure software used a grid method to search for the best fit spectra match between the observed and predicted reflectance spectrum in order to determine the film thickness. The time-delay between the measurements was limited by the 250 ms acquisition time and the calculation time. Typically, this interval was 1-2 seconds, allowing for the procurement of at least one data point during each 4 s revolution of the web loop (when operating at 1 m/s web speed).

The Filmetrics reflectometer system calculates several parameters useful in determining the validity of the derived thickness measurement. The software provides a weighted based fitting

parameter, goodness of fit (GOF), which reflects how well the measured and observed spectra match. A GOF of 1.0 reflects a perfect spectra match. The data from the in situ tests used to determine growth rates was filtered using the GOF, kalumina, and nalumina parameters. Typically, the parameters were set to GOF > 0.98, kalumina = 0, and $1.3 \leq$ nalumina ≤ 1.7. Figure 2.5 shows all the parameters used in the filtering of all the thickness monitoring results to be discussed in this dissertation work. Non-zero extinction coefficients and deviating refractive indices correspond directly to a poor GOF and are indicated by outlier thickness measurements.
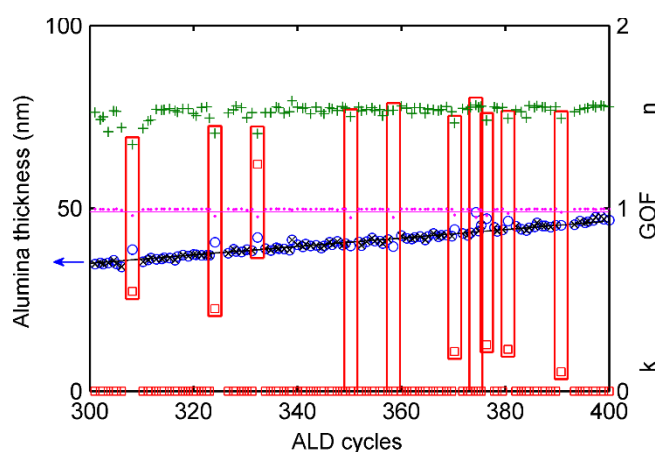
Figure 2.5. The data filtering method is shown for a portion of the reflectometry data of an in situ thickness monitoring of an Al_2O_3 film deposition with optimized reactor system parameters. The red boxes show the filtered out data points which were excluded from the data used for the regression line. Legend: green pluses (n), red squares (k), pink circles (GOF), blue circles (raw data), black crosses (good data), pink line (GOF cutoff = 0.98), and black line (linear regression through filtered data). Please refer to the text for an explanation of the criteria used to filter the data.

In some cases, poor measurements were attributed to reflectance spectra acquired over the web splice. (This gap in the web is an artifact of configuring the polymer web into a continuous loop.) Other poor measurements seemed to be a consequence of surface particulates and/or scratches.

The repeatability/precision and stability of the in situ Al_2O_3 film thickness measurements were determined based on in situ reflectometry data collected on a 47 nm thick Al_2O_3 film after the ALD run was finished. Figure 2.6 shows the rolling 2 σ of the thickness measurements computed using a simple moving 10 data point center window.
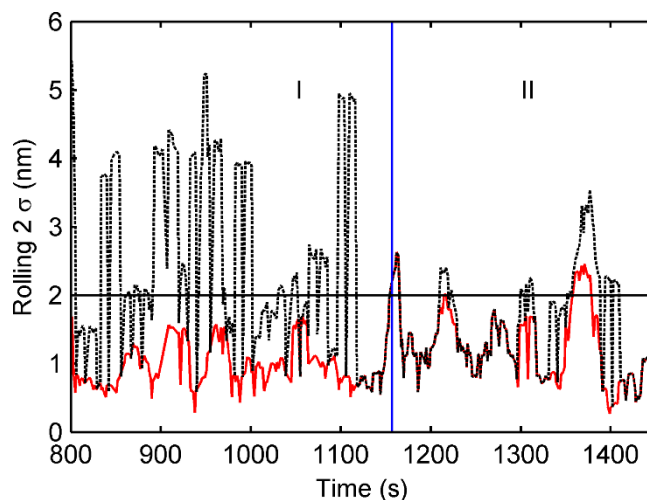
Figure 2.6. The rolling 2 σ deviation of in situ thickness measurements on a 47 nm Al_2O_3 ALD film is plotted to show the repeatability/precision and stability of the reflectometry technique with respect to time and web movement. Region (I) represents measurements on a moving web. Region (II) represents measurements on a stationary web. In situ unfiltered data is shown in faded black curves. Filtered data is shown in bold red curves. The horizontal solid black line represents the standard error of the reflectometer (±2 nm).

Region (I) measurements were collected on a moving web, such that the measurements occurred along the longitudinal direction of the web. The precision of the measurements in this region are affected by the random error of the instrument as well as any ALD uniformity variations. The unfiltered data shows random error, 1.2±1.4 nm (±2.6 nm total), is greater than that of the instrument standard error of ±2 nm. However, the filtered data random error, 0.5±0.4 nm (±0.9 nm), is within the instrument standard error. Region (II) measurements were collected on a

stationary web (all at the same measurement spot). The unfiltered data shows a noticeable decrease in the amplitude of the random error to 0.8±0.7 nm (±1.5 nm total). The percent change in the total average of 2 σ between the unfiltered data in Regions I vs. II is 42%. The filtered data remains largely unchanged in comparison to the unfiltered data and is 0.6±0.5 nm (±1.1 nm total). The percent change in the total average 2 σ between the filtered data in Region I vs. II is 14%. The large percent change of the unfiltered data suggests that the total random measurement error and precision of the unfiltered thickness measurements are a function of a moving web and, to some extent, time. The small percent change in the filtered data suggests a relatively weak function of a moving web and time.

The relatively low random error of the filtered rolling 2 σ of the mean 2 σ in region I (±0.4 nm) vs. Region II (±0.5 nm) suggests that the measurement precision of the filtered data is stable and does not change significantly with time.

2.3 Results and Discussion

2.3.1 ALD Reactor Operation and Film Properties

The initial operating conditions for the atmospheric pressure S-ALD reactor were based on the CFD modeling. Conditions were identified such that the H_2O and TMA (i.e., methane) species did not mix between their respective dosing locations. For example, the CFD modeling predicted that for 1 m/s web speed, adjacent precursor and purge bands (consisting of a one nozzle each), and a 0.8 mm gap height, 4 slpm of gas flow per nozzle would be required to prevent mixing of the precursor bands. Minimum flow solutions were found for various gap heights from 0.1 up to >1 mm. (For gaps far larger than 1 mm, gas flow becomes turbulent and significant precursor mixing occurs.) The validity of the modeling was corroborated by very faint deposition patterns on the underside of the coating head which matched the TMA precursor band shape predicted by the CFD

model. The ALD web coating system was successfully utilized to deposit Al_2O_3 ALD films onto 4 m long polymer web substrates, with Al_2O_3 thicknesses up to 200 nm. The successful operation of the system was indicated by thickness measurements of the Al_2O_3 ALD films which indicated growth rates saturating at ~0.11–0.13 nm/cycle, consistent with growth achieved at low-pressures in conventional ALD reactors.[37] Achieving sufficient water purging during atmospheric pressure ALD can be challenging[61] and tends to result in an increase in the growth per cycle as well as a degradation of film properties. Previous studies have shown that non-optimized residence times, system purge/exhaust flow rates, precursor partial pressures, and/or deposition temperatures can lead to anomalous growth per cycle, variable film refractive indexes, and/or poor barrier properties.[24,42,43,46–48,51–54,74]

Table 2.2 shows a film thickness comparison between in situ reflectometry on a moving and stationary web, ellipsometry, and SEM.

Table 2.2. Al_2O_3 film thickness measurement techniques are compared.

Sample	In situ reflectometry moving web (nm) a)	In situ reflectometry stationary web (nm) a)	Ex situ ellipsometry (nm)	SEM (nm)
I	52	51		~50 - 53
II	105	105	101 ± 7	
III	184		188 ± 3	

a) The standard error of the reflectometer is ±2 nm.

The agreement between the techniques (within experimental error) validated the use of the reflectometer for in situ thickness monitoring. The refractive index of the films deposited at 100 °C was typically 1.5–1.6, similar to other studies.[47] The water vapor transmission rates (WVTR) of 50 nm Al_2O_3 ALD films were measured with values as low as ~0.025 g/m^2/day at 38 °C and

100% relative humidity using MOCON testing and shown in Figure 2.7. This permeation rate was two orders of magnitude lower than that of bare PEN, although it did not achieve the excellent barrier properties that have been reported in earlier studies.[21] It seems likely that the Al_2O_3 dust generated on the side of the coating head during the ALD process contaminated the film and thereby degraded its barrier properties. This problem could be remedied by exhausting and containing the gases from the coating head. In addition, the repeated passes of the web over the rollers may degrade the barrier properties.[75] In contrast, in a R2R system, the web would be subjected to only a few passes over rollers, reducing fatigue stresses. Trace amounts of water in the ppb N_2 purge lines may also react in a CVD fashion with adjacent TMA dosing lines.
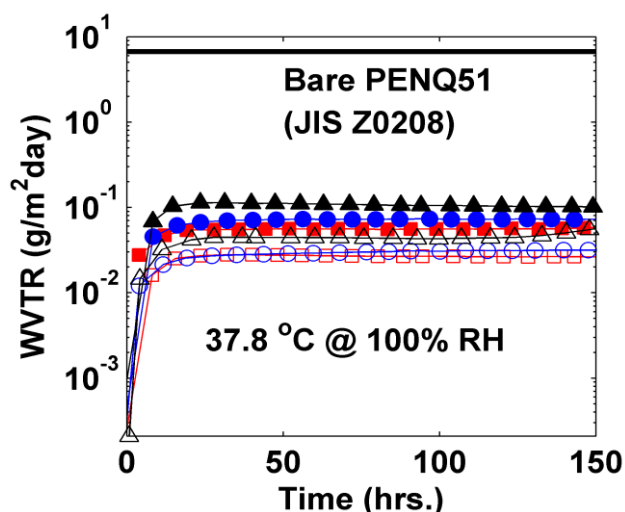
Figure 2.7. WVTR for two different locations on same web substrates (open symbol, closed symbol) for three separate R2R ALD runs (triangle, square, and circle) is shown.

Wide ranges of operating conditions were explored using this S-ALD web coating system. In some cases, mixing of precursors under the coating head was observed, resulting in higher growth rates and dust formation on the surface of the polymer substrate. The excessive growth per cycle could be attributed to insufficient purging caused by factors such as large gas conductance gap heights, low purge flow rate, and/or low temperatures. This observation is consistent with previous

studies which have shown that increases in low temperature (<130 $^\circ$C) atmospheric ALD growth rates can be explained by excess physisorbed H_2O molecules and can be remedied with sufficient purge velocities.[61] Also, S-ALD studies using helium as a tracer gas have shown that with sufficient purge gas velocities gas entrainment will not contribute to precursor mixing.[54]

The contribution of CVD reactions towards the total film growth, trace amount of water in the ppb N_2 with TMA, was investigated by placing a stationary 15.24 cm (6 inch) Si wafer directly underneath a TMA zone between two N_2 purge zones. In theory, during normal operational conditions, the Si wafer, when removed into ambient air, will have experienced one full ALD cycle, but this was not observed. During this one ALD cycle, methylation of the surface sites on the Si wafer will occur in the presence of TMA. Moisture in ambient air will then hydroxylate the surface during the second ALD half reaction. Instead, two well defined deposition bands were formed at the regions between the TMA and N_2 nozzles as shown in Figure 2.8. The deposition bands were measured over a ~1.5 mm spot with a film thickness of ~221 nm with 30 minutes of operational gas flow. As a result, CVD reactions contribute ~0.3% towards the total growth per cycle.
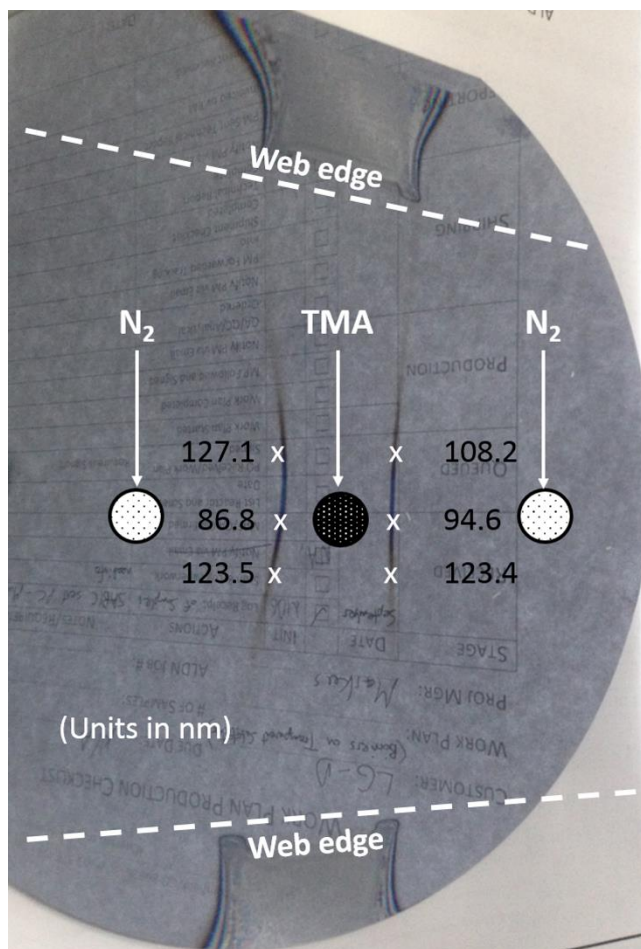
Figure 2.8. Silicon wafer after exposure to ~30 minutes of normal operational gas flows of N_2 and TMA with a web speed of 0 m/s.

2.3.2 ALD Reactor Particulate Levels

CVD reactions may also occur when unreacted TMA is vented into the enclosure and mixes with moisture in the air. The particulates generated may then deposit on the web substrate during the endless web process, and as a result the particulates may compromise the barrier quality of the film. Particulates were monitored using a particle counter at the web edge of a TMA nozzle and is shown in Figure 2.9. The particulate levels during the ALD process were reported with the before values subtracted out to allow comparison between multiple ALD runs. CVD particulates generated in this R2R ALD system were ~968 times higher than the dust contaminate levels in the

enclosure before the ALD process. The level of cleanliness for this R2R ALD system and a conventional ALD reactor before the ALD process were on the same order.
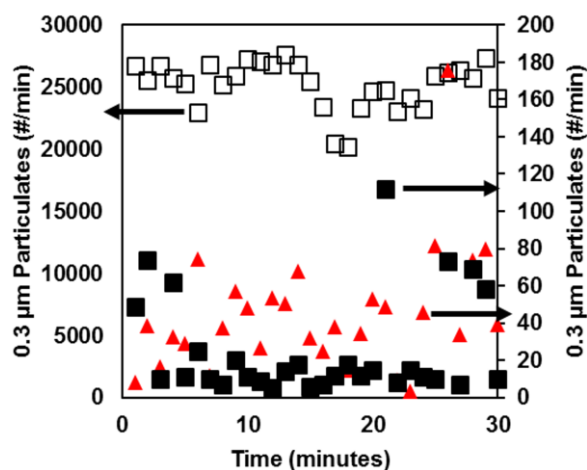
Figure 2.9. Particulates before (closed square) and during (open square) the ALD process measured at the edge of the web near the first TMA nozzle for the configuration shown in Figure 2.2 is shown. Particulate levels before the ALD process in the ALD Nanosolutions reactor (conventional reactor) are depicted with closed triangles. Each data point is an average of particulates measured during one minute intervals.

To investigate the sources of the particulates, 8 cm increments along the web longitude of the coating head/sled from the web entrance to the exit were measured as shown in Figure 2.10. The 30 nozzles of the R2R ALD system for these measurements were configured in the following way: $N_2(x10)/TMA/N_2(x3)/H_2O/N_2(x3)/TMA/N_2(x3)/H_2O/N_2(x7)$. Each nozzle center to center distance was about ~1.9 cm. The two TMA inlet lines, with the location of the fourth N_2 nozzle set to 0 cm, are ~13.3 cm and 28.6 cm, respectively. The first in situ measurement location corresponds roughly to the location of the fourth nozzle which is a N_2 nozzle. Three separate ALD depositions were measured and averaged. Measurements were acquired from three passes up and back along the web longitudes with an acquisition period of 20 seconds at each location along the

longitude of the web. The particulate levels were observed with two peaks near the TMA nozzles for all particulate sizes, which suggests that unreacted TMA and moisture in the enclosure were in fact the CVD particulate sources.
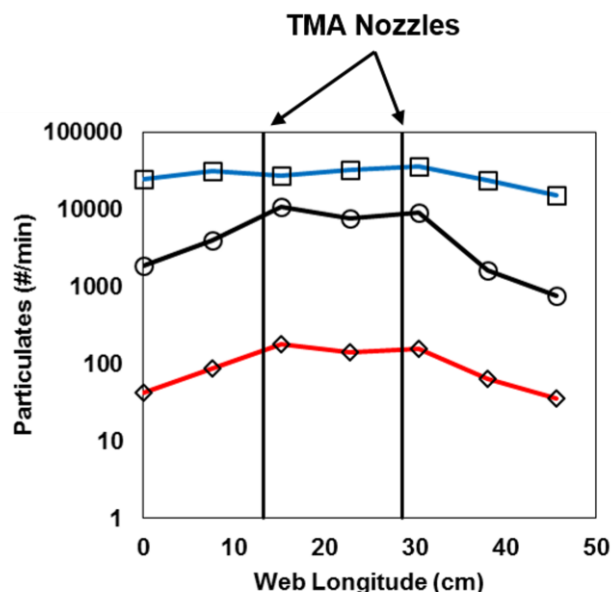
Figure 2.10. Mean particulates of size 0.3 µm (square), 0.5 µm (circle) and 5 µm (diamond) during three separate ALD processes measured across the longitude of the web during the ALD process is shown.

The particulates along the web width are shown in Figure 2.11. The level of particulates increases towards the web edge. This increase in particulates in either case follows that the N_2 purge gases are pushing particulates towards the edge of the web. The pseudo-asymmetrical particulate profile was a result of an unintentional tilted coating head/sled. Large 5 µm size particulates were not observed in the gas flow. Using a particulate counter, the number of particulates on the web surface could not be measured.
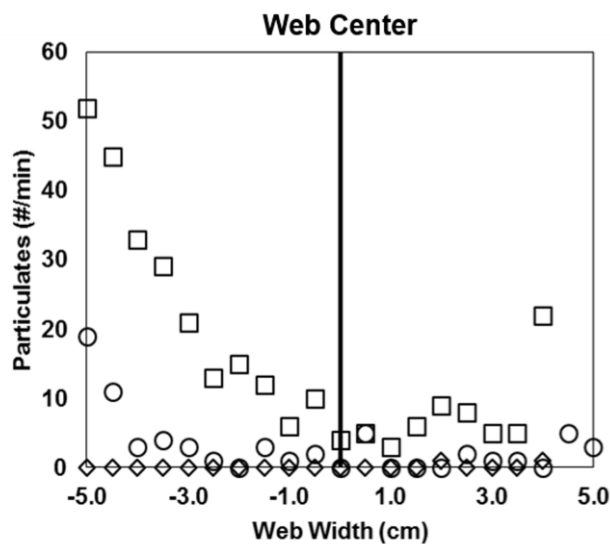
Figure 2.11. Mean particulates of size 0.3 µm (square), 0.5 µm (circle) and 5 µm (diamond) during three separate ALD processes measured across the width of the web during the ALD process is shown.

Particulates generated during the ALD process in this R2R ALD system were determined to be sourced from TMA and trace ppb moisture in the N_2 lines reacting in a CVD fashion, and unreacted TMA mixing with moisture in the enclosure. Particulate generation may compromise the quality of the ALD films in terms of moisture barrier properties. Exhausting of the particulates was briefly explored, but did not result in any barrier improvements. A polymer-based encapsulation method using molecular layer deposition (MLD) polyamide followed by an ALD Al_2O_3 step will be discussed in **Chapter 4** for future ultrabarriers.

2.3.3 ALD Process and in Situ Optical Model Challenges

The optimization of the reflectometer for in situ film thickness monitoring on a moving web required multiple refinements of the optics model and the experimental setup. Figure 2.12 shows the reflectometer data during the first test of the in situ monitoring technique. This data shows significant scatter and a lower than expected growth rate. The solid black line represents the target

growth per cycle of 0.12 nm/cycle. The growth per cycle calculated using a regression of the filtered data (solid blue) was 0.04 nm/cycle. The lower than expected growth per cycle was attributed to be due to insufficient precursor dosing. The scatter in the data was determined to be a result of insufficient web tension, scratching of the web, and use of generic PEN optical parameters.
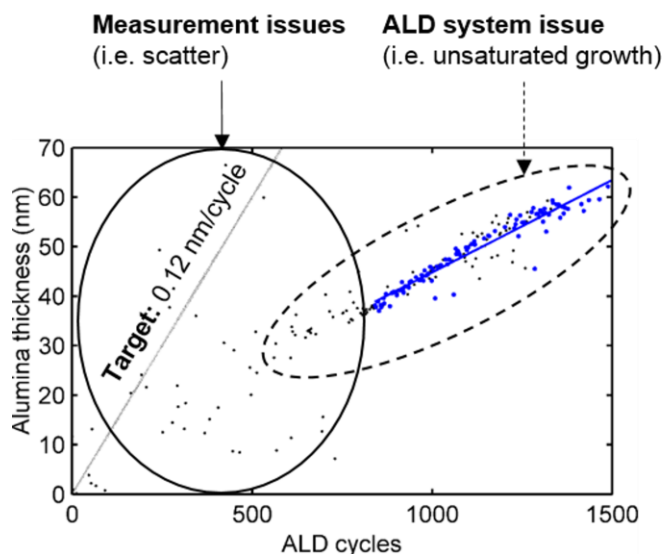
Figure 2.12. In situ reflectometry data showing the thickness of an Al_2O_3 film as a function of ALD cycle number. The growth per cycle was 0.04 nm/cycle based on the linear regression of the filtered data. The target growth of 0.12 nm/cycle is shown as a thin black line for reference.

The improvements obtained by replacing the generic PEN parameters by PEN Q51 parameters, increasing the web tension to ~10 N, and using the correct flow rate of the precursors are shown in Figure 2.13. Increasing the precursor concentration raised the growth per cycle to 0.11 nm/cycle. Reductions in the scatter of the data were also made by eliminating scratching on the web.

2.3.4 ALD Reactor Optimization Using in situ Thickness Monitoring

In situ thickness monitoring of the growth of an Al_2O_3 film on a moving PEN web grown using optimized ALD reactor parameters is shown in Figure 2.13. Film thickness is plotted as a function

of ALD cycle number. A linear growth of 0.11 nm/cycle was observed after an initial nucleation region. The coating head was configured for two ALD cycles per web revolution, with a web speed of 1 m/s. An ALD cycle was defined by one nozzle each of TMA, N_2, H_2O, and N_2.
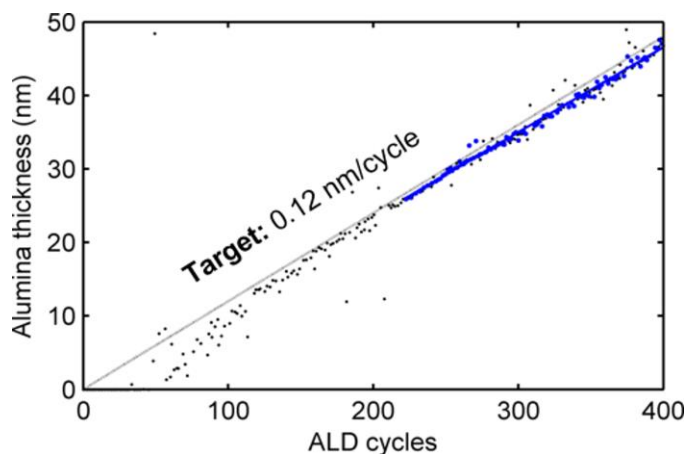
Figure 2.13. Graph of the in situ reflectometry data is shown, with the thickness of an Al_2O_3 film plotted as a function of ALD cycle number. The Al_2O_3 grew at 0.11 nm/cycle ($R^2 = 0.99$) based on the filtered data points are represented by the bold markers (GOF $\geq$ 0.99). The thin line represents the target ALD growth rate of 0.12 nm/cycle.

The ALD cycle numbers were calculated based on the web revolution frequency and the number of ALD cycles per web revolution. Precursors were delivered by flowing 0.15 slpm N_2 through the TMA and water bubblers.

Figure 2.13 shows all of the raw data points, including a subset of filtered data points represented by larger bold markers. These markers represent the data used to calculate a growth rate of 0.11 nm/cycle, as shown by the linear regression with an R^2 value of 0.99. For reference, the thin line represents a typical Al_2O_3 ALD growth of 0.12 nm/cycle. The data not used for the regression were filtered out for a variety of reasons, such as low goodness of fit (GOF), and n or k values that deviated significantly from the expected values.

The data in Figure 2.13 also shows what appeared to be an ALD nucleation period of ~48 ALD cycles. The initiation of ALD growth coincided with a maximum in the GOF parameter which was calculated by the reflectometry software. The subsequent observed decrease in GOF could be attributed to intermixing at the interface of the polymer and Al_2O_3. As a result, the sample reflectance was weaker than expected by the model and was indicated by a decrease in GOF. As the ALD layer became well-defined, the GOF increased again. Nucleation behavior in ALD processes can vary greatly depending on the polymer substrate used as was previously reported in a quartz crystal microbalance study of Al_2O_3 ALD nucleation on various polymers.[41] The nucleation period may also vary when using different dosing conditions.

The ability to perform in situ monitoring of ALD processes allows the exploration of process parameters during an ALD run. Figure 2.14 shows the effects of precursor dosing variations on the growth rate of an Al_2O_3 ALD film.
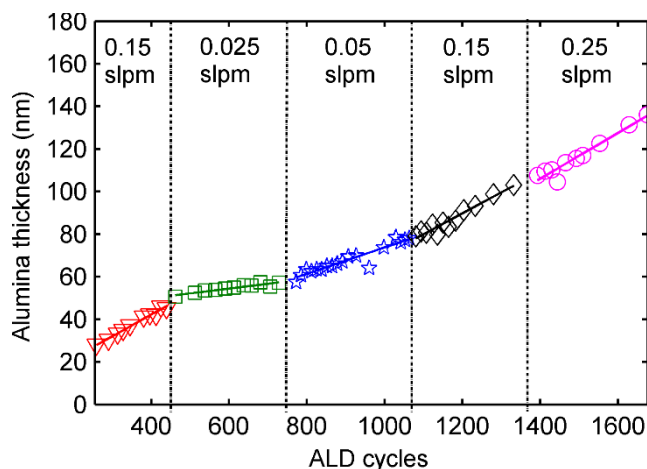
Figure 2.14. In situ reflectometry data show the effects of the N_2 flow rate through the TMA bubbler on the growth of Al_2O_3 on PEN. The calculated growth per cycle of the filtered data was 0.10, 0.02, 0.06, 0.10, and 0.11 nm/cycle from left to right. The R^2 values were 0.98, 0.88, 0.89, 0.94, and 0.94, respectively. Measurements were acquired at a lateral location ~25 mm from the edge of the web

The thickness measurements were obtained at a 25 mm location with respect to the edge of the web. The TMA bubbler flow rates ranged from 0.025 to 0.25 slpm per nozzle, while the H_2O bubbler flow rate and web speed were fixed at 0.15 slpm and 1 m/s, respectively. The coating head was configured to two ALD cycles per web revolution. The coating head was arranged with three N_2 gas nozzles between each precursor nozzle (TMA, N_2, N_2, N_2, H_2O, N_2, N_2, N_2, and repeat).

These data were then analyzed and plotted in Figure 2.15 with the growth per cycle as a function of TMA bubbler flow rate.
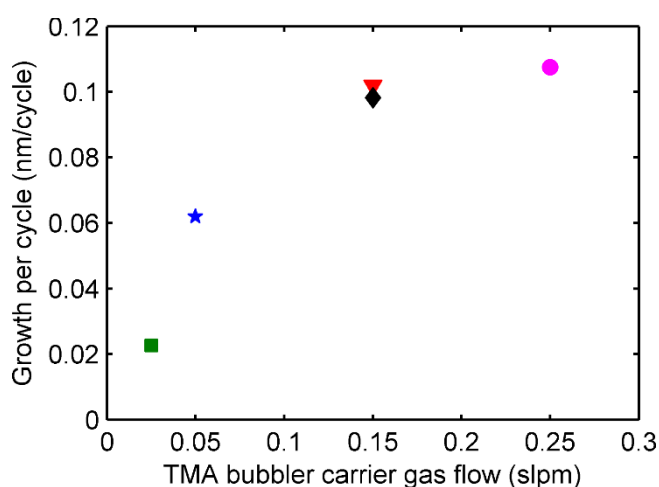
Figure 2.15. This TMA uptake curve plots the growth per cycle as a function of bubbler flow rate, calculated based on the data presented in Figure 2.14. The Al_2O_3 ALD growth appears to saturate at 0.11–0.12 nm/cycle with respect to the TMA exposure. Measurements are acquired at a lateral location of ~25 mm from the edge of the web.

The growth per cycle at each flow rate was calculated based on a linear regression of the filtered data. This TMA uptake curve shows the expected ALD saturation behavior typical of a self-limiting surface reaction. The growth per cycle asymptotically approached a growth per cycle of 0.11–0.12 nm/cycle at high TMA flow rates. When precursor exposures are insufficient, the growth per cycle drops off toward the edge of the web as the precursor stream becomes depleted. A similar

change in the growth per cycle near the edge of the web (achieved by varying residence times) has been observed by Maydannik et al.[53] These results demonstrated the ability of the reflectometer to identify system parameter adjustments and the corresponding thickness trend.

A similar uptake curve experiment was performed as shown in Figure 2.16 and with a web speed fixed at 1 m/s. The minimum growth rate per cycle was ~0.07 nm/cycle. The duration of each exposure was ~10 minutes, or ~300 ALD cycles. Measurements were acquired at a lateral location of ~25 mm from the edge of the web. As expected, Al_2O_3 growth rates decreased as the carrier gas flow through the bubbler decreased.
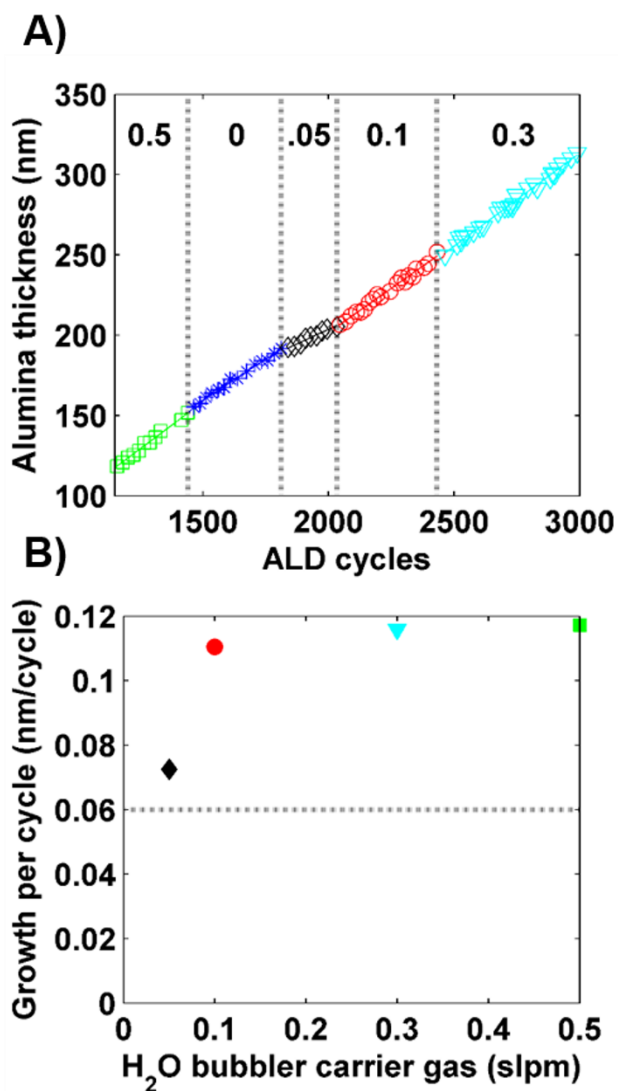
Figure 2.16. (a) In situ reflectometry data show the effects of the N_2 flow rate (slpm) through the H_2O bubbler on the growth of Al_2O_3 on PEN. Flow rate is in slpm units. (b) H_2O uptake curve is shown with growth per cycle as a function of bubbler flow rate. (b) The Al_2O_3 ALD growth appears to saturate at 0.11–0.12 nm/cycle with respect to the H_2O exposure. The R^2 values for flow rates of 0, 0.5, 0.1, 0.3, and 0.5 were 0.99, 0.97, 0.99, 0.99, and 0.98, respectively. The water exposure with 0 slpm carrier gas was not plotted.

However, the minimum growth per cycle measured was only ~0.07 nm/cycle when the coating head was configured for two ALD cycles. Without water dosing, the web surface will be saturated with methyl groups from the TMA exposure upon exiting the coating head. These methyl groups will react with atmospheric water, resulting in one ALD cycle of growth per revolution. In this atmospheric endless web coating system with n ALD cycles per web revolution, the minimum growth rate that can be obtained at ambient conditions is 1/n of the full growth rate. The growth rate per cycle, as a result of the water exposure, was affected by the previous water exposure times. For example, 0 slpm of H_2O preceded by a large exposure of 0.5 slpm of H_2O resulted in a growth rate of ~0.1 nm/cycle and higher than the expected growth rate of 0.07 nm/cycle. However, 0.05 slpm of H_2O dosed after the 0 slpm H_2O step showed an expected growth rate of ~0.07 nm/cycle. This delayed onset for the expected growth rate of ~0.07 nm/cycle follows that the water dosing lines contained water molecules after significant dosing of H_2O at 0.5 slpm prior to the 0 and 0.05 slpm H_2O step. The water molecules are dosed to the web substrate until the lines are fully purged by the N_2 carrier gas flow.

The web speed was varied from 0.5 to 2 m/s during a single ALD coating run with the other parameters held constant and shown in Figure 2.17. The N_2 purge band width was set to 57 mm (three adjacent nozzles). A web speed of 1 m/s yielded the expected growth of ~0.12 nm/cycle.

The growth per cycle was ~0.12 nm/cycle when the web speed was lowered to 0.5 m/s. In another case, a growth of ~0.14 nm/cycle was measured when the web speed was lowered to 0.5 m/s. A slight increase in growth per cycle upon doubling of the TMA and water exposures may be attributed to insufficient water purging and/or the soft saturation behavior of the TMA half reaction.[76] Increasing the web speed to 2 m/s led to a decrease in the growth to ~0.08 nm/cycle. This observation follows that, for subsaturated exposures and with sufficient purging, the growth per cycle will decrease because the precursor residence time is inversely proportional to the web speed. Other studies have shown a similar decrease in growth rate in S-ALD web coating systems with an increase in substrate speed.[25] However, if the purging is inadequate, the growth rate tends to increase due to CVD reactions.[24]
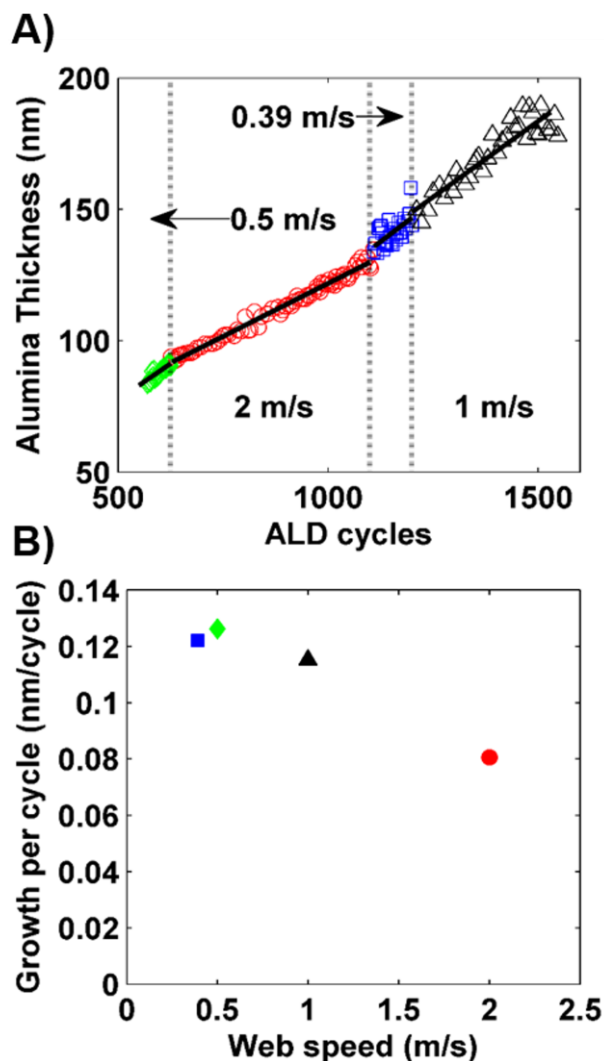
Figure 2.17. Growth per cycle as a function of web speed is shown. (a) Thickness measurements used to calculate growth per cycle with R^2 values for web speeds of 0.39, 0.5, 1, and 2 m/s of 0.41, 0.85, and 0.85, and 0.98 respectively. (b) Growth per cycle calculated from linear fits from (a) with values of 0.12, 0.13, 0.12, and 0.08 nm/cycle for web speeds of 0.39, 0.5, 1, and 2 m/s, respectively.

2.3.5 ALD Film Thickness Uniformity (Ex situ Measurements)

Postdeposition film thickness measurements were performed with the reflectometer to characterize the uniformity of the ALD film. Figure 2.18 shows the growth per cycle as a function

of lateral web location for three different Al_2O_3 films. These tests examined the effects of TMA dosing by comparing carrier gas bubbler flow rates of 0.15 slpm (circles and squares) and 0.1 slpm (stars) on the lateral profile. These experiments also showed the effects of the gas curtain band width of 19 mm (one nozzle: stars and squares) and a band of 57 mm (three nozzles: circles) on the lateral growth per cycle profile. The growth per cycle was calculated based on the total number of ALD cycles, accounting for the nucleation period. The lateral growth profile shown by the circles exhibited a thickness variation of only ±2%, using a bubbler flow rate of 0.15 slpm and purge gas band width of 57 mm. A slightly increased growth per cycle was observed near the edges of the web (shown by the square data points) when the purge gas band width decreased to 19 mm. The thickness variation increased to ±4%. This effect was likely caused by precursor mixing through the N_2 gas curtain near the edges of the coating head and could be remedied by higher purge gas flow rates or wider purge bands. The significant decrease in growth per cycle toward the edge of the web of the star data set arguably corresponds to insufficient precursor surface saturation.
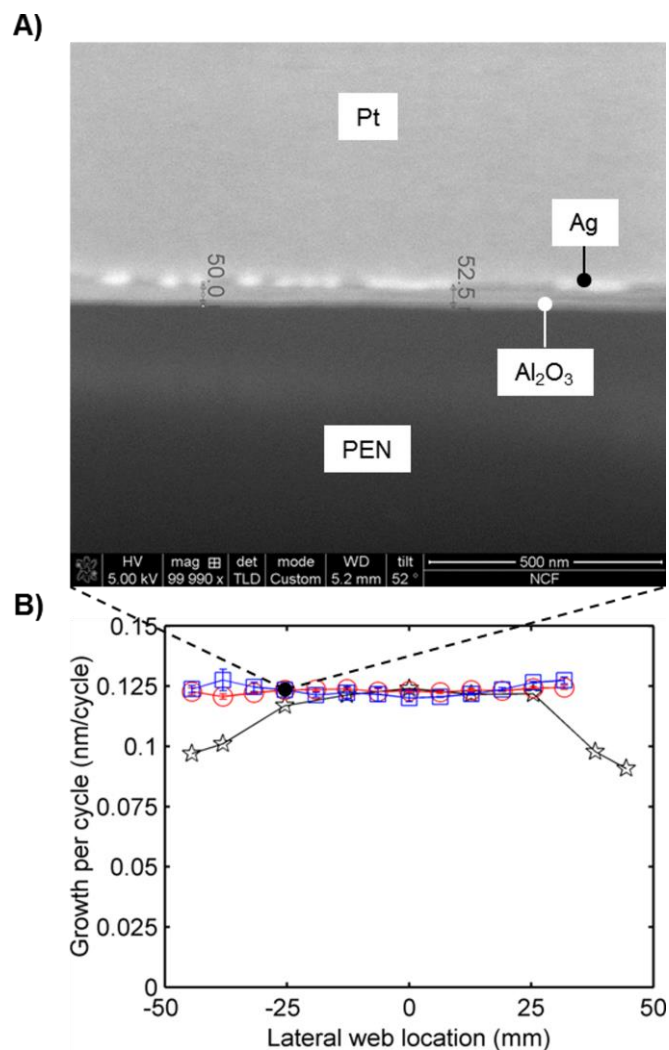
Figure 2.18. (a) This SEM image shows an Al_2O_3 film thickness of roughly 50–52.5 nm, measured at a lateral web location of ~25mm. (b) The lateral film thickness uniformity was characterized using the reflectometer. The growth per cycle is shown as a function of the lateral location across the web for three Al_2O_3 ALD films. The bubbler flow rate and N_2 gas curtain band width was 0.15 slpm and 19 mm for the squares, 0.15 slpm and 57 mm for the circles, and 0.10 slpm and 19 mm for the stars, respectively. The reflectometry measurement corresponding to the SEM image is the square data point at the ~25 mm lateral location, with a film thickness of 51 nm and a 0.12 nm/cycle growth.

Figure 2.18 also shows a FIB-SEM image of the Al_2O_3 film at a lateral location of ~25 mm on the sample represented by the squares. The SEM image (with a 52 degree tilt adjustment) indicated a thickness of ~50–52.5 nm. The 52.5 nm was measured based on the apparent height of the Al_2O_3 layer. The sputtered silver layer (deposited to created contrast between the Al_2O_3 and the physical vapor deposition Pt) appears to have been smeared down over the edge of the cross section during milling. Hence, the 50 nm arrow was measured to the center of a silver cluster. The corresponding reflectometry measurement determined a film thickness of 51 nm (equivalent to 0.12 nm/cycle). Figure 2.19 shows a zoomed out FIB-SEM image of the trench milling technique and use of Ag and Pt to form a contrast at the Al_2O_3/PEN Q51 interface for Figure 2.18.
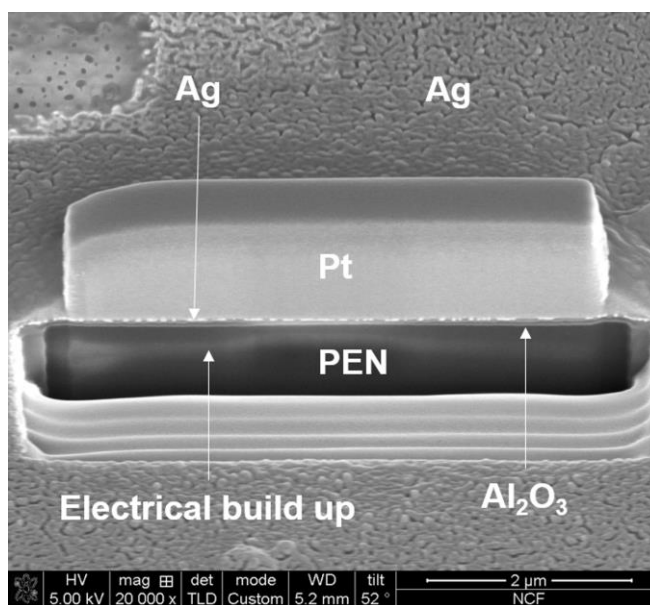
Figure 2.19. This image shows the trench milling technique using FIB-SEM to create Figure 2.18**.**

2.4 Chapter Summary

Al_2O_3 films were grown on a moving polymer web using an atmospheric pressure spatial ALD coating head. Rapid in situ thickness monitoring and process control of this web coating system was successfully demonstrated using a reflectometer. The film thicknesses of multiple samples as determined by the reflectometer showed agreement with ellipsometry and SEM measurements.

The growth per cycle for the Al_2O_3 ALD films was 0.11–0.13 nm/cycle, consistent with typical vacuum ALD growth rates. Precursor uptake curves were acquired in situ by varying the carrier gas bubbler flow rates, showing expected ALD saturation behavior. Web coatings with ±2% lateral thickness uniformity could be obtained with proper operating conditions. As expected, inadequate purging resulted in gas mixing and increased growth near the edges, while insufficient dosing yielded films with decreasing thickness toward the edges of the web.

In situ monitoring on this S-ALD system will enable an improved understanding of the nucleation mechanism of ALD films on different polymer substrates. The pinhole defect density of the film will be explored to better understand the system variables affecting the moisture barrier properties of the films, such as particulates.

High throughput and low-cost roll-to-roll ALD coatings may be realized using atmospheric pressure ALD systems based on the prototype coating head demonstrated in this dissertation work. The in situ reflectometry technique demonstrated here can be used for process control and optimization of S-ALD systems, minimizing the need for postdeposition analysis. For this ALD reactor system to deposit thin film barriers, the pinhole defects and intrinsic quality of the ALD films need to be investigated. **Chapter 3** investigates extrinsic pinhole defects in ALD systems.

Chapter 3 Probabilistic Distributions of Pinhole Defects in Thin Films on Polymeric Substrates

3.1 Introduction

3.1.1 Defects in ALD Films

In this chapter we discuss the following concerning extrinsic pinholes in thin films:

- Extrinsic defects in conventional and spatial ALD films,

- Extrinsic defects in inorganic and organic R2R spatial ALD and MLD multilayer coatings,

- Pinhole simulations for enhanced nanomanufacturing design.

As previously mentioned in **Chapter 1**, ALD technology is essential for applications requiring thin pinhole-free coatings for hermetic sealing[9,11,21,22,58,77], surface passivation[4,69,78–81], high-K thin films[82,83], and other functionalities.[34] Other techniques used in industry and research to deposit single and multilayer barrier films include combinations of chemical vapor deposition (CVD), physical vapor deposition (PVD), and polymer-like deposition processes.[84–87] Conformal thin ALD films have been described as a superior thin film barrier technology.[9] Thin flexible glass is a major competitor to transparent polymer-based devices. ALD films are described as pinhole-free due to the self-limiting and surface saturation behavior of the ALD process,[37] but the nature of the manufacturing processes[57] creates extrinsic pinhole defects and intrinsic[10] defects. For thick ALD films >10 nm, extrinsic defects are a consequence of substrate particulate contamination, and for films <10 nm defects are reported to be due to a less than efficient nucleation process.[38] Typically, in an ALD process, a random and stationary defect density (i.e., defects/area) is used to characterize an ALD coating.[88] However, this representation assumes the distribution of extrinsic pinholes across an entire sample or set of samples is described by complete spatial randomness.

With this representation alone, enhanced manufacturability of ALD-based devices cannot be achieved due to no knowledge of the clustering (i.e., tightly spaced) tendency of the pinhole defects. In terms of a display yield of working pixels, the use of a single density metric is misleading, as shown in Figure 3.1, by a large discrepancy between a simulation of random pinhole defects and a highly clustered pinhole defects simulation of the same defect density and different yields.
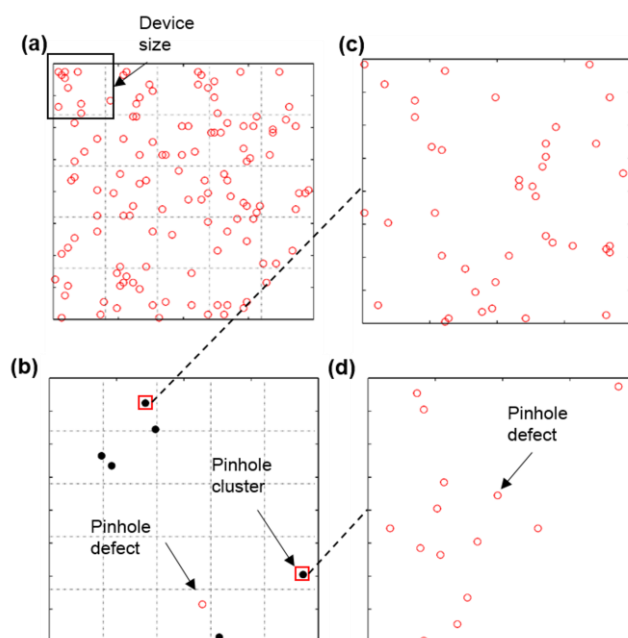
Figure 3.1. Two 5 x 5 illustrative wafers/displays with 25 devices (i.e. pixels on a display) with random or clustered defects. (a) Simulated random defects with density of 126 defects/wafer for a yield of devices without any defects to be 0%. (b) Simulated clustered defects with density of 126 defects/wafer for a yield of devices without any defects to be 76%. The max pinhole cluster size is 41 defects. (c) and (d) Within a cluster area the pinhole defects are random. A single pinhole and a pinhole defect cluster are represented by an open circle and solid circle, respectively.

Single pinhole defects and pinhole clusters (i.e., more than one pinhole defects) are represented by open circles and solid circles, respectively. Pinhole defects are clustered together in tight surface

area regions and entirely absent in other regions of the thin film, and as a result, the density of the pinhole defects is a function of the surface area size and location. The pinholes in each cluster are random in the cluster area, as shown in Figures 3.1(c, d).

A new probabilistic method is needed to characterize defect distributions including clustered pinhole defects. In this study, the probabilistic process by which extrinsic pinhole defects cluster in ALD films was determined, and simulated over a large area such as 1 m^2, which is typical in a manufacturing scale. Simulated devices on the holder, e.g., wafer or glass plate, with patterned ALD coatings, as shown in Figure 3.2, could be investigated by overlaying device patterns onto the extrinsic defect simulation maps to be discussed in detail later.
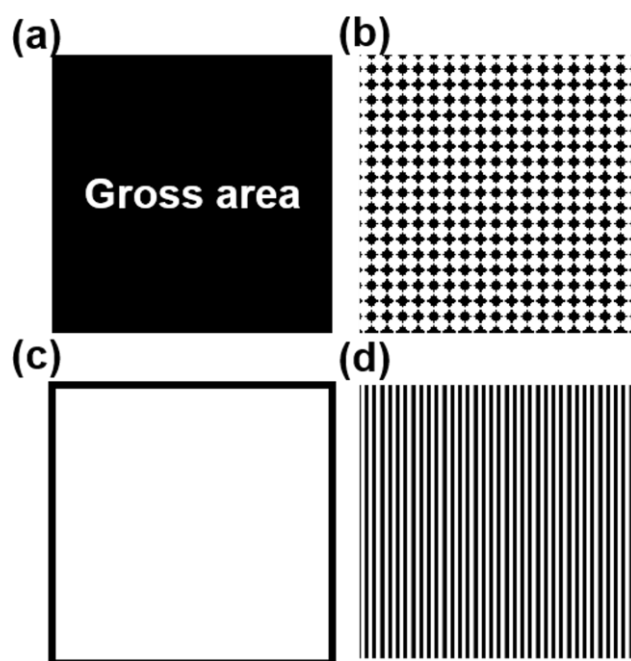
Figure 3.2. ALD-sealed polymer device with different designs: (a) the total area, (b) a designed array of areas, (c) the perimeter, and (d) a designed columns of areas sealed by ALD coatings. The white represents an area that does not require ALD coatings, and black represents an area covered by the ALD coatings. The black regions may represent locations of pixels used to make different lighted patterns.

Areas of the device that require an ALD hermetic seal and areas that do not are represented in black and white, respectively. This design method can be applied to any type of pattern needing ALD coatings, such as displays.

The tendency of defects to cluster was tested by fitting the observed frequency of extrinsic pinhole defect counts per quadrat[89] area mesh size (i.e., unit cell of the grid/mesh used to bin defect frequency counts) to a random and cluster model. Extrinsic pinhole defects in ALD films can deviate from a random process in three ways, as shown in Figure 3.3, and was also discussed in the case of particulate clustering and defects in chips on silicon wafers in the early semiconductor industry.[90–92] Particulate clustering on the coating surface before and during ALD coating is considered to be the driving factor for clustering of extrinsic pinhole defects in ALD films.
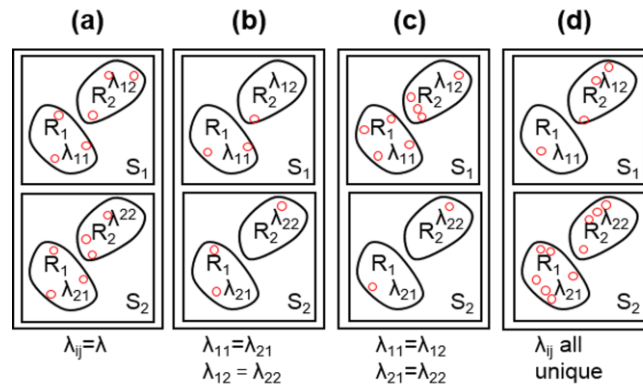
Figure 3.3. Four possible defect distributions with pinhole defects represented by dots in different devices represented by subdomains R_1 and R_2 and different fabrication runs represented by S_1 and S_2: (a) a random process (b) a cluster process resulting from defect clustering, (c) run-to-run fabrication variations with each run a unique random process, and (d) combination of [(b) and (c)].

3.1.2 Probabilistic Random Defect Model

A random pinhole generation model implies that the mean number of pinhole defects (λ_{ij}) within any disjoint subregion R_i in S_j are entirely independent and realized by one parameter $\lambda_{ij} = \lambda$. This

follows that the mean number of defects in any disjoint subregion R_i in S_j is the same. This process

is called a Poisson process

$$P(X = k) = \frac{e^{-\lambda}\lambda^k}{k!},$$ (3.1)

where k is the number of defects and X is a random variable.

3.1.3 Probabilistic Cluster Defect Model

A cluster process shown in Figure 3.3(b-d) cannot be modeled using a one parameter model.

The λ parameter is a random variable in a cluster model with a marginal distribution $P(\lambda)$

$$P(X = k) = \int_0^\infty \frac{e^{-\lambda}\lambda^k}{k!}P(\lambda)d\lambda.$$ (3.2)

The marginal distribution describes the probability of observing a mean number of defects in a

disjoint sub region R_i in S_j.

Equation (3.2) can be solved using a variety of marginal distributions to define the probability

of observing a λ value.[90] For example,

$$P(X = k) = \frac{1}{\Gamma(\alpha)\beta^\alpha} \int_0^\infty \frac{e^{-\lambda}\lambda^k}{k!}\lambda^{\alpha-1}e^{\frac{-\lambda}{\beta}}d\lambda$$ (3.3)

can be formulated by compounding Equation (3.2) with a gamma distribution as the marginal

distribution with parameters α and β.

The final form of Equation (3.3) after integration is the negative binomial model:

$$P(X = k) = \frac{\Gamma(r+k)}{\Gamma(r)\Gamma(k+1)}p^r(1-p)^k,$$ (3.4)

where r and p are model parameters. The relationship of r and p with the gamma distribution

parameters α and β may be written

$$r = \alpha,$$ (3.5)

and

$$p = \frac{1}{\beta + 1} \tag{3.6}$$

The r and p parameters are related to the mean and variance of the distribution by the following:

$$r = \frac{\mu^2}{\sigma^2 - \mu} \tag{3.7}$$

and

$$p = \frac{r}{r + \mu} \tag{3.8}$$

Equation (3.7) can be rearranged to show that the variance can be independently varied by r. The degree of pinhole clustering is described by 1/r; with maximum clustering as r approaches 0. Maximum clustering implies that all pinholes are confined to one infinitely small region. Minimum clustering will occur when r goes to ∞ and the cluster model converges to a random model where the mean and variance are equal.

The statistical method used in this study to test for and simulate clustering of defects was also tested for compatibility using a spatial roll-to-roll ALD system. In spatial ALD systems, the precursor dosing is separated by space rather than time.[36] This compatibility suggests that this ALD-based device design method, to be discussed, may be applicable to other gas-phase thin film deposition techniques such as CVD and PVD. The probabilistic model shows promise as tool to with the capability to identify defect sources using the cluster parameter (1/r).

3.1.4 Barrier Structure Configurations

Hybrid organic and inorganic structures have been investigated as discussed in **Chapter 1**, and were used to reduce extrinsic defects by arresting particulates as shown in Figure 1.10. In this dissertation we compare a single-layer ALD Al_2O_3 by conventional ALD, single-layer ALD Al_2O_3 film by spatial ALD, and a hybrid spatial ALD and MLD structure as shown in Figure 3.4.

ALD films were grown with TMA and water for both conventional and spatial reactors. No special preparation method was used for the spatial ALD and MLD structures.
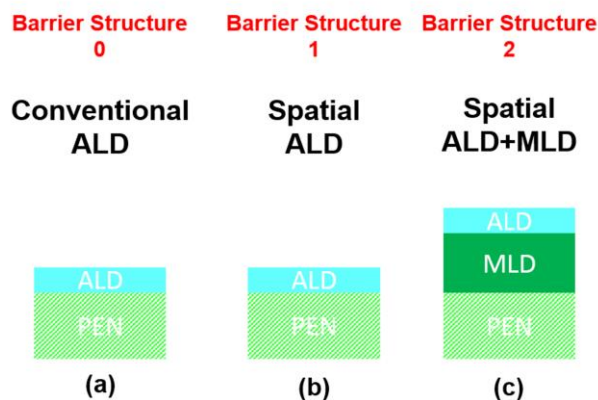
Figure 3.4. Barrier structures investigated in this dissertation. (a) 500 cycles of conventional ALD Al_2O_3. Probabilistic models were fit to this data. (b) 500 cycles of spatial R2R ALD Al_2O_3. (c) 500 cycles of spatial R2R ALD Al_2O_3 on 500-2000 cycles of R2R MLD polyamide. Probabilistic models were not fit to the data for Barrier Structure 1 and 2.

Hybrid organic and inorganic films were deposited using a R2R ALD and MLD reactor in Steve George's group at the University of Colorado at Boulder. The reactor is designed with a fixed outer drum and rotating inner drum to which the substrates are attached. ALD precursors are separated by sequential pumping and N_2 purge zones. The outer drum is a modular design of nozzles which allows different ALD and MLD configurations per rotation. The reactor accommodates a web of ~ 6 inches and has an inner diameter of 12.69 inches. The reactor has been reported to grow good ALD Al_2O_3 films by Sharma and coworkers as shown in Figure 3.5.[56]
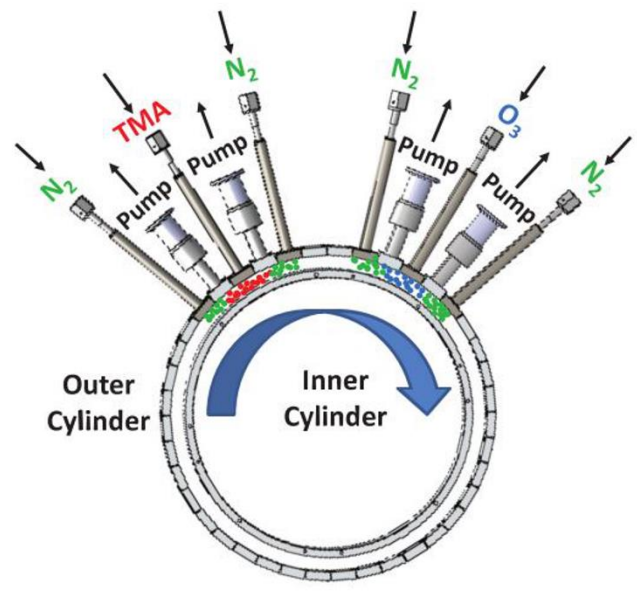
Figure 3.5 Spatial ALD and MLD reactor configured for ALD Al_2O_3.[56]

The ALD and MLD reactor in Figure 3.5 can be configured in a R2R configuration using the web handling system designed and built at Oklahoma State University[93] for the reactor of Sharma and coworker[56] as shown in Figure 3.6.
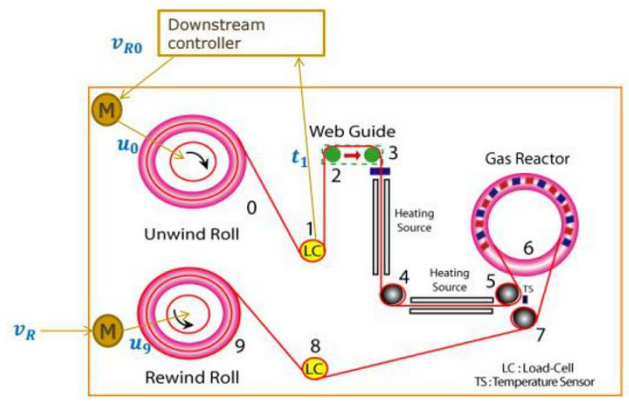
Figure 3.6 R2R ALD and MLD reactor.[93]

3.2 Experiment

3.2.1 Al$_2$O$_3$ ALD and Polyamide MLD Film Deposition Setup and Conditions

For conventional ALD Al$_2$O$_3$ depositions, five samples (1.6 x 1.9 cm) of polyethylene naphthalate (HS-PEN Q51, Dupont-Teijin) were adhered, using double-sided Kapton tape, to a repurposed lithography glass mask to serve as a holder for each of four distinct ALD runs, as shown in Figure 3.7a. For spatial ALD and MLD films 4x4 inch web was subdividing into 16 samples (1.6 x 1.9 cm) as shown in Figure 3.7. Web center indicates the location coincident with the center of the spatial ALD and MLD drum. To avoid confirmation bias, we select sample 03, 06, 12, and 13 for each analysis. No model was fit to the spatial ALD films. More samples would be needed in the future to fit models to the spatial coatings.
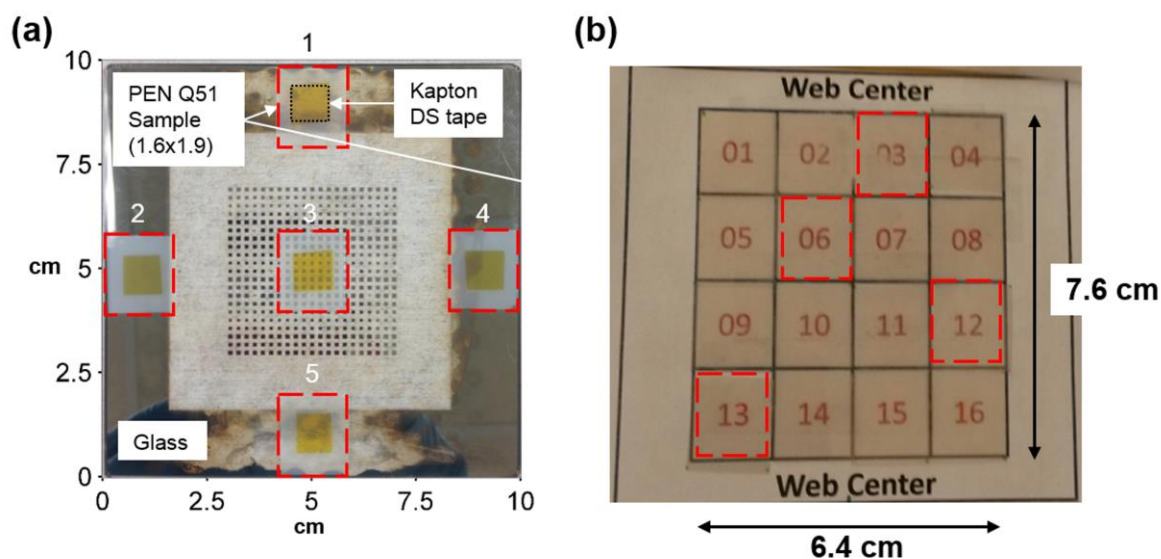
Figure 3.7. (a) Repurposed Glass PEN Q51-substrate holder showing five PEN Q51 samples (1.6 x 1.9 cm) adhered using double-sided Kapton tape and highlighted with dashed boxes. The metal patterns are not relevant to this study and are from a repurposed lithography mask. (b) Subdivided samples for spatial ALD and MLD coatings.

The metal on the repurposed glass holder in Figure 3.7a does not have any purpose in this study. The total surface area of the five samples combined was 60.8 cm^2 of which 30 cm^2 was analyzed. The ALD tool used in this study was a Beneq TFS 200 system. The ALD reactor volume and samples were cleaned prior to each deposition in the Colorado Nanofabrication Laboratory cleanroom facility using ethanol (CHROMOSOLV, HPLC grade). The samples were loaded into the reactor volume in the cleanroom and sealed.

For conventional ALD, trimethylaluminum (TMA) (Strem, 98%) and water (HPLC grade) was used as the Al_2O_3 precursors. The reactor pressure was typically ~2 mbar at the deposition temperature of 110 ^{o}C. Four-hundred and fifty cycles were deposited with cycle times of 1000 ms N_2 purge, 250 ms TMA dose, 1000 ms N_2 purge, and 250 ms water dose.

Spatial ALD Al_2O_3 films were deposited at 110-115 ^{o}C at 100-200 rpm on both PEN Q51 and polyamide MLD substrates. TMA and water were used as the precursors to grow 500 cycles of Al_2O_3. Samples of 4x4 inch wide PENQ51 were attached with Kapton tape at the center of the inner drum of the reactor as the base substrate.

Polyamide MLD films were deposited at 110-115 ^{o}C at 20 rpm on PEN Q51. Trimesoyl chloride and m-Phenylenediamine were used as the precursors to grow ~ 1 μm of MLD. Extrinsic defects were investigated for two structures: 500 cycles of ALD Al_2O_3 on PEN Q51 and 500 cycles of ALD Al_2O_3 on 1 μm thick polyamide MLD on PENQ51.

3.2.3 Defect Decoration and Enlargement Using O_2 Plasma

To visualize defects reported as small as 200 nm[94], the extrinsic pinhole defects in the ALD films for all barrier structures were enlarged and decorated after Al_2O_3 deposition with oxygen plasma etching of the underlying PEN Q51 substrate, and then the resulting undercuts were

visualized with optical microscopy at 100x magnification, as shown in Figure 3.8. The MLD films were also attacked by oxygen plasma.
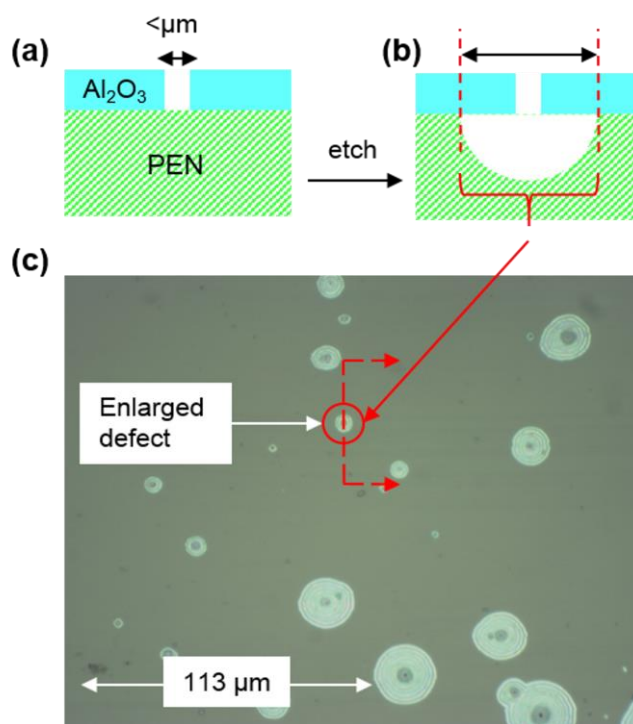
Figure 3.8. Major steps for defect decoration and enlargement technique: (a) Cross sectional cut of an optically flat PEN Q65 sample with a pinhole defect too small to visualize with optical microscope in a conventional ALD Al_2O_3 coating. (b) Enlarged pinhole defect after oxygen plasma etching of the underlying PEN Q65. (c) Optical microscope image showing the undercut pinhole defects.

Image capture resolution used was 1280 x 1024 (i.e., pixel = 0.77 μm^2). The oxygen plasma (Power$_{RF}$ = 75–100 W, pressure = 0.6–0.7 Torr, and time = 6-12 hrs.) was generated using a solid state RF generator (March Plasmod) with a 13.56 MHz signal. Other methods for pinhole defect visualization that could be used are electroplating[88] and fluorescent tagging.[94] Electroplating requires an electrically conductive substrate, which is not suitable for decoration of defects in an ALD film deposited on the insulating PEN Q51 polymeric substrate used in this study. Fluorescent

tagging can be used for defect decoration on polymeric substrates, and provides information on the actual size of the pinhole. Oxygen plasma etching was chosen as the decoration method in this study as it provided the simplest solution for defect decoration.

3.2.4 Image Acquisition Method

For Barrier Structure 0, twenty PEN Q51 samples with 450 ALD Al_2O_3 cycles from four distinct runs were examined for extrinsic defects under a grid as shown in Figure 3.9 using a quadrat method.[90] The same method was used to analyze four samples in each Barrier Structure 1 and 2. But, no model was fit to Barrier Structure 1 and 2.
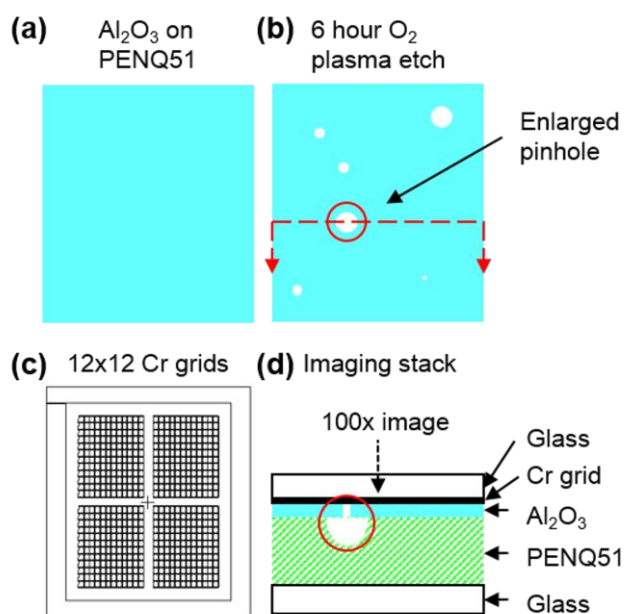
Figure 3.9. Four major steps for defect imaging: (a) Top down view of ALD Al_2O_3 on PEN Q51 with defects too small to visualize with optical microscope. (b) Top down view of enlarged pinhole defects after oxygen plasma etching of the underlying PEN Q51. (c) Glass with four 12 x 12 gridded boxes with each cell corresponding to one 200x microscope image, or 6 x 6 100x images with each image containing four Cr cells. (d) Cr gridded side of the glass is placed on the top

surface of the Al_2O_3 surface with defects. The bottom surface of the sample is held with a blank glass slide.

Each of the four grids consisted of 12 x 12 Cr boxes with a quadrat corresponding to a 200x microscope image. Magnification of 100x consists of four sets of 6 x 6 images, with each image containing four of the Cr cells. The images obtained were of lower quality than Figure 3.8(c) due to the small air gap between the glass slide with the Cr grid and the sample creating a slight distortion of the images. The image files were stored in a directory file, and analyzed using a MATLAB GUI. The GUI functioned by reading each microscope image from file and then prompting the user to manually select the (x, y) pixel location of each pinhole defect. The pixel locations of all of the defects relative to each run were then analyzed for clustering or randomness.

3.3 Results and Discussion

3.3.1 Extrinsic Pinhole Defects in an ALD Structure using Conventional ALD

The (x, y) locations of all defects are plotted in Figure 3.10. Sources and types of these defects will be discussed in **Chapter 3.3.2**. The mean number of defects per run shows run-to-run fabrication variations with densities from 1.62 to 22.92/cm^2. The defect data show that in some cases a pinhole-free film is obtained, such as sample 2 and 7 of runs 1 and 2, respectively. However, 90% of the samples were not pinhole-free and were observed to have at least one defect. In the case of single-sided adhesive Kapton tape used to fasten the PEN Q51 samples to the glass plate, the (x, y) locations of all defects are plotted in Figure 3.11**.** Pinhole defects were mostly observed near or at the perimeter of the samples. Adhesive from the Kapton tape was also observed near the tape edge. A quadrat method[90] was used, with the data from Figure 3.10, to count the number of pinholes in each quadrat (i.e., unit cell of a grid/mesh) and determine the frequency distribution of the number of pinholes per quadrat, and for different quadrat mesh sizes. Pinhole

locations per sample were determined from four sets of 6 x 6 arrangement 100x microscope images with quadrat area mesh size of 2.6 x 10^{-2} cm^2 as shown in Figure 3.9. The defects per smaller quadrat were then counted using MATLAB for quadrat area mesh sizes of 6.4 x 10^{-4} cm^2 (24 x 24), 1.6 x 10^{-4} cm^2 (48 x 48), and 4 x 10^{-5} cm^2 (96 x 96). In the case of the 24 x 24 quadrat mesh, each microscope image was further subdivided into a 4 x 4 mesh or equally a set of 16 smaller quadrats of area size 6.4 x 10^{-4} cm^2. As a result, each of the four original 6 x 6 meshes of 100x microscope images per sample were rearranged into four 24 x 24 meshes. The purpose of analyzing the frequency of defect counts with respect to different quadrat area mesh sizes is to determine the extent of clustering of pinholes in ALD films for simulations or root cause analysis to be discussed later.
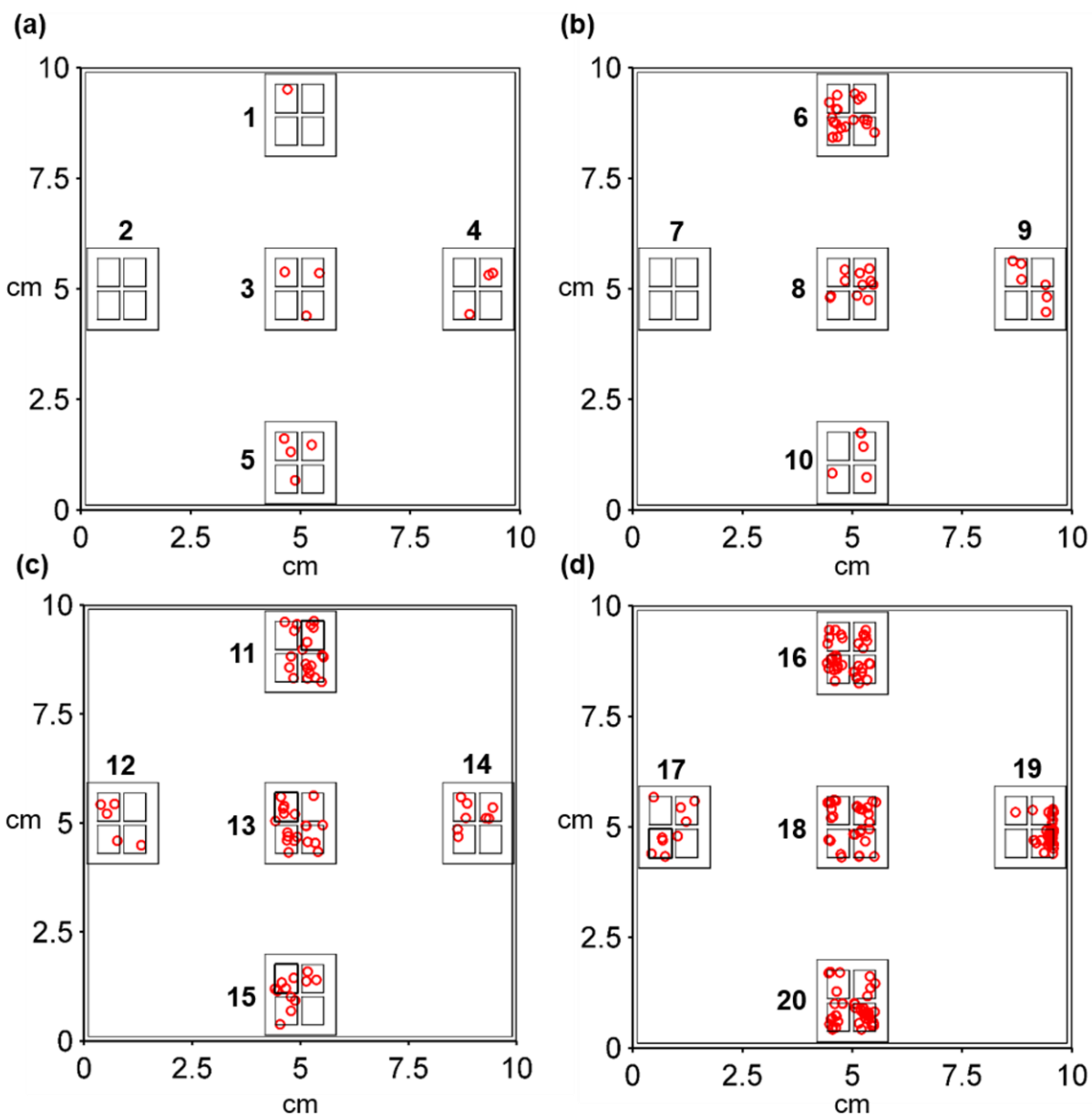
Figure 3.10. Conventional ALD pinhole maps [(a)–(d)] with the centroid of a defect represented by an open circle with arbitrary size. The real size of the defect is not known. The random defect densities of the maps are: (a) $1.62/cm^2$, (b) $6.2/cm^2$, (c) $8.76/cm^2$, and (d) $22.92/cm^2$.
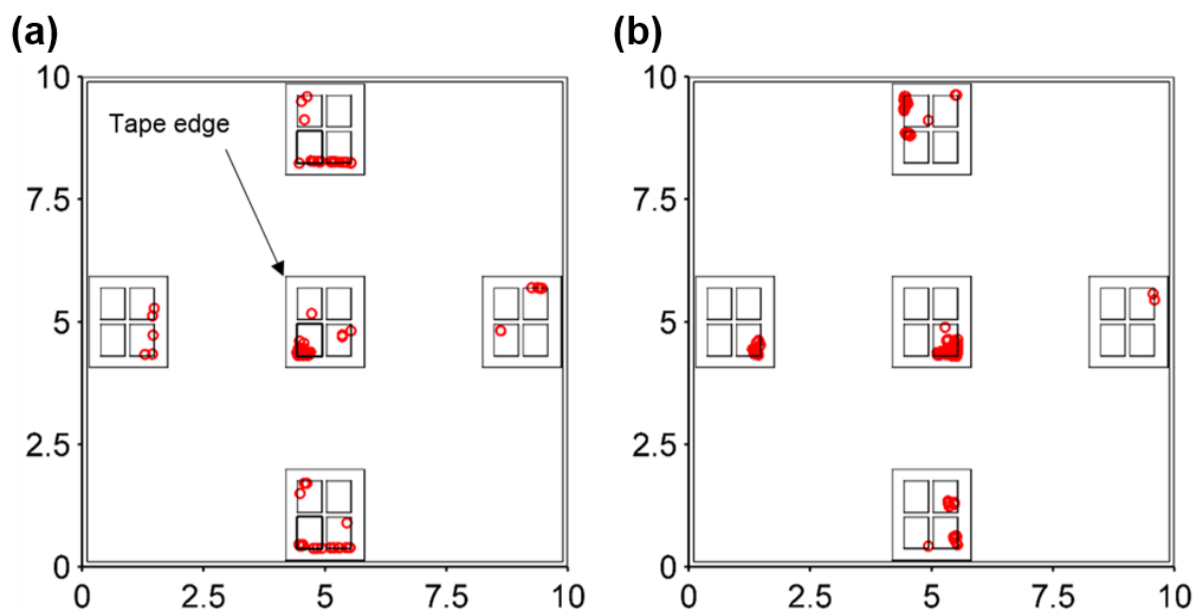
Figure 3.11. Conventional ALD pinhole maps (a, b) with the centroid of a defect represented by an open circle with arbitrary size. The random defect densities of the maps are: (a) 101 defects = 13.70 /cm^2 and (b) 173 defects = 23.46 /cm^2. Single sided adhesive Kapton tape was used to fasten the samples to the glass plate.

To isolate pinhole clustering effects, the cumulative frequency counts for the defects for each quadrat mesh size per run were separately fit using a maximum likelihood estimation (MLE) method in MATLAB to the random and cluster model cumulative distribution functions after integrating in MATLAB Equation (3.1) and Equation (3.2), respectively.[95] The residuals (i.e., the difference between the measured and modeled raw defect counts) of the fits for the random and cluster model are shown in Figure 3.12 and Figure 3.13, respectively.
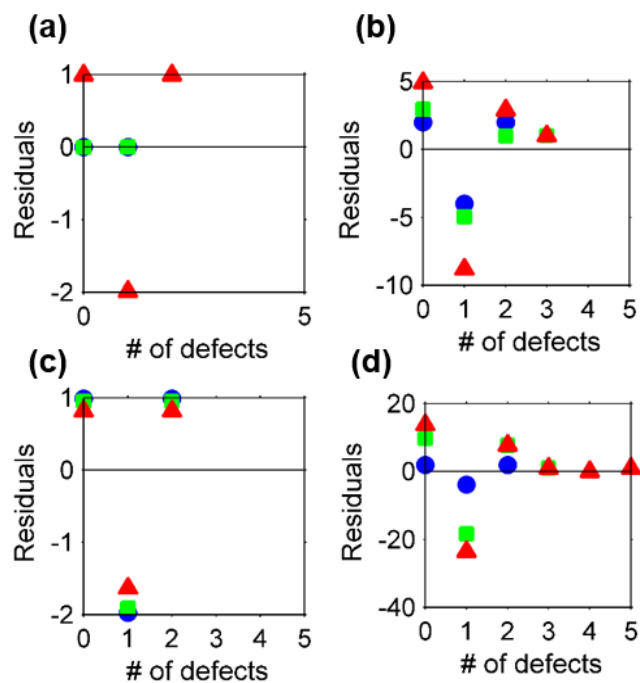
Figure 3.12. Residuals (i.e., the difference between the measured and modeled raw defect count) are shown for ALD coating runs in Figures 3.10(a-d). The quadrat mesh area sizes analyzed were 6.4 x10^{-4} cm^2 (triangle), 1.6 x 10^{-4} cm^2 (square), and 4.0 x 10^{-5} cm^2 (circle). The normality of the residuals for the quadrat area mesh sizes 6.4 x 10^{-4}, 1.6 x 10^{-4}, and 4.0 x 10^{-5} cm^2 for the ALD coating runs are as follows: (a) 0.32, 0.5, and 0.5, (b) 0.07, 0.08, and 0.09, (c) 0.43, 0.34, and 0.32, and (d) 0.06, 0.07, and 0.1, each respectively. A value of 1 indicates that the residuals are random.
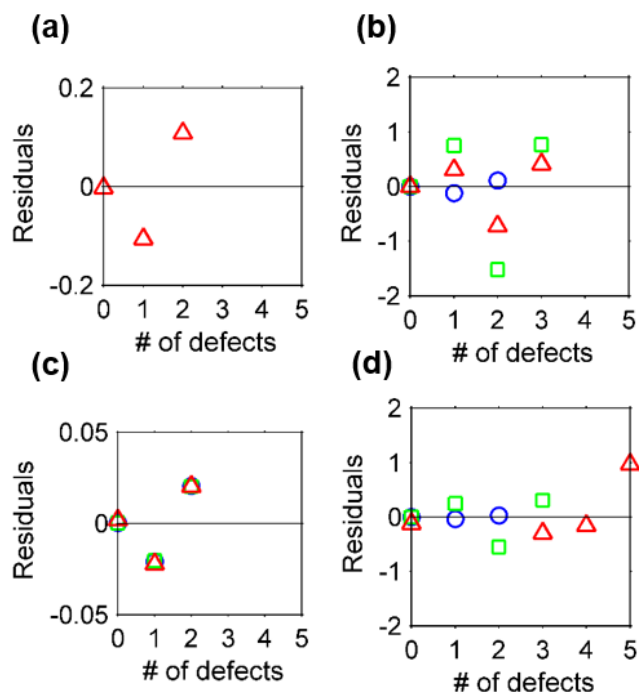
Figure 3.13. Residuals (i.e., the difference between the measured and modeled raw defect count) are shown for ALD coating runs in Figures 3.10(a-d). The quadrat mesh area sizes analyzed were 6.4 x 10^{-4} cm^2 (triangle), 1.6 x 10^{-4} cm^2 (square), and 4.0 x 10^{-5} cm^2 (circle). The normality of the residuals for the quadrat area mesh sizes 6.4 x 10^{-4}, 1.6 x 10^{-4}, and 4.0x 10^{-5} cm^2 for the ALD coating runs are as follows: (a) 0.35, fail, and fail, (b) 0.64, 0.85, and 0.45, (c) 0.35, 0.35, and 0.35, and (d) 0.89, 0.51, and 0.36, each respectively. A value of 1 indicates that the residuals are random.

In all but one case - the defect map in Figure 3.10(a) - the distribution of pinhole defects was best described by a cluster model, with the residuals of the cluster models multiple orders of magnitude less than the random models. The normality of the residuals of both models was calculated with a Kolmogorov–Smirnov test. Seventy-five percentage of the runs were best described using a cluster model, which follows that the deviation from a random model is not singularly due to run-to-run fabrication variation, but also due to pinhole clustering, as shown in Figure 3.3(b).

Run-to-run fabrication variation and clustering of defects, as described in Figure 3.3(d), were tested by combining runs 1–4 into one dataset of frequency counts for the defects for each quadrat mesh area sizes of 6.4 x 10^{-4}, 1.6 x 10^{-4}, and 4 x 10^{-5} cm^2. The residuals of fitting the cumulative pinhole counts to the random and cluster model using the same MLE method are shown in Figure 3.14.
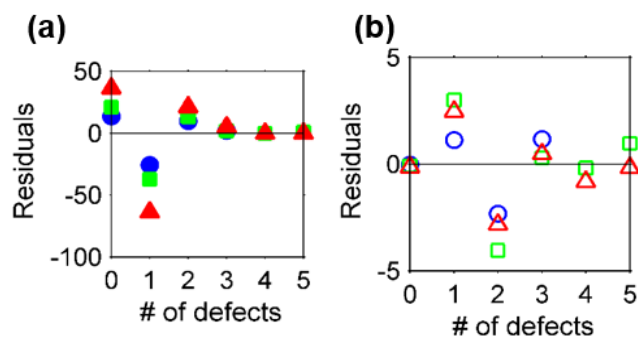
Figure 3.14. Residuals [i.e., the difference between the measured and the random (a) and cluster (b) model defect counts] are shown for ALD coating runs in Figures 3.10(a-d) in one dataset. The quadrat mesh area sizes analyzed were 6.4 x 10^{-4} cm^2 (triangle), 1.6 x 10^{-4} cm^2 (square), and 4.0 x 10^{-5} cm^2 (circle). The normality of the residuals for the quadrat area mesh sizes 6.4 x 10^{-4}, 1.6 x 10^{-4}, and 4.0 x 10^{-5} cm^2 for the random and cluster models are as follows: (a) 0.06, 0.01, and 0.07 and (b) 0.71, 0.52, and 0.45, each respectively. A value of 1 indicates that the residuals are random.

For example, in the case of counting the frequency defect counts of 1 defect per quadrat and quadrat mesh area size of 6.4 x 10^{-4} cm^2, the residuals for the fitting to a cluster model and random model are 3.02 and -37.14, respectively. For this case, the cluster model underpredicts the probability of observing 1 defect or less by 3.02 and the random model overpredicts the probability of observing 1 defect or less by -37.14. A perfect model will have a residual of zero. The residual for predicting a defect count or less was determined up to the maximum observed defect count for that quadrat size. For example, in the case of the largest quadrat size of 6.4 x 10^{-4} cm^2, the

maximum observed number of defects was five. The normality of the residuals for each quadrat area size and defect count describes how well the models describe the pinhole defects. A normal description of the residuals suggests that the error in the model is random and not a systematic error in the model. A larger p-value suggests more evidence that the residuals show normality and that the model is sound. For example, in the case of the quadrat size of 6.4×10^{-4} cm^2, the p-values for the cluster and random model are 0.71 and 0.06, respectively. The relatively smaller residuals and stronger evidence of residual normality with respect to the random model suggests that the cluster model is better than the random model at describing the distribution of pinhole defects. Using the cluster model parameters r and p, pinhole defects on centimeter square devices could be simulated over a large area $\sim 1m^2$. The cluster model parameter estimates for the quadrat area mesh sizes were as follows: 6.4×10^{-4} cm^2 (r = 0.04±0.005, p = 0.861±0.029), 1.6×10^{-4} cm^2 (r = 0.016±0.004, p = 0.909±0.024), and 4×10^{-5} cm^2 (r = 0.012±0.005, p = 0.967±0.015). We showed that the defects per quadrat could be fit to better to a cluster model with respect to a random model.

The datasets A-D in Figure 3.10 were used to train and predict experimental data as shown in Figure 3.15. All zeros were removed from the analysis. For example, in one case maps {B, C, D} were fit to a cluster and random model and then used to predict the probability % of the defects observed in the fourth map A. The cluster model and random model for 2 defects predicted 11% and 1%, respectively. The experimental data (A) was observed to have a 10% probability of observing 2 defects.
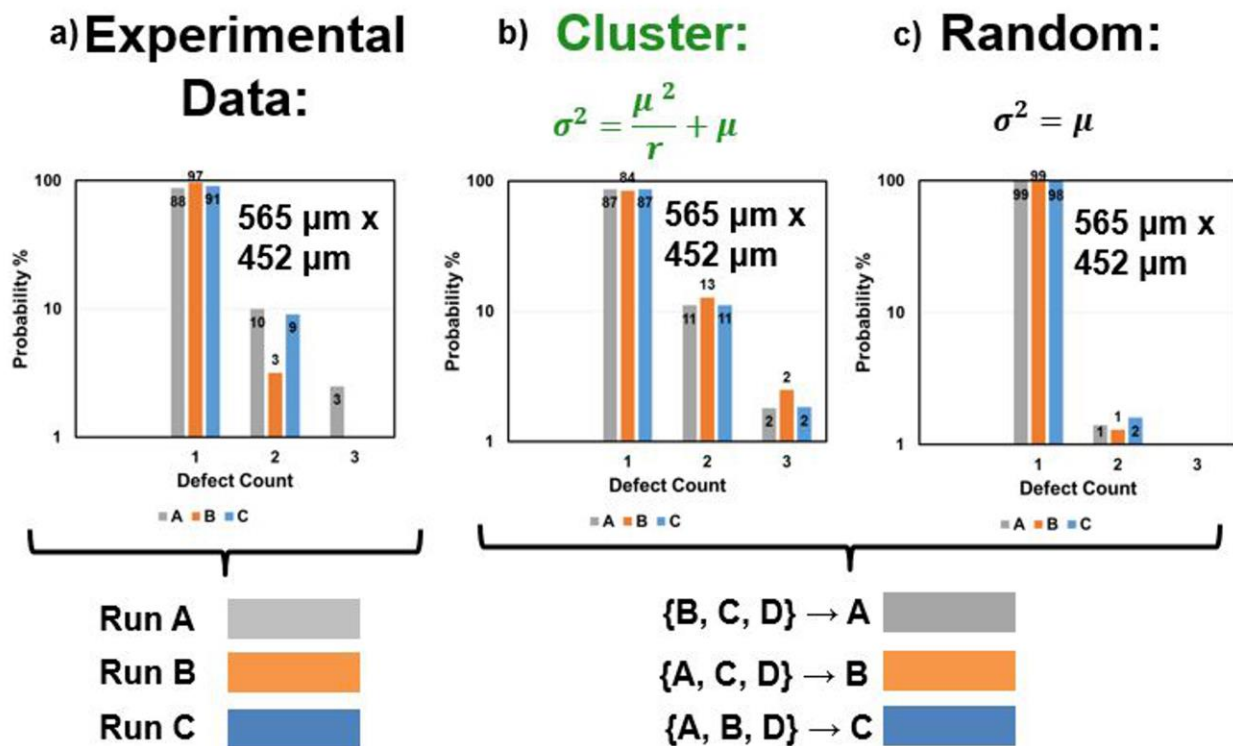
Figure 3.15. Predictive modeling for the quadrat area size of 565 μm x 452 μm. (a) Probability % of observing a defect count. (b) Predicting experimental data A, B, and C from cluster model trained with {B, C, D}, {A, C, D}, and {A, B, D}, respectively. (c) Predicting experimental data A, B, and C from random model trained with {B, C, D}, {A, C, D}, and {A, B, D}, respectively.

3.3.2 Extrinsic Pinhole Defects in a MLD and ALD Structure using Spatial Reactors

The (x, y) locations of all defect partial footprints are plotted for Barrier Structure 1 and 2 in Figure 3.16. The multilayer structure with MLD reduced the number of partial footprints by 10x to values achieved by conventional ALD systems.
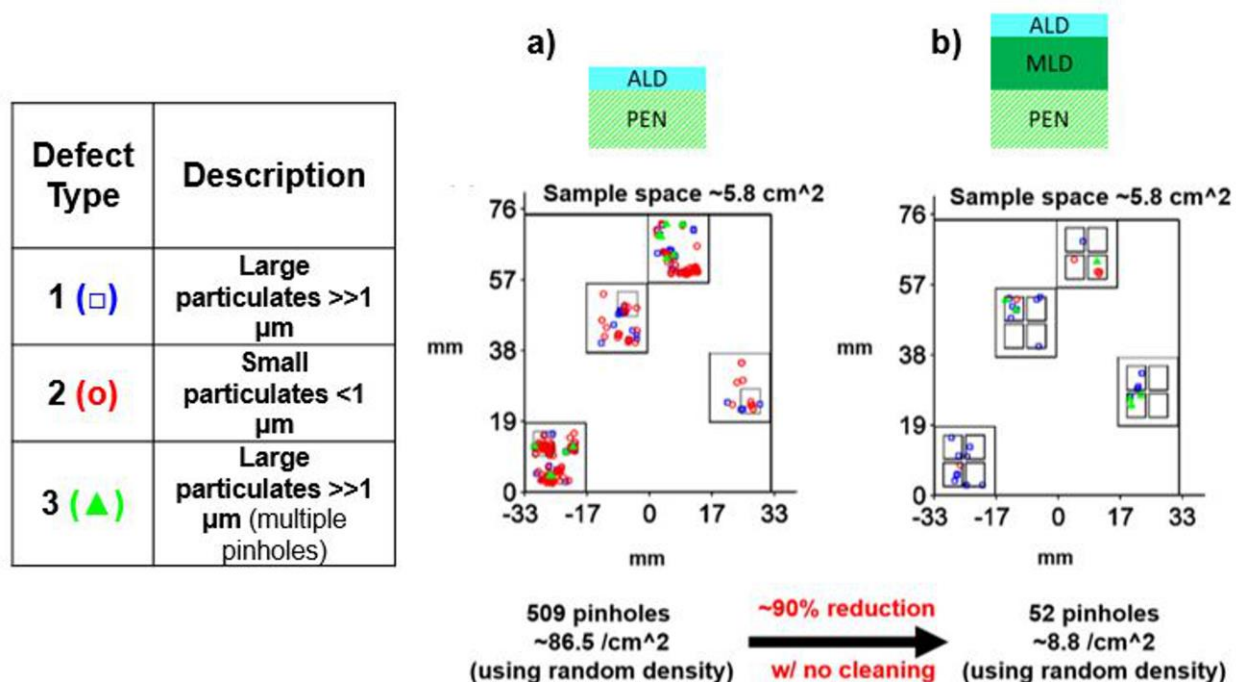
Figure 3.16. Spatial ALD and MLD pinhole maps with the centroid of a defect footprint type represented by a symbol with arbitrary size. (a) Single-layer spatial ALD structure. (b) Spatial ALD and MLD structure. The samples in this figure were not prepared with any special method.

Examples of Type 1 defects in Barrier Structure 1 and 2 are shown in Figure 3.17.
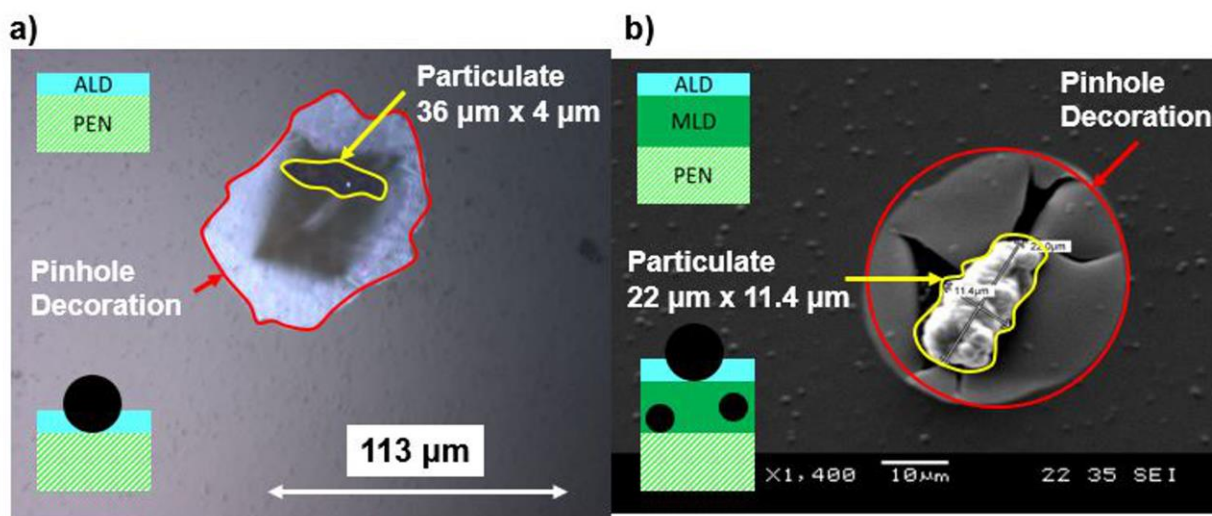
Type 1: Large particulates >> 1 μm

Figure 3.17. Type 1 defects. (a) Optical microscope of a defect in Barrier Structure 1. (b) SEM image of a defect in Barrier Structure 2.

Examples of Type 2 defects in Barrier Structure 1 and 2 are shown in Figure 3.18.
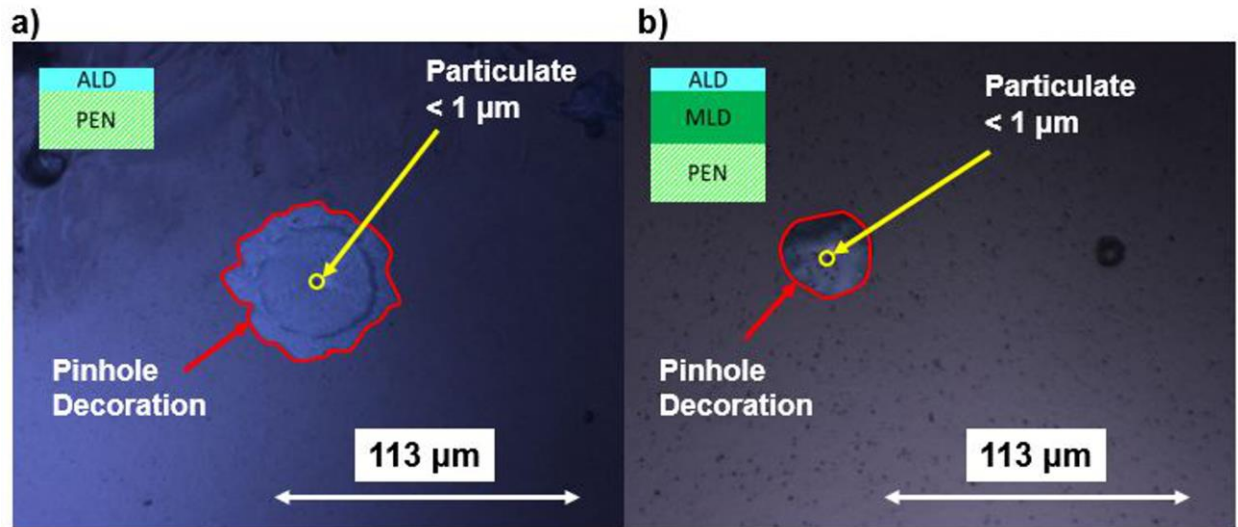
Type 2: Small particulates <1 μm

Figure 3.18. Type 2 defects. (a) Optical microscope of a defect in Barrier Structure 1. (b) Optical microscope image of a defect in Barrier Structure 2.

Examples of Type 3 defects in Barrier Structure 1 and 2 are shown in Figure 3.19.
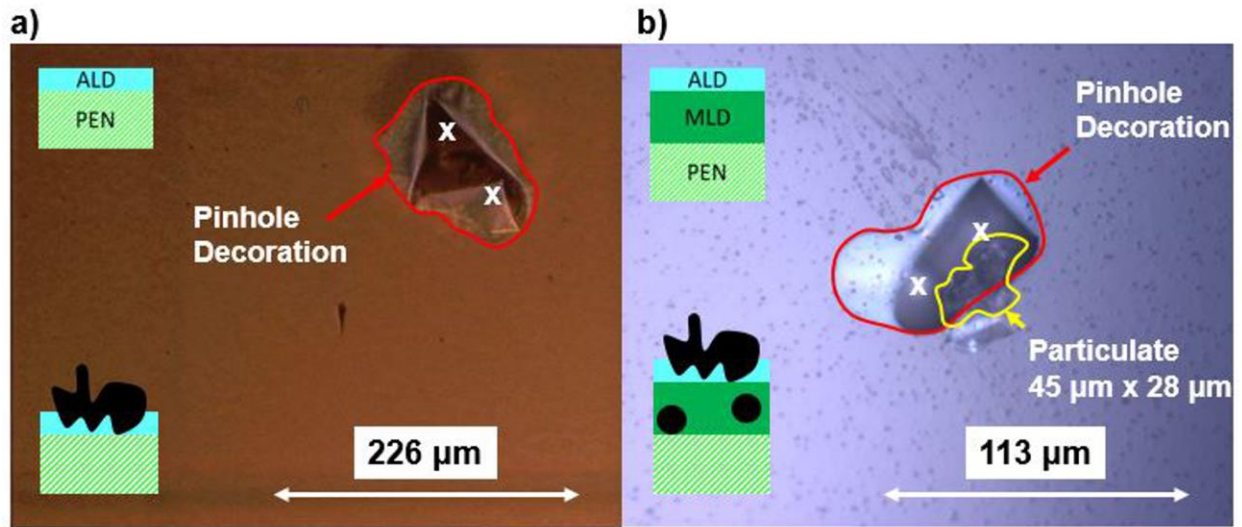
Type 3: Large particulates >>1 µm (multiple pinholes)

Figure 3.19. Type 3 defects. (a) Optical microscope image of a defect in Barrier Structure 1. (b) Optical microscope image of a defect in Barrier Structure 2.

Defect types in Barrier Structure 0-2 are compared and summarized in Figure 3.20. The MLD film reduced Type 2 defects in Barrier Structure 2 by 74x.
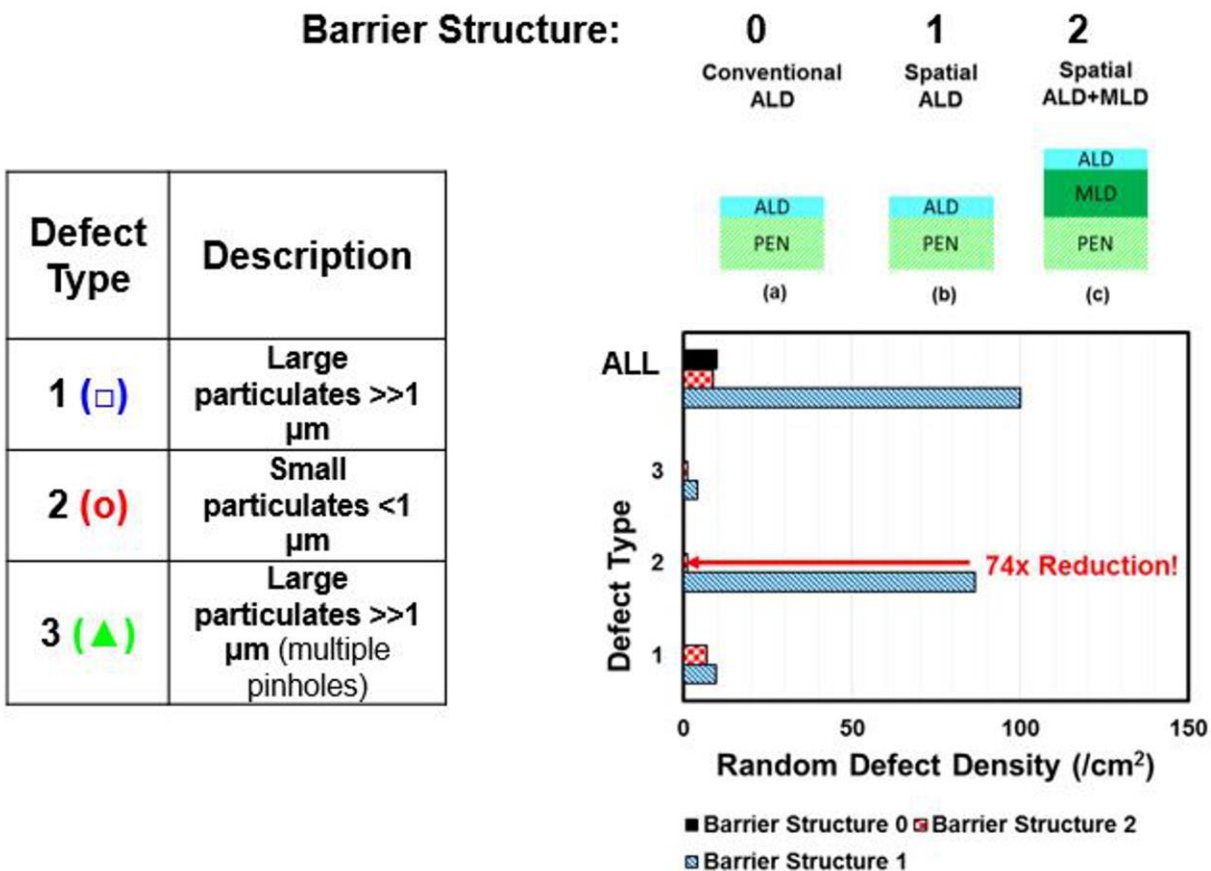
Figure 3.20. Barrier structure comparisons.

3.3.4 Pinhole Cluster Simulations in ALD Films

Using a single random density of defects to determine the number of defects on large complicated designs such as Figure 3.2 is misleading because defects are clustered and not random. Pinhole clusters were simulated over 100 separate 10 x 10 cm surface maps with a (n x m) grid from quadrat area mesh sizes of 6.4 x 10^{-4} cm^2 (n x m = 440 x 349 = 153560 quadrats), 1.6 x 10^{-4} cm^2 (880 x 698 = 614240 quadrats), and 4 x 10^{-5} cm^2 (1760 x 1396 = 2456960 quadrats). This simulation represents 100 fabrication runs. A two-step simulation process was developed. This simulation method incorporates both run-to-run fabrication variations and clustering of defects in the quadrats. Run-to-run fabrication variations can be attributed to different initial levels of

particulate contamination on the substrate before the ALD coating, reactor particulate levels, substrate handling, and any different levels of particulate generation during the ALD coating.

Step 1 (run-to-run variation): Cluster model parameters (r, p) are generated for each run from a pseudorandom sampling of a normal distribution description. For example, the normal distributions generated for r and p in the case of the quadrat area mesh size of 6.4 x 10^{-4} cm^2 are shown in Figure 3.21.
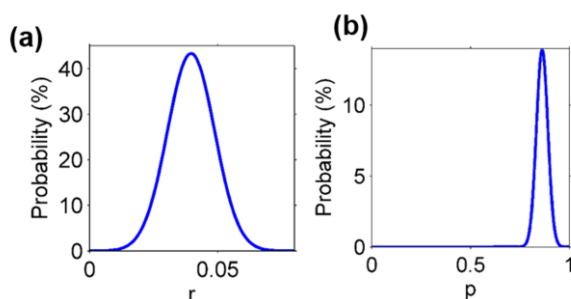
Figure 3.21. Normal distribution representation of the run-to-run variation for a quadrat mesh area size of 6.44 x 10^{-4} cm^2 for (a) r and (b) p.

Step 2 (clustering): Pseudorandom pinhole counts were generated in a (n x m) grid of quadrats by sampling from the cluster distribution generated from the r and p values from step 1. Figure 3.22 shows cluster simulations for the quadrat area mesh sizes of 6.4 x 10^{-4}, 1.6 x 10^{-4}, and 4 x 10^{-5} cm^2. Figures 3.22(a, b) illustrates the run-to-run fabrication variation with the maps with the minimum and maximum number of defects, respectively. Each map is a simulation of a different run. The difference in the degree of clustering and the total number of defects follows that there is a variation in the sample preparation methods and the manufacturing process. A random model does not describe run-to-run variations.
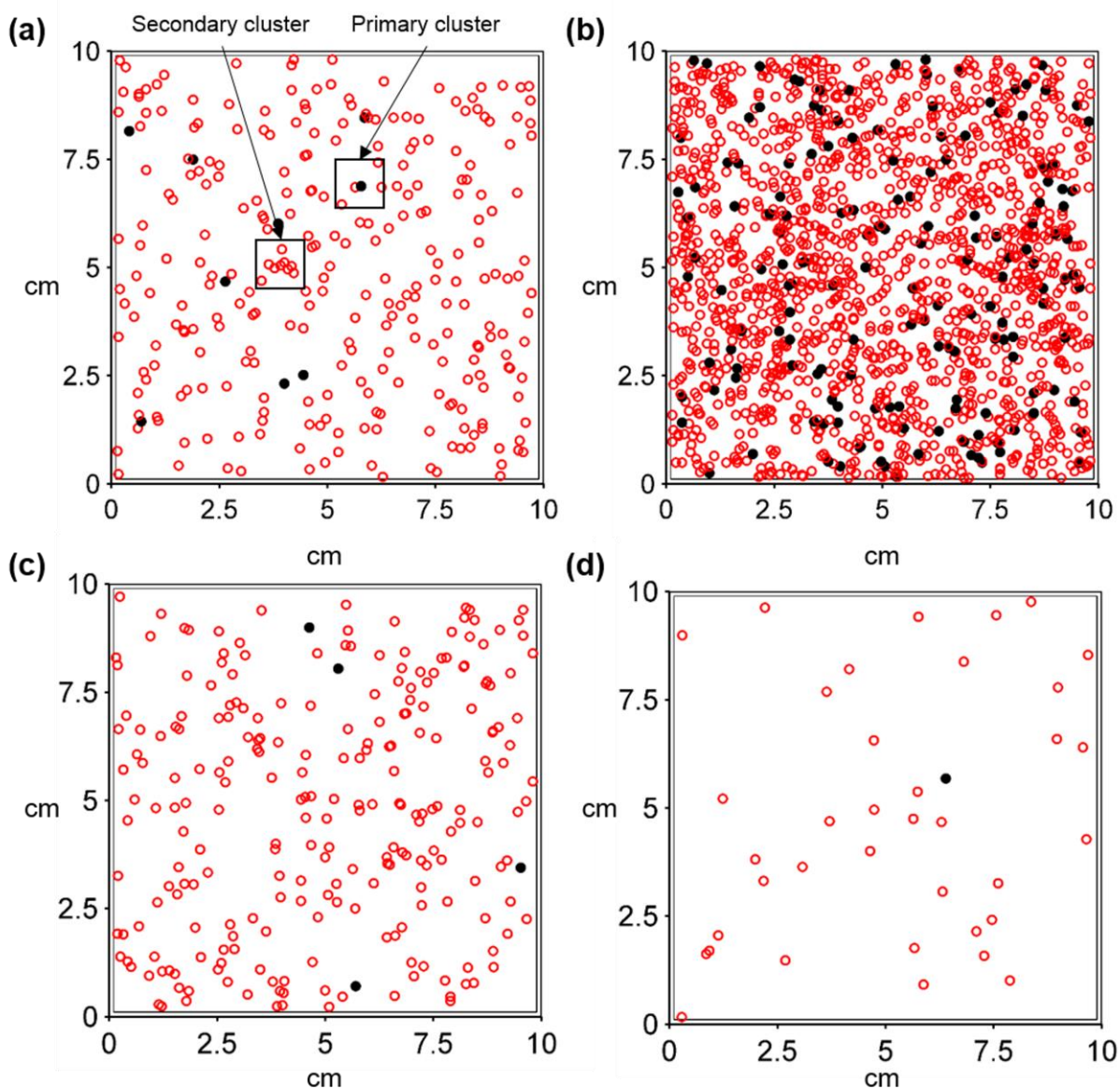
Figure 3.22. Simulated pinhole maps [(a)–(d)] with the centroid of a primary cluster (>1 defect) in a quadrat area represented by a solid circle and one pinhole by an open circle. The maps with the minimum and maximum defects counts for the 6.44 x 10⁻⁴ cm² quadrat area size are represented by (a) and (b), respectively. The minimum defect counts for the 1.6 x 10⁻⁴ cm² and 4 x 10⁻⁵ cm² quadrat areas are shown in (c) and (d), respectively. (a) Quadrat area = 6.4 x 10⁻⁴, total defects = 224, max cluster size = 2, r = 0.01, and p = 0.97. (b) Quadrat area = 6.4 x 10⁻⁴ cm², total defects = 1745, max cluster size = 4, r = 0.05, and p = 0.81. (c) Quadrat area = 1.6 x 10⁻⁴ cm², total defects

= 295, max cluster size = 3, r = 0.03. p = 0.92. (d) Quadrat area = 4 x 10^{-5} cm^2, total defects = 39,

max cluster size = 2, r = 2.93 x 10^{-4}, and p = 0.96.

Maps shown in Figures 3.22(c, d) are for quadrat mesh sizes of 1.6 x 10^{-4} and 4 x 10^{-5} cm^2, respectively. As shown in Figure 3.23, the degree of clustering from simulations is a function of quadrat mesh area size, with the probabilistic cluster model not accurately describing defects below a quadrat mesh area size of 10^{-3} mm^2. A coarse quadrat mesh is not desirable because defects locations cannot be resolved within a quadrat area mesh size. Using a fine quadrat area mesh allows analysis of small ALD features with the smallest area size of 58 x 68 µm.
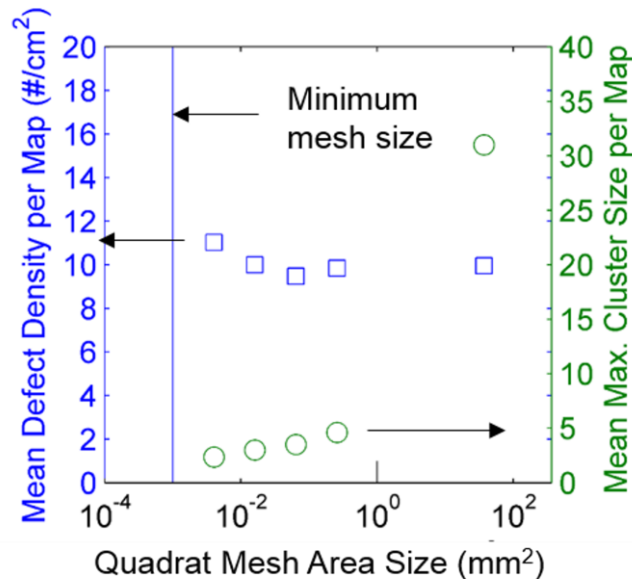
Figure 3.23. Mean defect density and cluster size per map as a function of quadrat mesh area size for cluster model simulations. The cluster model cannot adequately describe defects below a quadrat area mesh size of 10^{-3} mm^2 as shown by the solid vertical line.

The cumulative percentage of devices with respect to defect density for different device sizes were analyzed by overlaying device configurations on the 100 simulated maps from the quadrat area mesh size of 6.4 x 10^{-4} cm^2. A single defect density from the random probabilistic model will

be compared to the simulation maps using the probabilistic cluster model later for a device size of 2.28 x 2.35 cm.

The defect maps were analyzed by partitioning the surface area with devices of the size 9.12 x 9.49 cm (1 device per map, 100 total devices), 2.28 x 2.35 cm (16 devices per map, 1600 total devices), and 0.57 x 0.59 cm (256 devices per map, 25600 total devices). The defect density distribution was determined for each device from the total gross area and from the perimeter (i.e., the outer quadrats = 255 µm), as shown in Figures 3.2(a, c). Defect density is calculated by dividing the number of defects by the size of each different device size. The shape of all the distributions depends on the device size, and shows an increase in the cumulative percentage of devices with a lower defect density with smaller device sizes as shown in Figure 3.24. This increase in percentage of devices with a lower defect density follows that as the devices become smaller, the device size becomes comparable to the secondary cluster size and intercluster spacing, as shown in Figure 3.22. The effect of pinhole clustering on the yield of defect densities of devices is more evident using a real device example to be discussed later.
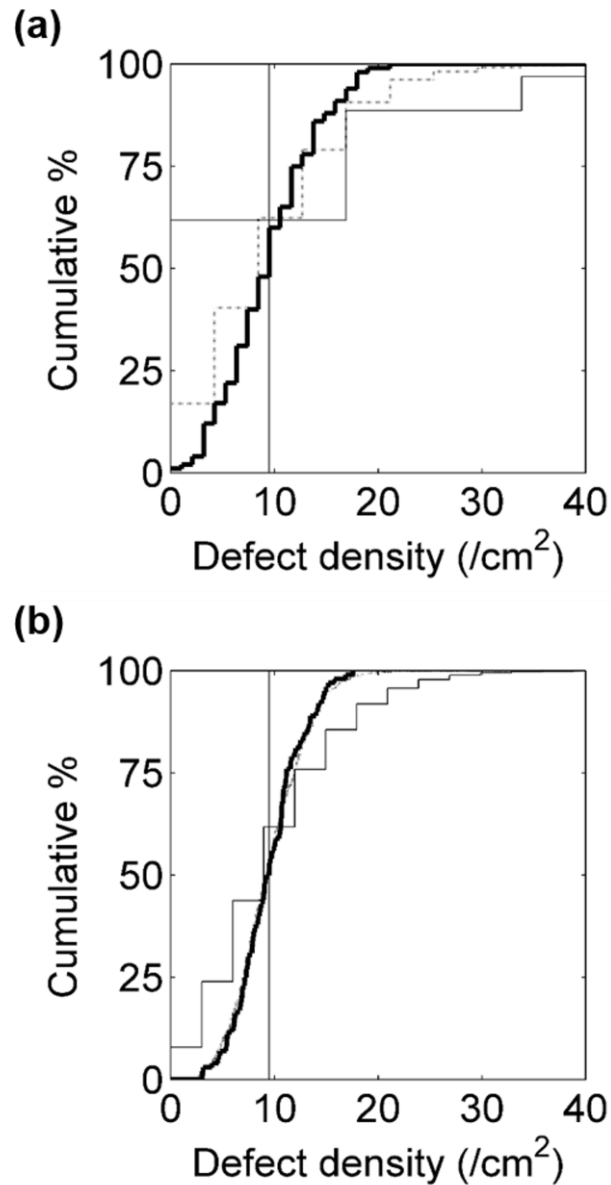
Figure 3.24. Cumulative percentage of a devices with different defect density for (a) perimeter and (b) gross configurations with respect to diced device size (cm x cm): 0.57 x 0.59 (light line), 2.28 x 2.35 (dotted line), and 9.12 x 9.40 (bold line). Device aspect ratio was 1.03. Solid vertical line represents the random defect density value of 9.49/cm^2. The cumulative percentage represents the probability of observing a defect density value or less for all devices of that device size.

3.3.5 Enhanced Nanomanufacturing Design: An Example

To illustrate the effectiveness of this enhanced design method over using a single defect density value from a random model, a flexible thermal ground plane (FTGP)[96,97] heat management device can be used as a case study. For example, the FTGP can be built in two different configurations requiring ALD hermetic sealing over the entire device or the perimeter polymer seal, such as in Figures 3.2(a, c). The FTGP requires a thin film hermetic seal to prevent fluid loss, prevent gain of atmospheric air, and provide an internal hydrophilic coating. Extrinsic rather than intrinsic defects have been shown to be driving factor dictating the useful life of the coatings for applications in the FTGP.[96] The ALD films can be deposited using the same Beneq TFS 200 used in this study. The size of the device of interest is fixed at 2.28 x 2.35 cm with a thickness of 255 µm, and total surface area of 10.96 cm^2. The devices will be analyzed using 100 simulated ALD maps with the quadrat area mesh size of 6.4 x 10^{-4} cm^2. The device is intended to operate at either 60 ^{o}C temperatures or high temperatures applications >60 ^{o}C, with device failure at 40, and 7 defects/cm^2, respectively. The failure criteria and density numbers for the FTGP are courtesy of Dr. Ryan Lewis from Y. C. Lee's group at University of Colorado at Boulder.[98]

A random defect density of 9.48/cm^2 can be obtained by measuring all the defects over the 100 simulations and dividing by the total area examined of 8500.73 cm^2. This method of measuring all the defects implies that the investigator physically etched and imaged all of the samples, as opposed to observing the clustering behavior of defects over a small area ~30 cm^2 and simulating over the 8500.73 cm^2 area using computer software. Table 3.1 summarizes the average number of tolerable defects per device configuration. The number of tolerable defects is determined by multiplying the area needing ALD coating by the tolerable defect density. In the case of the <60 ^{o}C applications, using the old single defect density value from a random model, the average

number of defects is less than the tolerable amount in all cases and more for the >60 °C case. Using

a single defect density, the number of devices that fail or pass (i.e., the device yield) in terms of

tolerable average number of defects is not known.

Table 3.1. Average tolerable number of defects per device configuration and number of defects

calculated by a random density of 9.48/cm^2 are tabulated. The device size is 2.28 x 2.35 cm.

Application	1) Perimeter (0.24 cm^2)	2) Top (5.36 cm^2)	1)+2) (5.6 cm^2)
<60°C	9.6	214.4	224
>60°C	1.68	37.52	39.2
Random: 9.48 /cm^2	2.28	50.81	53.09

The new probabilistic cluster model simulations applied in this study is able to determine how

many devices pass or fail for any device configuration.

Using the enhanced design method developed in this study, the yield of the FTGP device

configurations were determined and tabulated in Table 3.2.

Table 3.2. Number of defects (in bold) and cumulative percentage (in parenthesis) of device configurations.

Perimeter and top	Perimeter
Defect: 0 Yield: (0)	**0** (16.8)
25 (7.6)	**1** (40.3)
39 (29.4)	**2** (62.3)
50 (54.8)	**3** (79.1)
75 (90.7)	**4** (90.6)
100 (99.2)	**5** (96.1)
224 (100)	**9** (100)

Using this method, the cumulative percentage of devices with respect to the total number of defects can be applied to devices with ALD coated patterns. In some applications, the ALD coating is only needed on certain areas, such as a perimeter seal. It is known that in the case of the perimeter only seal: 40.3% of the devices will pass with one average defects (tolerable number = 1.68) for the >60 °C case and 100% of the devices will pass with nine defects (tolerable number = 9.6) for the <60 °C application. The high yield of devices with perimeter yield follows that defects are highly clustered, and as the ALD pattern becomes smaller, less defects will be present in those areas, as discussed in the general results of Figure 3.25.

In the case of the gross area ALD coating: 29.4% of the devices will pass with an average number of defects of 39 for the >60 °C application and 100% will pass 224 defects in the case of the <60 °C application. Figure 3.25 shows the cumulative percentage curves, which were used to create Table 3.2.
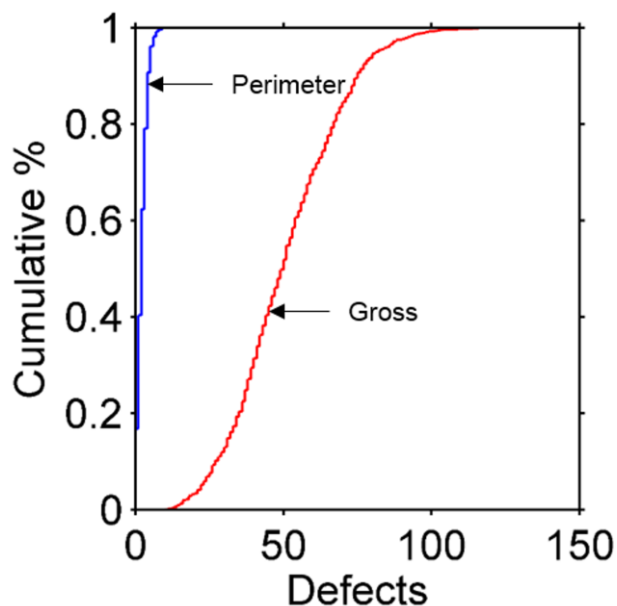
Figure 3.25. Cumulative percentage of devices with respect to defect count for a device size of 2.28 x 2.35 cm for gross and perimeter device configurations. The cumulative percentage represents the probability of observing a defect count value or less for all devices of that device size.

The simulations can be used to design for higher yield by changing device feature sizes that require ALD coatings. For example, if a higher yield was needed in the case of the FTGP, the size of the device may be altered as shown in Figure 3.24, as well as the perimeter thickness.

3.4 Summary and Conclusions

Al_2O_3 films were grown on PEN Q51 under cleanroom conditions using a Beneq TFS 200 ALD reactor tool, and using a R2R ALD and MLD reactor with no sample preparation. Oxygen plasma etching and optical microscopy were used to enlarge and visualize extrinsic pinhole defects over an area about 30 cm^2 in the Beneq TFS 200 tool. The patterns from extrinsic pinhole defects in the ALD films were successfully modeled using a probabilistic cluster model and were shown to be predictive. Simulations using a cluster model were successfully used to design a manufacturable

FTGP requiring thin ALD hermetic coatings. Using a single defect density and assuming a random model, it was determined that for high temperature operation applications >60 °C, the FTGP would not be possible. The new method developed in this study shows that up to 40.3% of the FTGP will not fail. In future studies, a thin film coating tool capable of both molecular layer deposition and ALD will be characterized using the modeling methods developed in this study. In the next **Chapter 4**, we will discuss a measurement technique to investigate the intrinsic quality of coatings.

Chapter 4 Characterization of Thin Film Dissolution in Water with in Situ Monitoring of Film Thickness Using Reflectometry

4.1 Introduction

ALD coatings have been incorporated into many emerging devices requiring a thin, conformal, protective, coating, and have enabled implantable biocompatible[99] nanowire nanoelectronic biological devices[100], microelectromechanical system flow sensors,[101] Si-based transient electronics[28], diffusion barriers,[21] metal encapsulation[4,80,102–105], and cathode protection[81]. Metal films, such as copper, without a protective ceramic barrier have been reported with corrosion rates in water of 1.1 to 2.5 nm/day at room temperature.[30] As a result, nm-scale copper films used in these devices will fully corrode within days in room temperature water. To solve this problem, thin film ALD ceramic coatings may be used as a corrosion barrier to protect thin metal films. However, the ALD coatings themselves are susceptible to dissolution in water over time. As a result, after years of immersion in water a thin ceramic corrosion barrier will no longer adequately protect a metal surface. An accelerated lifetime test is needed to predict slow dissolution rates of ALD coatings in low-temperature water that would otherwise require unacceptable experimental measurement periods of up to years.

ALD films are most often deposited in expensive batch processes, but spatial ALD (S-ALD) is a concept where the ALD precursors are separated in space rather than time, and has enabled manufacturable ALD coatings on large surface areas >> m^2.[26,36] For example, the roll-to-roll Beneq WCS 500 can coat a 500 mm wide substrate with a 25 nm film at a rate of 400,000 m^2/year.[106] Other film deposition techniques such as plasma-enhanced chemical vapor deposition (PECVD), low-pressure chemical vapor deposition (LPCVD), and electron beam (E-beam)

evaporation have been reported as alternative deposition methods to grow SiO_2 corrosion barrier films;[28] However PECVD, LPCVD, and E-beam SiO_2 coatings contain more defects than ALD SiO_2 coatings[28], and cannot provide a thin and conformal barrier on high aspect ratio structures. The intrinsic quality of SiO_2 coatings is a direct result of the deposition process. For example, E-beam deposited SiO_2 coatings in room temperature water have been reported with dissolution rates two orders of magnitude higher than wtg-SiO_2 coatings immersed in water at room temperature.[28] Uniform, conformal, biocompatible, and thin ALD films have begun to be investigated in pure water and under physiological conditions over a range of predetermined pH values and over limited temperatures for TiO_2, Al_2O_3, and SiO_2 thin film coatings.[28,29] ALD SiO_2 films in 37 °C water have been reported with <1 nm of dissolution over a period of time in water for ~15 days.[28] ALD SiO_2 substrate temperatures during deposition have been reported to affect the hydrogen content in the film.[107] Hydrogen content in the film during deposition has been observed to affect the crystalline content of thin SiO_2 films.[108] Bulk SiO_2 films have been measured to be a dissolution-predictable material with no hydrothermal crystallization processes in water temperatures up to the critical point of water.[109] Predictable bulk SiO_2 dissolution properties suggests thin ALD SiO_2 and wet thermally grown SiO_2 (wtg-SiO_2) coatings as good candidates for dissolution-predictable barrier coatings.

ALD SiO_2 forward [k+(T)]] and reverse [(k-(T)] reactions with water are written as

$$SiO_2 + 2H_2O \rightarrow Si(OH)_4 \quad k + (T) \tag{4.1}$$

and

$$SiO_2 + 2H_2O \leftarrow Si(OH)_4 \quad k - (T) \tag{4.2}$$
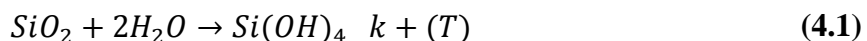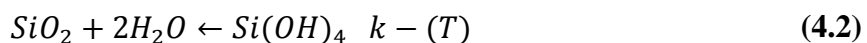
The total rate at which the pseudo first-order reaction[109] proceeds has been described as

$$r_{SiO_2} = k_+(T)\left(a_{SiO_2}\right)\left(a_{H_2O}\right)^2\left(1 - \frac{Q(t)}{K_{eq}}\right) \tag{4.3}$$

where

$$K_{eq} = \frac{k_+(T)}{k_-(T)} = \frac{[P]}{[R]} = \frac{[Si(OH)_4]}{[H_2O]^2[SiO_2]} \tag{4.4}$$

and

$$Q(t) = \frac{k_+(T,t)}{k_-(T,t)} = \frac{[P(t)]}{[R(t)]} \tag{4.5}$$

$$= \frac{[Si(OH)_4](t)}{[H_2O]^2(t)[SiO_2](t)}$$

Quantities in square brackets represent concentrations. The reaction will stop when $Q(t) = K_{eq}$. If the reaction is far from equilibrium, $K_{eq} \gg Q(t)$ then Eq. 4.3 can be expressed as reactant activities and the forward rate constant.

$$r_{SiO_2} = k_+(T)\left(a_{SiO_2}\right)\left(a_{H_2O}\right)^2 \tag{4.6}$$

The activity of a pure solid is 1 and the activity of water can be assumed to be near one because of far from equilibrium conditions. As a result Eq. 4.6 can be expressed as

$$r_{SiO_2} \approx k_+(T) \tag{4.7}$$

Since the rate of the reaction is nearly equal to the rate constant of the forward reaction we would expect an observed linear decrease in film thickness over time. The reaction pathway for SiO_2 dissolution in water was previously described in **Chapter 1**.

Previous studies investigating the dissolution behavior of thin films in water, characterized using ex situ measurements to monitor film thickness, are slow processes conducted at temperatures <100 °C and over periods of up to months.[28,29,69] Using ex situ measurements it is difficult to investigate thin film dissolution dynamics for real systems that do not experience periodic interruptions in the dissolution process. Electrochemical techniques have been used to

measure in situ the dissolution and porosity of thin films in ionic liquids.[4,80,81,102–105] Electrochemical techniques cannot resolve location-dependent dissolution and require conductive electrodes. Optical microscope reflectance measurements were reported as another viable method to measure copper films using normalized average color signals, but this method requires extensive calibration processes per material configuration, making the technique unsuitable for rapid testing of many different types of materials.[110] The optical microscope reflectance technique used to monitor film color intensity assumes a linear relationship of thickness and color intensity during dissolution.[110]

Our study demonstrates an enhanced optical measurement technique with the capability to measure location-dependent dissolution dynamics for different metal and ceramic thin films by monitoring nm-scale film thickness reductions in situ using spectral reflectometry. Reflectometry is used in this study to resolve 150 μm lateral feature sizes and 2 nm thin films. Temperature dependent dissolution rates are obtained in less than 1 day, and are used to predict dissolution rates of thin ceramic films in water at low-temperatures. ALD SiO_2 dissolution rates for films deposited at different substrate temperatures and with/without post-deposition annealing are determined. ALD SiO_2 films deposited at 300 °C are predicted with a slow dissolution rate of 3.7 nm/year at physiological temperatures in water. SiO_2 dissolution measurements in this hyperbaric chamber are near the reported values for the activation energies, ~76-95 kJ/mol, for bulk SiO_2 dissolution in water[109], which suggests our in situ optical measurement technique as a valid method for rapid characterization of the dissolution of thin transparent films.

4.2. Experiment

ALD SiO_2 films were grown in a Beneq TFS 200 reactor tool at a chamber temperature of 150 °C and 300 °C on ~2 μm of wtg-SiO_2 on a Si wafer (El-Cat Inc.). ALD cycle times were 0.2 s AP-

LTO 330 pulse, 6 s purge, 2 s O_3 pulse, and 6 s purge. SiO_2 films were annealed at 400 ºC in a Beneq TFS 200 under vacuum conditions and 1065 ºC in a N_2 environment.

Growth per cycle and dissolution in water of the SiO_2 films were characterized and measured using a reflectometer (FILMETRICS F20-UV). A reflectometer operates by transmitting light to the thin film and measures the reflected light at 512 different wavelengths via a fiber optic bundle as shown in Figure 4.1. The small size and flexible optics allowed simple integration with a translation stage and hyperbaric test chamber.
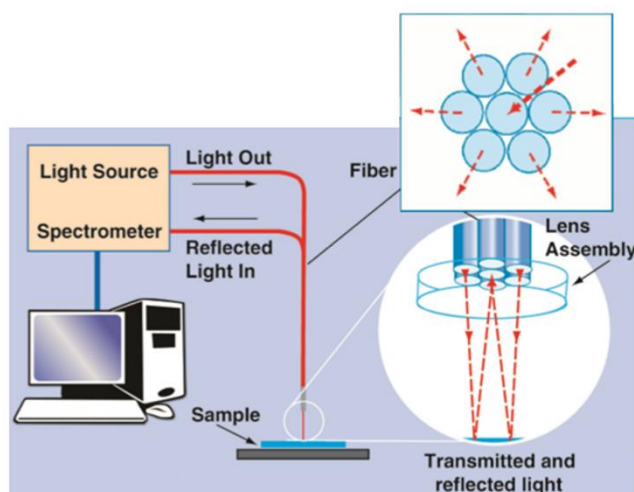
Figure 4.1. Schematic with reflectometer operation is shown. Reproduced with permission from ref. [111]. Copyright 2012 Filmetrics, Inc.

The film thickness range of the reflectometer tool is from 2 nm to 40 μm. The repeatability and accuracy of the reflectometer was ±0.2% as determined in a previous study using a reference Si wafer standard with 724.7 nm of SiO_2 on a Si substrate.[26] Vendor stated error was ±0.4% for thick transparent films. Before immersion, the samples were measured ex situ with the reflectometer, using an optical model of air (medium), thin film (layer), and Si/glass (substrate). The optical model for all in situ measurements was defined as: Water (medium), thin film (layer), and Si/glass (substrate). Si wafer chips were used as a baseline material to calibrate the spectral response of the

reflectometer. For highly reflective materials such as copper, a copper or gold reference was used. The thickness of the film is determined by the reflectometer software from the reflected spectra, in one of two analysis modes: the first is a fast Fourier transform (FFT) mode. The number of peaks in the FFT measurements is defined by:

$$\# \ of \ FFT \ Peaks = \frac{n(n+1)}{2} \ (\textbf{4.8})$$

where n is the number of material layers in the optical model. For example, a film stack with one material layer, such as SiO_2 on a thick Si substrate for samples measured in this study, will produce a single FFT peak. For thin films where the total thickness was in the nanometer range, the thickness was measured by analyzing the pure reflectance spectra. For ex situ measurements, the FFT analysis was performed on reflections measured between wavelengths of 300 and 1100 nm. FILMeasure 7.0 was used to calculate the geometrical thicknesses of films, and the software accounts for all material optical properties in our optical models.

ALD samples were immersed in degassed water (High Performance Liquid Chromatography) in an aluminum hyperbaric chamber with a pressure-rated borosilicate glass window as shown in the cross-sectional view in Figure 4.2.
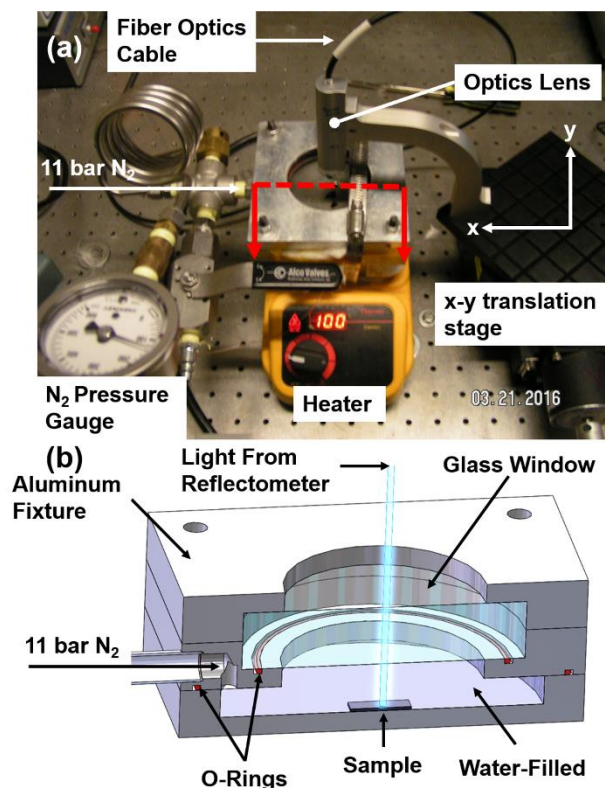
Figure 4.2. (a) Hyperbaric chamber with reflectometer setup for rapid characterization of the dissolution of multiple samples is shown. (b) Cross-sectional view of the aluminum hyperbaric chamber, pressurized to ~11 bar, for superheated water dissolution study is shown. An optical window allows light of $\lambda > 380$ nm to pass from the F20-UV optics to the immersed sample. The hyperbaric chamber is not configured with insulation in (a) for clarity.

A stir bar could be used in this hyperbaric chamber to investigate Reynold's number effects. The wavelengths of light measured by the reflectometer were limited from 400 to 900 nm. Shorter wavelengths in the ultraviolet range could be investigated by using ultraviolet fused silica high-precision windows, but the pressure-rated borosilicate glass used in this study absorbs such ultraviolet light. Longer wavelengths can be successfully used if the optical baseline procedure is done at the approximate water dissolution temperature. A variation in temperature from the baseline can affect the optical measurements due to the vibration mode ($\nu_1 + 3\nu_2$) of water at ~959

nm.[112] The chamber was insulated with fiberglass padding to maintain a constant dissolution temperature and anchored to a hot plate (Thermo Scientific). Typically, the hyperbaric chamber was pressurized with N_2 gas up to an absolute pressure ~11 bar to allow liquid water temperatures up to ~183 ºC. Water dissolution temperatures above 159 ºC were not investigated but were attainable. A fiberglass, insulated, external, thermocouple was used to monitor the chamber temperature at the vertical position of the samples in the chamber. A stepper motor was utilized to translate the optics lens and fiber optics cable over the immersed samples to measure multiple samples and locations on each sample during a single test. As a result, film dissolution rates could be measured in a short period of time <1 day. Typically, the reflectometer measured the film thicknesses every 1-2 minutes.

To test the capability of a reflectometer to accurately measure in situ the dissolution of SiO_2 films, ~2 µm thick wtg-SiO_2 samples were partially masked using Kapton tape during SiO_2 ALD to create a nanometer-scale step height. Step heights were scanned using atomic force microscopy (AFM) before and after dissolution in water (EasyScan 2 AFM). Physical vapor deposited copper samples (EMF Corporation) on borosilicate glass after dissolution were masked and etched (CE 49) to obtain a step height that was measured with profilometry (Dektak 3030).

4.3. Results and Discussion

4.3.1 Characterization of in Situ Measurements

ALD SiO_2 and wtg-SiO_2 films with different thicknesses were measured ex situ and in situ to determine the accuracy of the in situ reflectometry technique to measure nm-scale thickness reductions in the hyperbaric chamber. Ex situ film thickness measurements for ALD SiO_2 films grown on wtg-SiO_2 films for 100, 200, and 500 ALD cycles are shown in Figure 4.3, and were all calculated using FILMeasure 7.0 software.
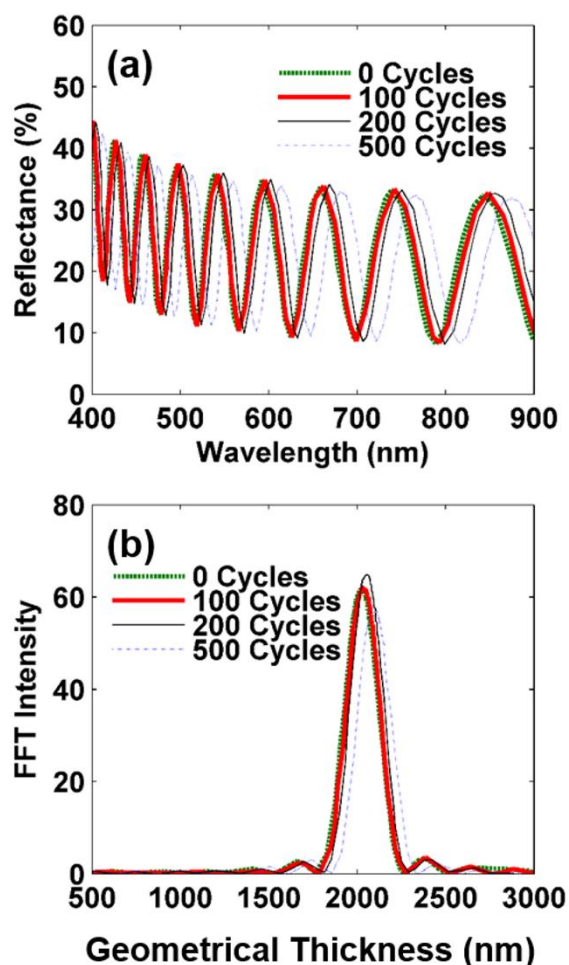
Figure 4.3. (a) Ex situ reflectance spectra for 100, 200, and 500 cycles of ALD SiO$_2$ films (300 ^{o}C deposition) grown on ~2 µm thick wtg-SiO$_2$ is shown. (b) FFT peaks were calculated from the reflectance spectra in (a) using FILMeasure 7.0 and correspond to the total geometrical SiO$_2$ film thicknesses.

The peak in the FFT measurements for each sample corresponds directly to the geometrical thickness of the film. The geometrical thickness accounts for optical properties of the silicon substrate and the SiO$_2$ films. The Cauchy coefficients used for SiO$_2$ coatings were A = 1.44646, B = 0.003735799 µm^2, and C = 7.296645×10^{-6} µm^4. Dissolution rates are derived from measured

changes in the thickness rather than the absolute magnitude itself. A constant error on the layer thickness will therefore not affect our results. A single peak in the FFT measurements is observed and expected based on Equation 4.8. Side lobes in the spectra were expected and were an artifact of the FFT calculation. The 0 ALD SiO_2 datum corresponds to the initial thickness of the wtg-SiO_2 film on which the ALD SiO_2 was grown.

The film thicknesses measured ex situ in Figure 3 were measured in situ as shown in Figure 4.4.
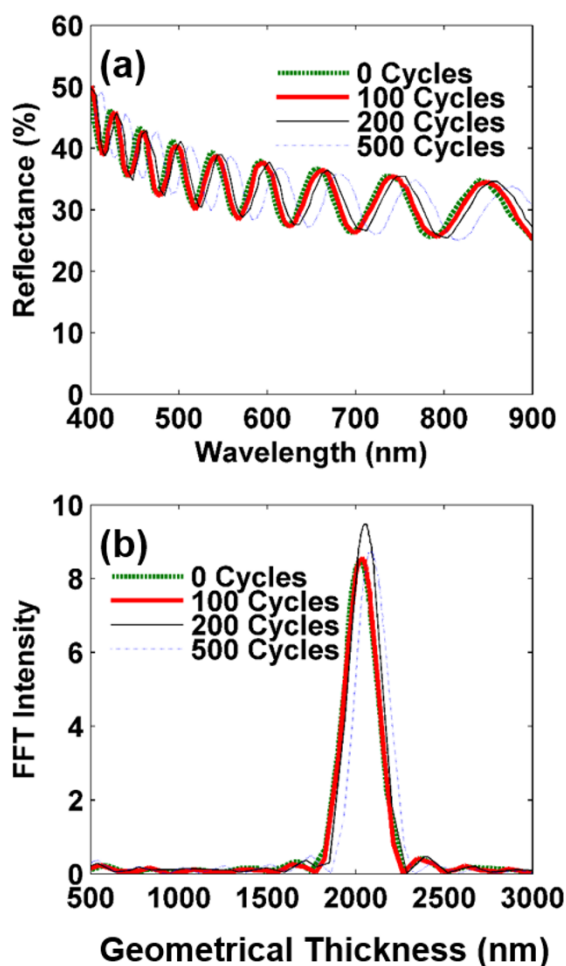
Figure 4.4. (a) In situ reflectance spectra for 100, 200, and 500 cycles of ALD SiO_2 films (300 °C deposition) grown on ~2 µm thick wtg-SiO_2 is shown. (b) FFT peaks were calculated by

FILMeasure 7.0 software from the reflectance spectra in (a) and correspond to the total SiO_2 film thicknesses.

The magnitude of the FFT intensity dropped by ~85%, but the frequency of oscillations in the spectra were not affected. A reduction in magnitude of the reflectance spectra will not affect a FFT geometrical thickness calculation and was expected for light transmitted through a thick glass window and water medium.

The measured thickness of the ALD SiO_2 films grown on ~2 μm wtg-SiO_2 at 300 °C from the 100, 200, and 500 ALD SiO_2 cycles films in Figure 4.3 and Figure 4.4 are shown in Figure 4.5 with 0.14 and 0.15 nm/cycle obtained using in situ and ex situ reflectometry, respectively. A small ~6.9% difference between the growth per cycle obtained using ex situ and in situ measurements may be a result of nonuniformity of the wtg-SiO_2 substrate and standard machine error of ±8 nm (0.4% of the total film thickness being measured). In situ SiO_2 measurements were taken from samples immersed in water at room temperature in the hyperbaric chamber. To confirm the reflectometry measurements, a step height at the ALD SiO_2 and wtg-SiO_2 edge was measured using AFM, with a value of ~15 nm. Using the reflectometer, ALD SiO_2 thicknesses were calculated by subtracting the initial wtg-SiO_2 thickness prior to the ALD process from the post-deposition process thickness measurements. For example, the total oxide thickness for the 100 cycles of ALD SiO_2 was measured ex situ as 2034 nm. The initial wtg-SiO_2 thickness was determined as 2023 nm. As a result, the thickness of the 100 ALD cycle SiO_2 films was ~11 nm. As a result the AFM measurement of ~15 nm was within predicted thickness values of 11 ± 8 nm, validating the in-situ measurement technique to machine accuracy. This growth per cycle is in agreement with reported values of SiO_2 grown films from AP-LTO 330.[107]
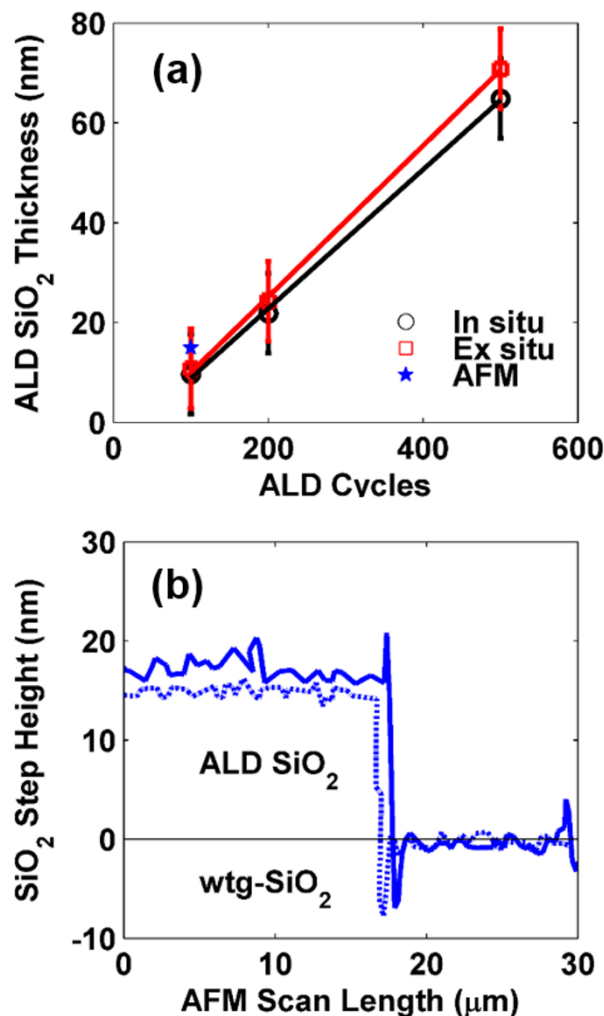
Figure 4.5. Measurement techniques are compared. (a) Growth per cycle of 0.14 (in situ) and 0.15 (ex situ) nm/cycle is shown for ALD SiO_2 films (300 ºC deposition). Error bars are for machine error of ±8 nm. (b) Two step height profiles for 100 cycles of ALD SiO_2 on wtg-SiO_2 were measured using AFM with a value of ~15 nm.

4.3.2 Copper Corrosion

The in situ thickness monitoring technique was first used to measure the corrosion rates of a metal film, such as copper, to obtain a reference to compare to the reported theoretical values in the literature for copper. Without a corrosion barrier, nm-scale copper films will corrode at an

unacceptable rate of ~1.4 nm/day in water at ~22 °C as shown in Figure 4.6. The thicknesses of the copper film with respect to time in Figure 4.6 are considered effective film thicknesses because of observed non-homogeneous corrosion of copper in water.
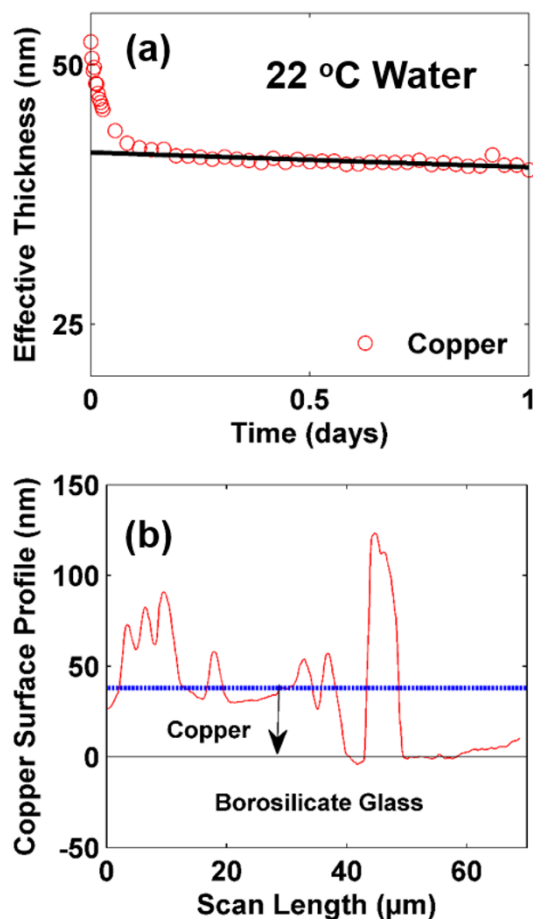
Figure 4.6. (a) Copper corrosion in water at ~22 °C is shown. (b) Step height was measured after 5.3 days of corrosion in water. The large peak is a lift-off artifact. Root mean square (rms) roughness was ~33 nm for the copper surface after corrosion.

Copper in water has been reported to exhibit corrosion rates in room temperature water from ~1.1 to 2.5 nm/day.[30] Corrosion of copper in aerated media has been reported as a diffusion-controlled process.[30] Back-deposition of copper has been reported to decrease the corrosion rate

of copper after an initial high transient corrosion rate.[30] The ~33 nm rms roughening of the copper surface suggests back-deposition, non-uniform corrosion, and formation of isolated oxidized copper in the shape of bumps.[30,69] The copper in Figure 4.6 was further corroded for a total duration of 5.3 days, and measured a final in situ and ex situ effective thickness of 38.4 nm and 37.7 nm, respectively. Profilometry measurements were obtained with an average step height in the range of ~38 nm. The large peak at the step edge is likely a lift-off artifact. The surface of the copper after 5.3 days in water exhibited localized oxidation as shown in Figure 4.7, and was observed as small dark regions. Local oxidation of copper in water has also been observed in another study.[69] Nano-scale copper suffers rapid corrosion at room temperature and is unsuitable for high temperature applications without some form of protective barrier. The initial fast corrosion of copper in water may have been affected by these localized copper oxidation bumps across the film surface.
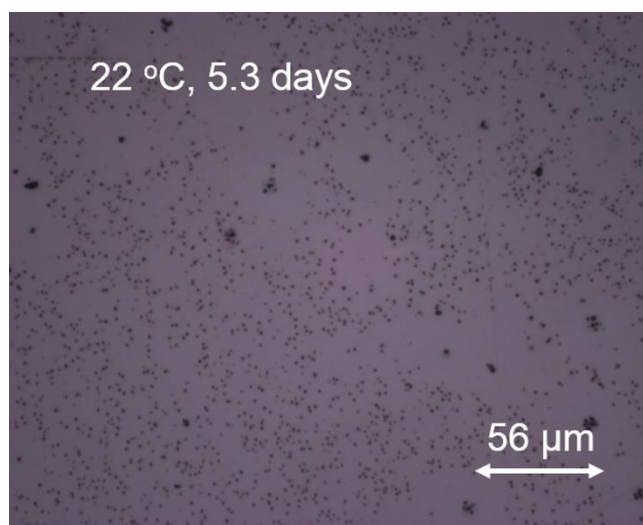
Figure 4.7. Optical microscope image of copper after 5.3 days of corrosion in 22 °C water is shown. Small dark regions are likely due to localized oxidation of copper. Large dark regions are clusters of localized oxidized copper.

4.3.3 SiO₂ Dissolution Rate Dependence on Surface Location

SiO₂ dissolution rates were measured over multiple surface locations on the films to determine the capability of SiO₂ films to provide a uniform layer against rapid corrosion of metals such as copper. ALD SiO₂ and wtg-SiO₂ dissolution in water at ~131 °C is shown in Figure 4.8.
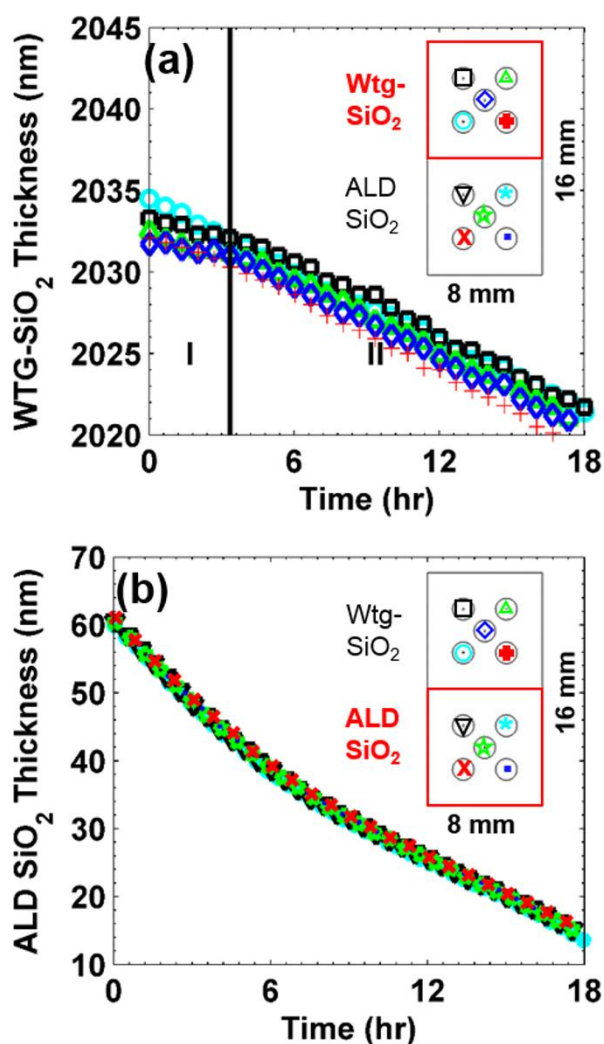
Figure 4.8. Mapping of the dissolution rate in water at ~131 °C for wtg-SiO₂ and ALD SiO₂ films deposited at 300 °C on the same 8 mm x 16 mm Si chip is shown (a) Two distinct dissolution regions (I) and (II) for the wtg-SiO₂ sample on the Si chip is observed. (b) Spatially uniform dissolution for the ALD SiO₂ sample on the Si chip is observed. The insets in (a, b) show the

locations measured on each SiO_2 film on the same Si chip. Each measurement spot was diagonally separated by ~2.1 mm. Spot size of the reflectometer was ~1.5 mm in diameter.

Five different locations on each sample were monitored and showed an entry region (I) for wtg-SiO_2 and a region (II) with uniform dissolution of wtg-SiO_2 films. In region (I) the spatial dissolution of the material was likely slowed by surface defects[113] in the film, which have a non-uniform distribution across the surface.[109] Non-uniform surface roughness of the wtg-SiO_2 film may also affect the initial film dissolution rates. Uniform dissolution was achieved after ~3 nm of dissolution of the wtg-SiO_2 film over a period of ~3.3 hours at the water temperature of ~131 °C. In contrast, the ALD SiO_2 film did not display an initial surface defect and/or surface roughness affected dissolution region (I) in this case, but rather a higher dissolution rate, likely due to incomplete deposition reaction of the organic precursors, which is uniform across the surface. Uniformity of the wtg-SiO_2 film was ~2 nm. Uniformity of the ALD SiO_2 layer was <1 nm as shown in Figure 4.8b.

4.3.4 SiO_2 Dissolution Dependence on Temperature

ALD SiO_2 and wtg-SiO_2 dissolution behaviors at different water temperatures of 101°C, 131 °C, 141 °C, and 159 °C are shown in Figure 4.9. In the case of a dissolution temperature of 141 °C, the wtg-SiO_2 film displayed an enhanced initial dissolution rate likely dominated by surface impurities and/or weakly bonded SiO_2 tetrahedra at the film surface, and is also seen in Figure 4.8. Surface roughness may also affect the initial dissolution rates of wtg-SiO_2 films. ALD SiO_2 film dissolution at a water temperature of 101 °C showed an entry region of ~5 nm with a plausible surface impurity driven dissolution rate due to incomplete surface reactions of the organic AP-LTO 330 precursor and/or surface roughness.
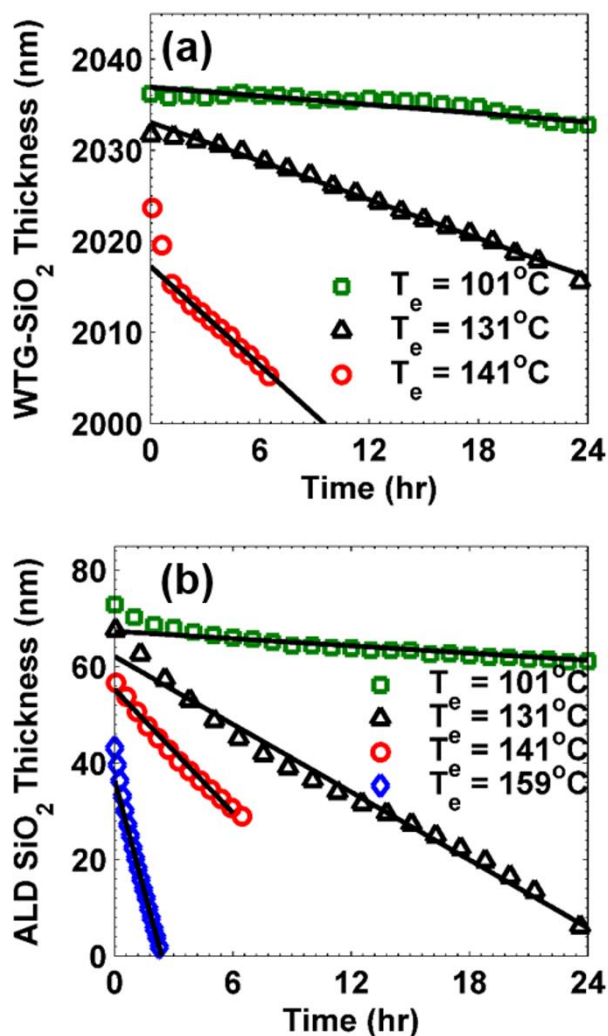
Figure 4.9. Dissolution rate of SiO₂ films in water at different dissolution temperatures in water is shown. (a) Wtg-SiO₂ dissolution rates were calculated with values of 2.5 (101 ℃), 17.0 (131 ℃), and 43.4 (141 ℃) nm/day. (b) ALD SiO₂ (300 ℃ deposition temperature) dissolution rates were calculated with values of 6.0 (101 ℃), 56.3 (131 ℃), 102.6 (141 ℃), and 367.1 (159 ℃) nm/day.

To further investigate the accuracy of the in situ reflectometer to measure the thickness of thin films in real time during dissolution, the final step height between the ALD SiO₂ and the wtg-SiO₂ step edge of the sample that was immersed in water at 101 ℃ from Figure 4.9 was measured to be

70 ± 2.5 nm and 66 ± 4 nm from AFM #1 and AFM #2 scans, respectively, and is shown in Figure 4.10. The 101 °C sample was immersed for 157 hours prior to the two AFM profile scans. The peak at ~11.3 μm in AFM #1 scan is a liftoff artifact as a result of masking the wtg-SiO$_2$ surface during ALD SiO$_2$ deposition. The in situ step height of ~64 ± 8 nm, compares favorably with the AFM scan, and suggests the reflectometer can successfully measure the dissolution of a thin film from start to end of the dissolution process. Using the dissolution rates from Figure 4.9, the final step height should be ~50 ± 8 nm after 157 hours. As a result, the final reflectometer and predicted step heights from the dissolution rates are within the machine error.
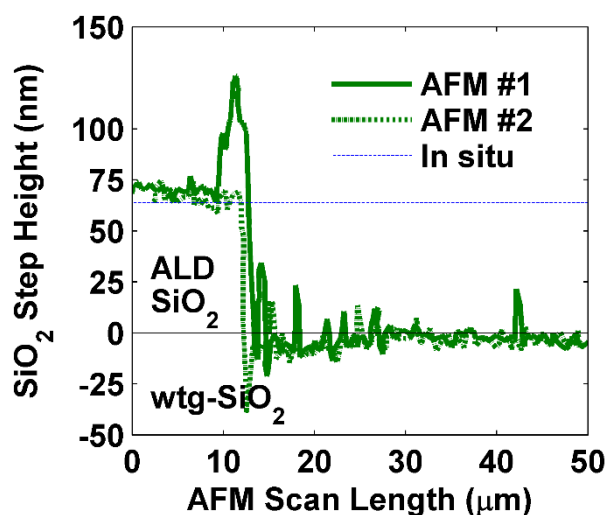
Figure 4.10. AFM scans and in situ measurements of the final step height between ALD SiO$_2$ (300 °C deposition temperature) and wtg-SiO$_2$ from the test in Figure 9 after 157 hours of dissolution in water at 101 °C is shown.

4.3.5 SiO$_2$ Dissolution Dependence on Growth Parameters

The intrinsic quality of the ALD SiO$_2$ coating in terms of dissolution in water at ~100 °C was investigated for ALD SiO$_2$ deposition temperatures of 150 °C and 300 °C, and is shown in Figure 4.11.
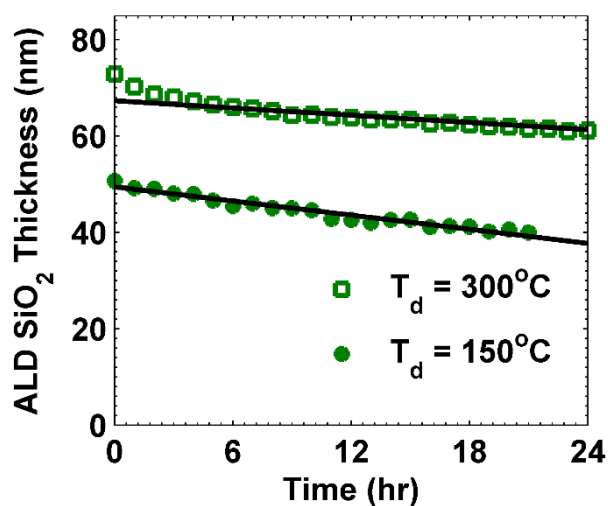
Figure 4.11. Dissolution is shown for ALD SiO$_2$ films in water at ~100 °C with deposition temperatures of 150 °C (circle) and 300 °C (square).

The dissolution rates were 11.7 nm/day and 6.0 nm/day for ALD SiO$_2$ deposited at 150 °C and 300 °C, respectively. The R^2 values for the linear fits were 0.93 and 0.89, respectively.

A substantial increase in dissolution rate of the ALD films with decreasing deposition temperature <175 °C has also been observed for TiO$_2$ films in hot sulphuric acid.[71] For plasma enhanced physical vapor deposition (PECVD) SiO$_2$ films, a reduction in substrate temperature from 300 °C to 150 °C has been reported to result in an increase the hydrogen content in the film from ~6 at.% to 20 at.%.[108] For films with hydrogen content above 3-4 at.%, the remaining fraction of hydrogen will occur as clusters in the film, and form voids in the film.[114] ALD SiO$_2$ films have been reported to display a decrease in refractive index of the film from 1.46 to 1.44, increase in hydrogen content, and decrease in film density with decreasing ALD SiO$_2$ deposition temperatures for the chemistries used in this study.[107] A reduction in the dissolution rate in water of ALD SiO$_2$ deposited at temperatures from 150 °C to 300 °C, suggests that the hydrogen content in the film may influence the water dissolution rate of the material.

4.3.6 SiO₂ Dissolution Dependence on Annealing

The effects of post-deposition annealing ALD SiO$_2$ and wtg-SiO$_2$ films at 400 °C in a vacuum and 1065 °C in N$_2$ are shown in Figure 4.12.
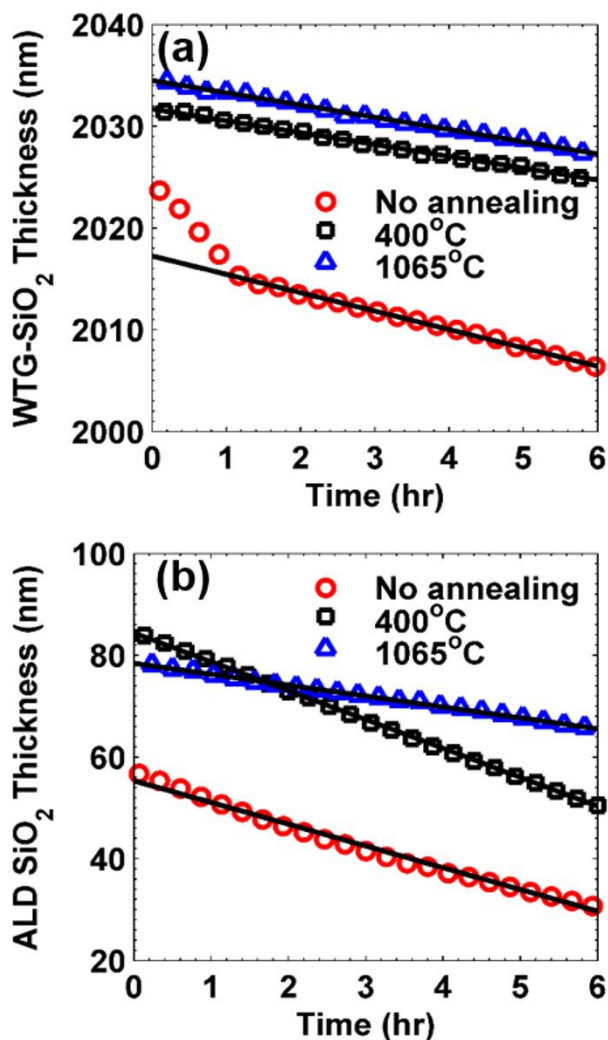
Figure 4.12. Dissolution in water at 141 °C for wtg-SiO$_2$ samples and ALD SiO$_2$ deposited at 300 °C that were not annealed, annealed at 400 °C, and annealed at 1065 °C is shown. (a) Wtg-SiO$_2$ samples. (b) ALD SiO$_2$ samples.

Dissolution rates of the wtg-SiO$_2$ films were unchanged by annealing, but likely showed a reduction in surface impurities manifested by the elimination of a region of increased dissolution

rate near the film surface. The unchanged subsurface dissolution rate follows that in the case of wtg-SiO_2 a material structure change, densification, and/or dehydrogenation process will not occur if the annealing temperature is below the deposition temperature of the film. The dissolution rate of ALD SiO_2 deposited at 300 °C and in water at 141°C was reduced from 4.3 nm/hr to 2.1 nm/hr (51% reduction) by post-deposition annealing ALD SiO_2 at 1065 °C. For reference, the wtg-SiO_2 was observed with a dissolution rate of ~1.8 nm/hr. This reduction in dissolution rate of ALD SiO_2 at annealing temperatures of 1065 °C coincides with a reported onset of film crystallization and a reduction of hydrogen content to below 2 at.% in the films.[108,115,116] The initial deposition thickness of the ALD SiO_2 samples was 70 nm, and the observed increase in film thickness after annealing steps suggest a material structural and/or density change, which has also been observed for annealing Al_2O_3 and TiO_2.[29] Dissolution rates are derived from measured changes in the thickness rather than the absolute thickness itself. A well-behaved linear slope of film thicknesses of the SiO_2 films with time suggests hydrothermal crystallization of the SiO_2 films did not occur during the dissolution tests at chamber pressures of ~11 bar and at a maximum temperature of ~159 °C in water. Reaction paths for structural states of SiO_2 under hydrothermal conditions have been reported.[117] Optical images at 500x of all of the SiO_2 films in this study did not reveal any observable micron size crystallization processes or significant roughening due to exposure to water. In contrast, ALD TiO_2 and Al_2O_3 films were observed to crystallize in water depending on the deposition conditions and dissolution conditions. Dissolution rate reduction for ALD TiO_2 and Al_2O_3 films has been observed for annealing temperatures between 400 °C and 900 °C.[29]

Annealing temperatures of 400 °C in a vacuum did not reduce the dissolution rate of the 300 °C ALD SiO_2 deposited films, but led to an increase of ~33% from 4.3 nm/hr to 5.7 nm/hr at water dissolution temperatures of 141°C. An increase in dissolution rate for the ALD SiO_2 (300 °C

deposition) sample annealed at 400 ºC and immersed in water at 141 ºC suggests that dehydrogenation and resulting formations of clustered voids in the films without concurrent film crystallization and densification due to thermal annealing process will increase the effective active area for dissolution in water.[108] The 400 ºC annealed sample was observe to be less dense than the 1065 ºC annealed sample as indicated by a thicker initial film thickness with respect to the 1065 ºC annealed sample.

The step heights between the initial ALD SiO_2 and wtg-SiO_2 for the annealed samples from Figure 4.12 were measured after ~88 hours of total dissolution in water and are shown in Figure 4.13.
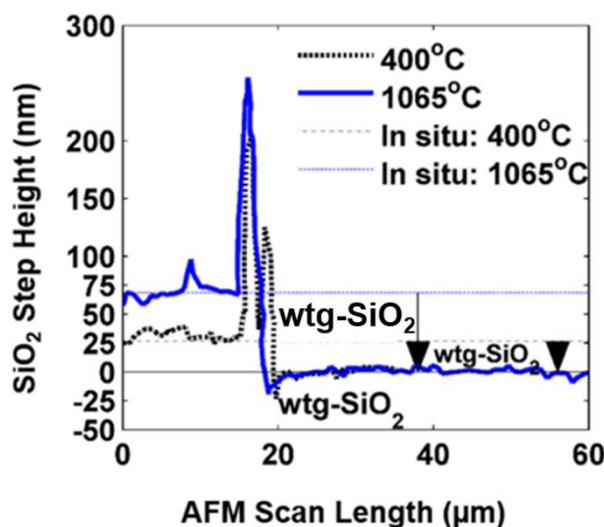
Figure 4.13. AFM scans of 400 ºC and 1065 ºC annealed ALD SiO_2 (300 ºC deposition) samples is shown after immersion in 141 ºC water for 88 hours. ALD SiO_2 is completely removed in both the 400 ºC and 1065 ºC annealed samples, and results in a step height between the wtg-SiO_2 and wtg-SiO_2.

ALD SiO_2 coatings (300 ºC deposition) annealed at 400 ºC and 1065 ºC were both completely removed after 88 hours of immersion in 141 ºC water, and the final step height was between wtg-

SiO$_2$ and wtg-SiO$_2$. The in situ step height of ~68 nm and ~27 nm for the 1065 ºC and 400 ºC annealed samples suggests that the reflectometer can successfully measure the dissolution of annealed thin films from start to end of the dissolution process. For example, in the case of the 400 ºC annealed ALD SiO$_2$ coating, it would take ~15 hours for the ALD film to be completely removed, based off the calculated dissolution rate of 5.7 nm/hr and initial film thickness of ~84 nm from Figure 4.12. After 15 hours, the wtg-SiO$_2$ will have been reduced by ~27 nm based on the dissolution rate of ~1.8 nm/hour measured in Figure 4.12. Thus, the step height of ~27 nm is maintained as the dissolution rate across the step height is now between wtg-SiO$_2$ and wtg-SiO$_2$ for the remainder of the total 88 hour immersion of the sample in water. In the case of the 1065 ºC annealed ALD SiO$_2$ coating, it would take ~37 hours for the ALD film to be completely removed, based off the calculated dissolution rate of 2.1 nm/hr and initial film thickness of ~78 nm from Figure 4.12. After 37 hours, the wtg-SiO$_2$ coating will have been reduced by ~67 nm based on the dissolution rate of ~1.8 nm/hour measured in Figure 4.12. Thus, the step height of ~67 nm is maintained as the dissolution rate is now between wtg-SiO$_2$ and wtg-SiO$_2$ for the remainder of the total 88 hour immersion of the sample in water.

4.3.7 Arrhenius Plots

The dissolution of ALD SiO$_2$ and wtg-SiO$_2$ films with temperature are plotted in Figure 4.14, and both show an experimental Arrhenius behavior written as

$$\log k_+(\text{nm/hr}) = \log(5.0 \times 10^{12}) - \frac{95{,}793}{RT(K)} \quad (\textbf{4.9})$$

and

$$\log k_+(\text{nm/hr}) = \log(3.4 \times 10^{11}) - \frac{90{,}200}{RT(K)} \quad (\textbf{4.10})$$

respectively. R is the gas constant in J/K-mol, and T is the temperature in Kelvin.
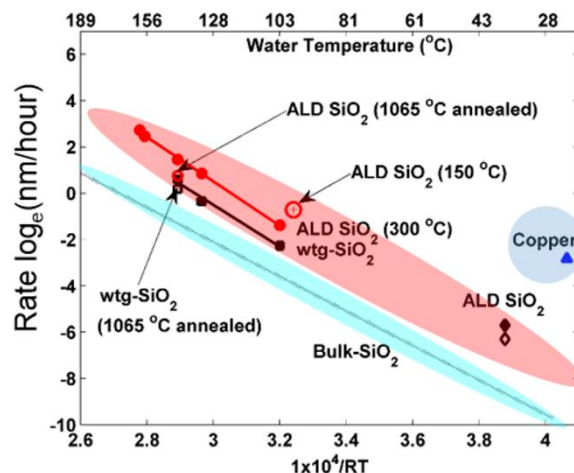
Figure 4.14. Arrhenius plot for SiO₂ materials. ALD SiO$_2$ (closed circle), wtg-SiO$_2$ (closed square), 1065 °C annealed ALD SiO$_2$ (open circle), 1065 °C annealed wtg-SiO$_2$ (open square), ALD SiO$_2$ deposited at 150 °C (large plus-circle) and copper (triangle) measured dissolution rates are shown. Initial and final measured dissolution rates for ALD SiO$_2$ (open diamond, closed diamond, respectively) deposited in a Savannah reactor, (Cambridge Nanotech) with an initial thickness of ~20 nm and ~1 nm of measured dissolution in water with a pH value of 7.4 and temperature of 37 °C, is plotted.[28] The faded line is a SiO$_2$ trend calculated for bulk materials from the literature.[109]

The experimental activation energies for the ALD SiO$_2$ and wtg-SiO$_2$ films were calculated as 95.7 and 90.2 kJ/mol, respectively. The R^2 values for the linear fits were 0.99 and 0.99, respectively. Bulk SiO$_2$ experimental activation energies have been reported for bulk materials with values of 81.9 ± 3.0 and 76.4 ± 6.6 kJ/mol for SiO$_2$ fused silica and pyrolyzed silica, respectively.[109] Activation energies up to 95 kJ/mol have been reported using a linear reaction-controlled model to describe bulk SiO$_2$ dissolution of the tetrahedral ring structure of silica glass, but an additional parabolic rate constant (i.e. diffusion-controlled model) was reported to be used to describe a transient response attributed to the breakup of weakly bonded tetrahedra with respect

to more strongly bonded Si atoms.[118] For crystallite and amorphous cluster models of vitreous silica it has been reported that the material consists of polymorphs of SiO_2 crystallites held together by weak zones of material.[118] These weak zones are quickly attacked and become diffusion limited, and the surface detachment mechanism of the tetrahedra SiO_2 rings becomes the dominant mechanism.[118] For dissolution of Si based glasses with network modifiers, such as Si nitride materials, a mixed reaction control is used to describe the corrosion process due to simultaneous leaching of the network modifiers and destruction of the hydrated glass layer in an acidic solution, and a simultaneous formation of a surface hydroxide layer and destruction of the glass in basic solutions.[119]

Using the calculated activation energy for ALD SiO_2 dissolution rate, it is predicted that the dissolution rate at 37 ^{o}C (i.e. physiological temperatures) would be 3.7 nm/year. ALD SiO_2 deposited in a different study and using a different ALD reactor tool, chemistry, and an unreported substrate deposition temperature, was extrapolated to predict a dissolution rate of ~16 to 29 nm/year, open diamond and closed diamond, respectively, in water at 37 ^{o}C and a pH 7.4 in Figure 4.14.[28] Calculations were completed using the raw data that was measured from a series of reported ex situ measurements consisting of <1 nm of total film dissolution and five data points. In this study we have also observed the existence of dissolution rates within the first few nanometers of the film thicknesses with high initial dissolution rates, as shown in Figure 4.8 and Figure 4.9. In addition, higher dissolution rates were observed for thin films (red oval) as compared to the average values for bulk SiO_2 materials (teal oval) as shown in Figure 4.14.[109]

4.3.8 Al_2O_3 Films Immersed in Water

ALD Al_2O_3 films grown on Si at 300 ^{o}C were measured in this hyperbaric corrosion chamber with a growth per cycle of 0.087 nm/cycle as shown in Figure 4.15. A lower than expected growth

rate of ~0.11-0.12 nm/cycle is likely due to desorption and loss of surface species at the 300 °C deposition temperatures.[37] ALD Al_2O_3 films were also annealed in a N_2 environment for ~30 minutes at 1065 °C. Al_2O_3 films were expected to crystallize at annealing temperatures above 900 °C.[120]
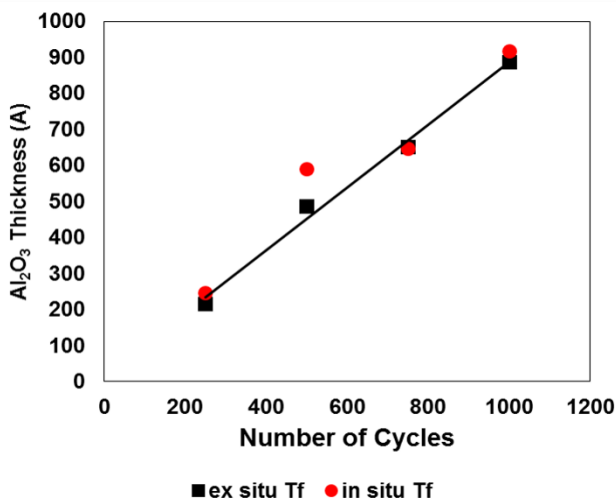
Figure 4.15. Growth rate of ALD Al_2O_3 films deposited at 300 °C was measure with in situ and ex situ reflectometry with a value of ~0.087 nm/cycle.

ALD Al_2O_3 films deposited at 300 °C annealed at 1065 °C were immersed in water at ~55 °C as shown in Figure 4.16. Al_2O_3 films were observed to fail after 2-4 hours after immersion in water at ~55 °C. The Al_2O_3 film that was annealed at a temperature of 1065 °C failed at a time ~2x that of the non-annealed sample. A failure indicates a rapid loss of surface material and concurrent exposure of the base Si substrate. To better understand this failure, a reflectometer was scanned over a step height between an ALD Al_2O_3 film and a bare Si substrate as shown in Figure 4.16a. Correa and coworkers[29] observed the same critical failure phenomena, but rather solved for optical thicknesses by allowing the material density (refractive index) to change. A decrease in refractive index was attributed to a bulk material restructuring and porosity.[29] Abdulagatov and coworkers[69]

observed no failure and no change in refractive index, but rather a smooth thickness reduction over time. We have observed that the Al_2O_3 films catastrophically fail after a critical time immersed in water.
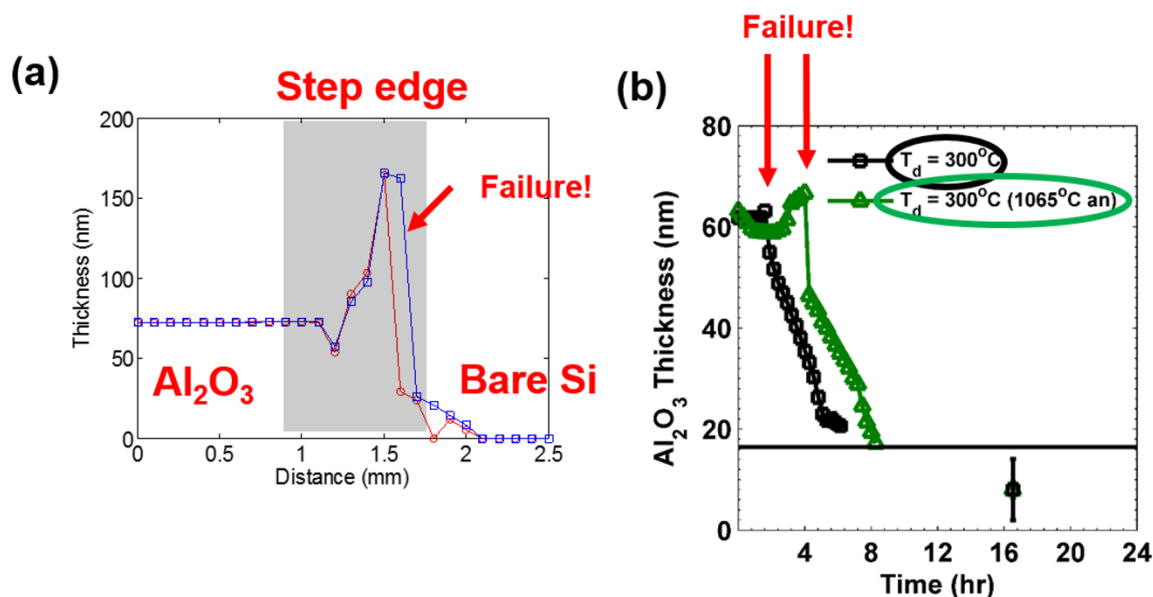
Figure 4.16. (a) Optical thickness measurements for scanning a reflectometer spot from an Al_2O_3 film over a step edge to bare silicon. The Al_2O_3 samples was not immersed in water. (b) Thickness measurements for ALD Al_2O_3 immersed in ~55 ^oC water.

To gain more insight into the failure mechanism of Al_2O_3 films in water at ~55 ^oC, optical microscopy images were taken before and after immersion in water for ~1 day as shown in Figure 4.17. A random pattern of micron size pseudo-hexagonal artifacts and were observed over the immersed sample in Figure 4.17b. Small dark spots were observed. AFM scans across a micron size pseudo-hexagonal artifact circled in yellow in Figure 4.17d indicated the presence of a hole.
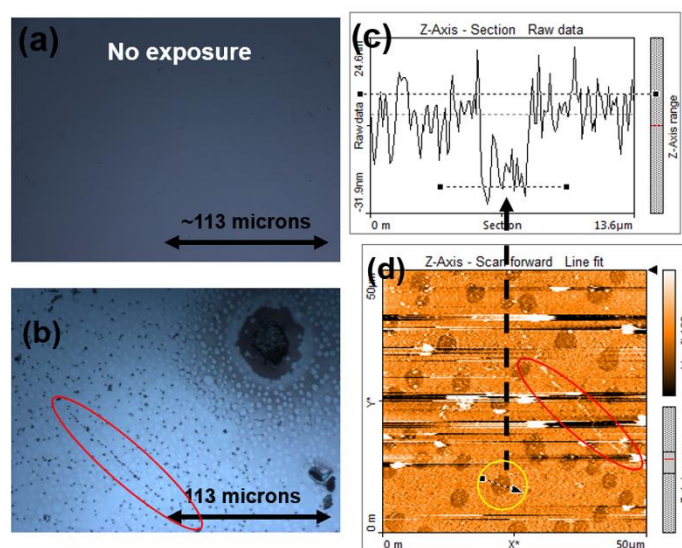
Figure 4.17. Optical microscopy and AFM images for ALD Al_2O_3 deposited at 300 °C. (a) Before immersion in water. (b) Immersed in ~55 °C water for ~1 day. (c) AFM profile across a cleaved crystal from (d) AFM scan.

The mechanisms for Al_2O_3 immersed in water at ~55 °C is likely due to 1) widespread and localized chemical changes of Al_2O_3 to $Al(OH)_3$ gibbsite clusters in the thin film, and followed by pure cleavage of the clusters along the basal plane exposing the bare Si substrate, or 2) back deposition of $Al(OH)_3$ gibbsite formed in solution, and followed by a tearing of the Al_2O_3 film, exposing the base Si substrate. A back deposition mechanism has been proposed by Correa and coworkers.[29] $Al(OH)_3$ clusters have been shown to cleave perfectly on the basal plane as shown in Figure 4.18.[121]
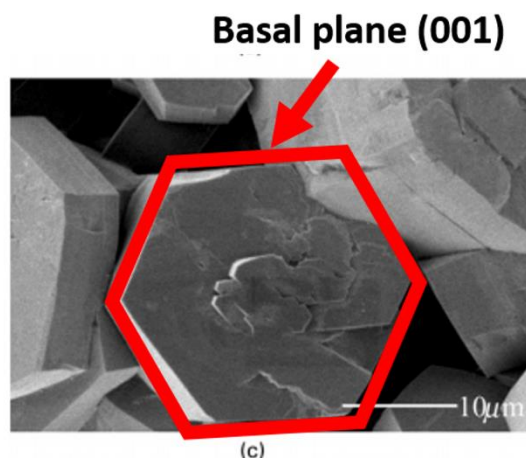
Figure 4.18. Pseudo-hexagonal shaped basal plane of a gibbsite crystal formed in solution.[121]

The mechanisms for failure of ALD Al_2O_3 films immersed in water likely depend on the water temperature. Future studies should investigate different temperatures and film thicknesses.

4.3.9 TiO₂ Immersed in Water

ALD TiO_2 films were grown on the native oxide of silicon chips with different thicknesses, and were measured in this hyperbaric corrosion chamber using reflectometry and AFM as shown in Figure 4.19**.** The growth rate was measured in situ and ex situ with a value of 0.058 nm/cycle for a deposition at 150 °C, which is consistent with the literature for ALD TiO_2 deposited at 120 °C.[69]
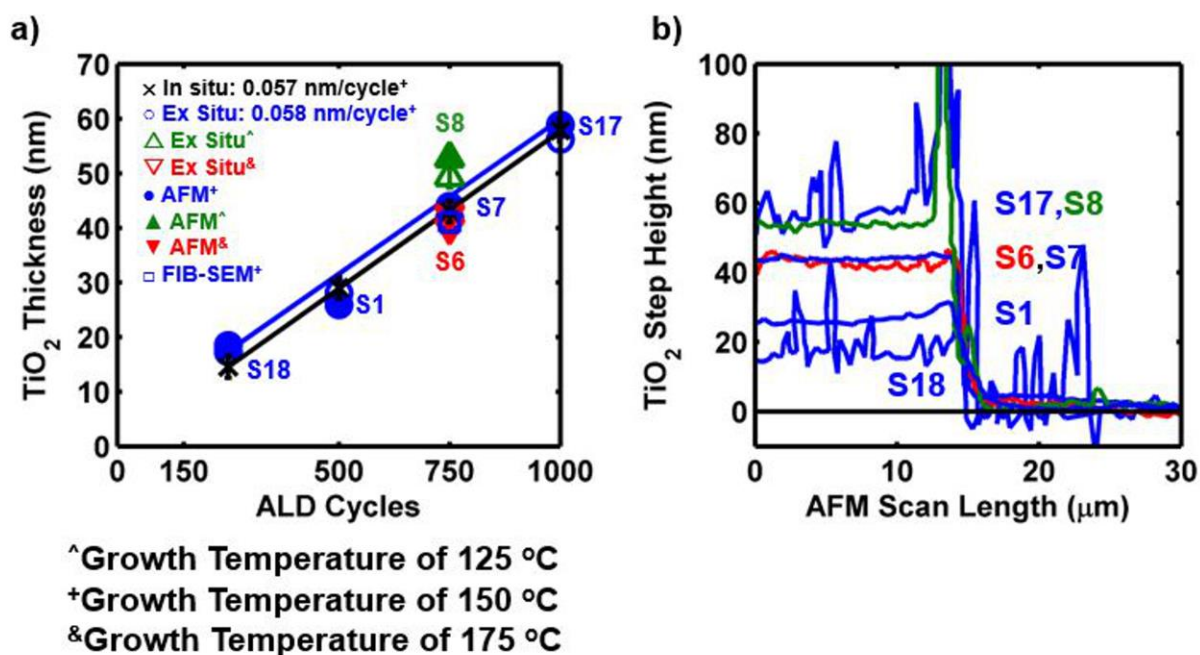
Figure 4.19. (a) Growth per cycle of ALD TiO$_2$ on Si was measured with a value of ~0.058 nm/cycle. (b) AFM scans.

Samples grown at 125 ºC, 150 ºC, and 175 ºC were immersed in 150 ºC water for 12 days and are shown in Figure 4.20**.** The film thickness of the TiO$_2$ samples deposited at 125 ºC were not measurable by the reflectometer after 3 days. The TiO$_2$ samples deposited at 150 ºC and 175 ºC were not observed with any reduction in film thickness. However, the surface of the film was observed with optical roughening as measured be the reflectometer.
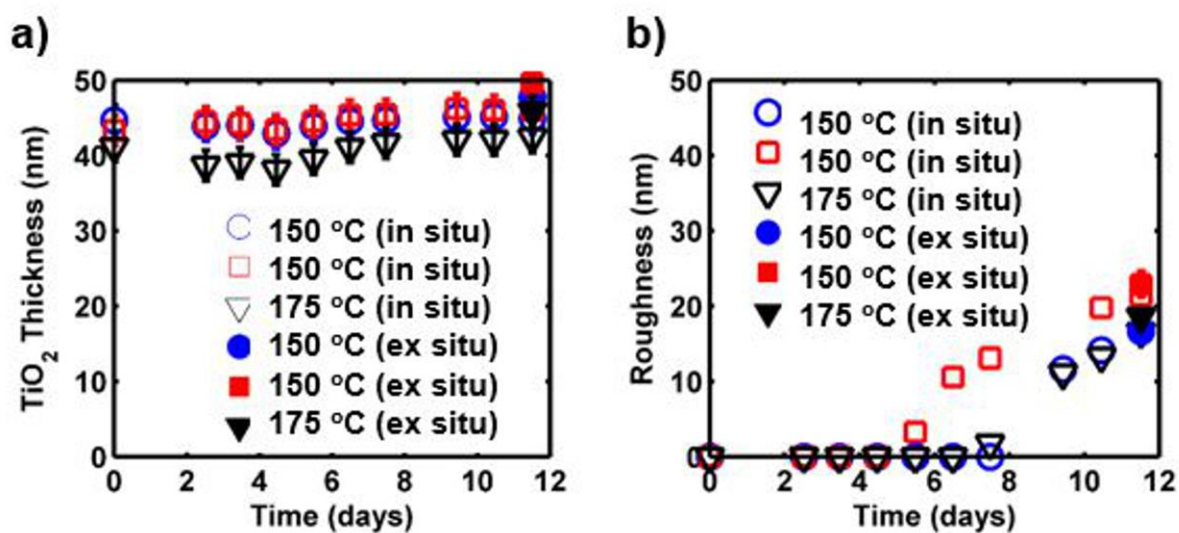
Figure 4.20. (a) Thickness of TiO2 samples over time immersed in 150 ºC water. (b) Optical roughness.

The physical roughness of the TiO₂ samples deposited at 150 ºC before and after immersed in 150 ºC water for 12 days was measured by AFM and shown in Figure 4.21.
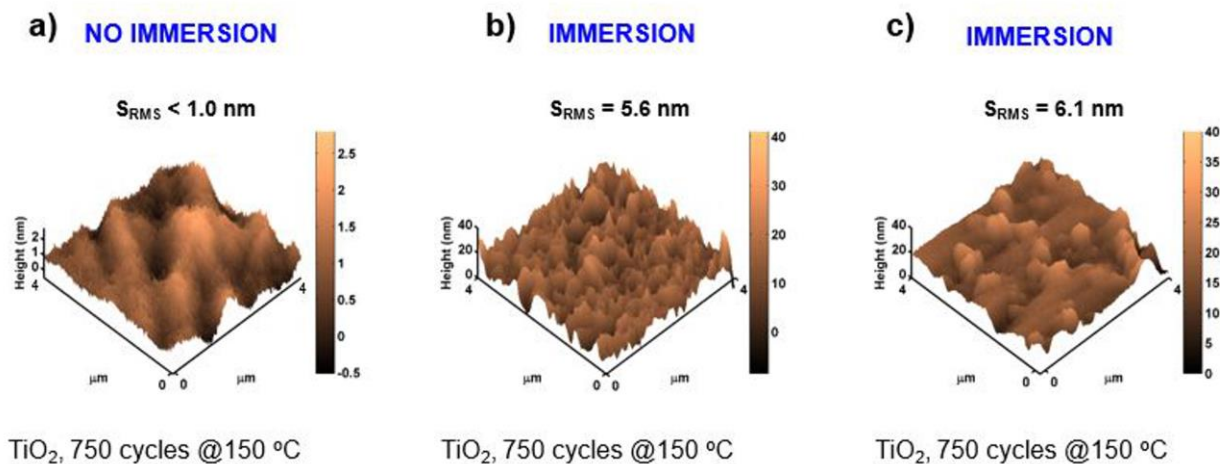
Figure 4.21. AFM scans of TiO₂ deposited at 150 ºC before and after immersion in 150 ºC water. (a) TiO₂ before immersion. (b, c) TiO₂ after 12 days of immersion.

The TiO$_2$ sample deposited at 125 °C before and after water immersion for 12 days at 150 °C is shown in Figure 4.22. The sample after 12 days in 150 °C water showed signs of widespread crystallization.
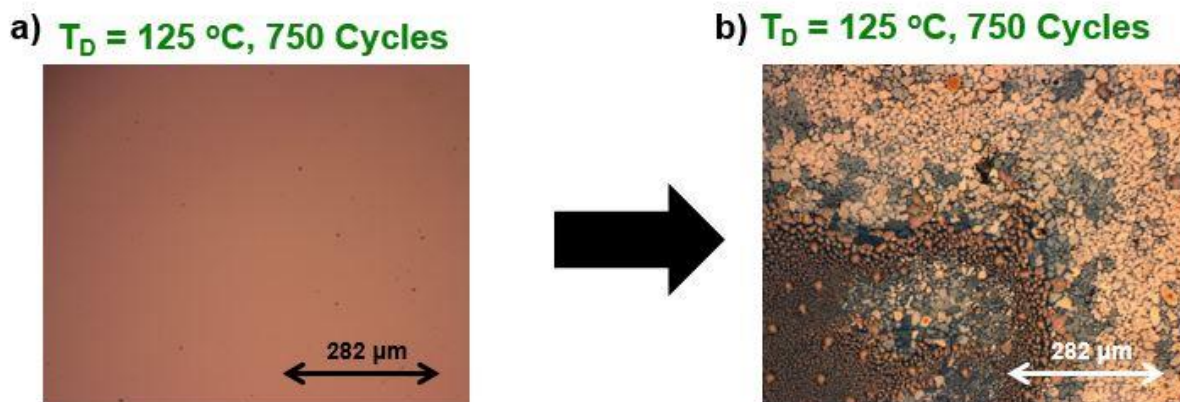
Figure 4.22. Optical micrographs of TiO$_2$ deposited at 125 °C before and after immersion in 150 °C water (a) TiO$_2$ before immersion. (b) TiO$_2$ after 12 days of immersion.

The TiO$_2$ sample deposited at 150 °C before and after water immersion for 12 days at 150 °C is shown in Figure 4.23. The sample after 12 days in 150 °C water did not show any signs of widespread crystallization. However, localized crystallization was observed, and appears as white artifacts in Figure 4.23b.
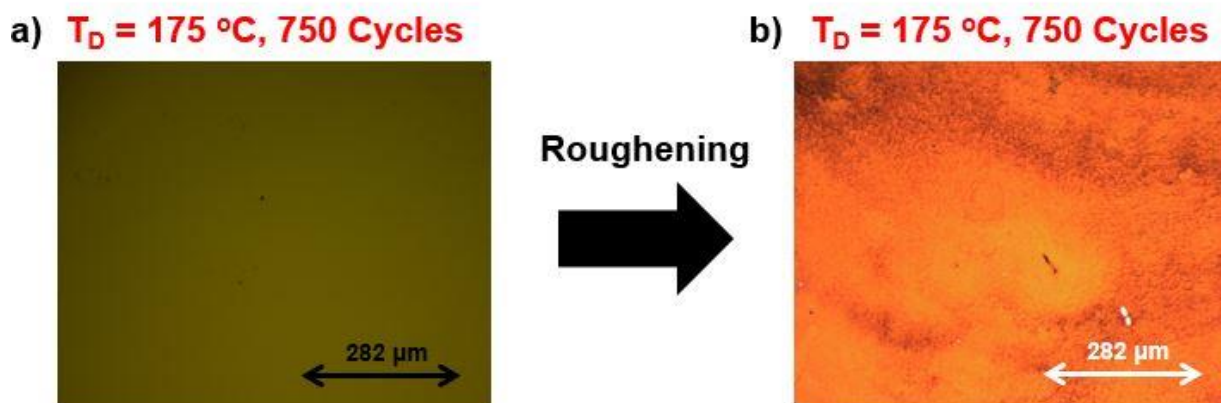
Figure 4.23. Optical micrographs of TiO$_2$ deposited at 150 °C before and after immersion in 150 °C water (a) TiO$_2$ before immersion. (b) TiO$_2$ after 12 days of immersion.

The TiO$_2$ sample deposited at 175 °C before and after water immersion for 12 days at 150 °C is shown in Figure 4.24. The sample after 12 days in 150 °C water did not show any signs of widespread crystallization. However, localized crystallization was observed, and appears as white artifacts.
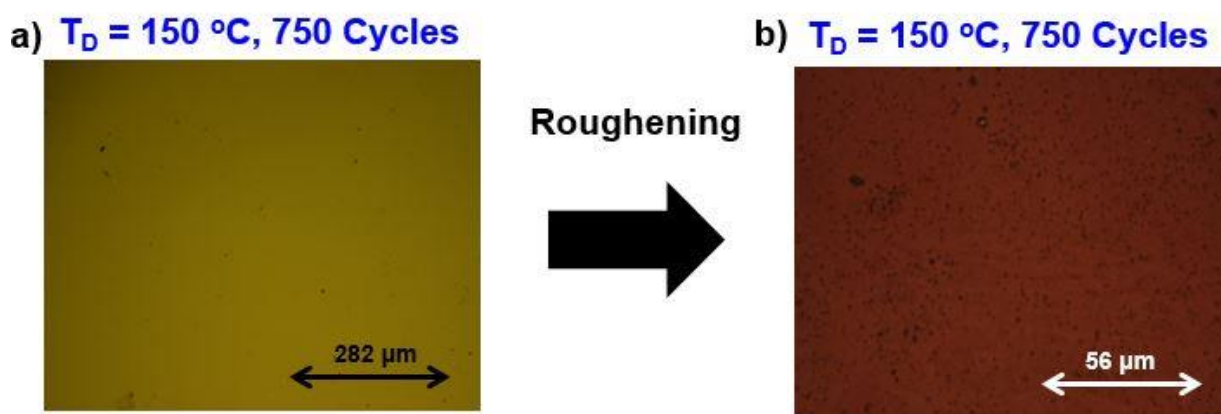
Figure 4.24. Optical micrographs of TiO$_2$ deposited at 175 °C before and after immersion in 150 °C water (a) TiO$_2$ before immersion. (b) TiO$_2$ after 12 days of immersion.

Future work should investigate the consequences of surface roughening. Holes in the ceramic coatings due to surface roughness on silicon could be visualize by XeF$_2$ exposure.

4.4. Conclusions

A rapid thickness measurement technique used to characterize film dissolution in water using in situ reflectometry to monitor film thickness was demonstrated. Metals, such as thin copper films, were observed with an unacceptable corrosion rate of ~1.4 nm/day in water at ~22 °C. ALD SiO$_2$ films were determined to be a dissolution-predictable barrier against corrosion of metals in water over a range of temperatures from 101 °C to 159 °C with measured dissolution rates from 6.0

nm/day to 367.1 nm/day. Wtg-SiO_2 film dissolution in water was measured over a range of temperatures from 101 $^{\circ}$C to 141 $^{\circ}$C with dissolution rates from 2.5 nm/day to 43.4 nm/day. A ~49% reduction in dissolution rate was achieved for ALD SiO_2 films by increasing the deposition temperatures from 150 $^{\circ}$C to 300 $^{\circ}$C. A further 51% reduction in dissolution rate from 4.3 nm/hr to 2.1 nm/hr for ALD SiO_2 films was observed by annealing the films in a N_2 environment at 1065 $^{\circ}$C. The dissolution rate of the annealed ALD SiO_2 and wtg-SiO_2 films in water at 141 $^{\circ}$C was 2.1 nm/hr and 1.8 nm/hr, respectively. Annealing wtg-SiO_2 at 400 $^{\circ}$C and 1065 $^{\circ}$C eliminated a fast transient response of ~8.4 nm/hr observed for the first 9 nm of the film dissolution. Slow and fast transient responses for dissolution of the wtg-SiO_2 in water observed may be due to non-uniform surface defects and/or varying surface roughness. Fast transient responses for ALD SiO_2 may be due to incomplete deposition reaction of the organic precursor AP-LTO 330. Al_2O_3 coatings were observed to fail 2-4 hours of immersion in 55 $^{\circ}$C water. TiO_2 films grown above 120 $^{\circ}$C on silicon with a native oxide did not show any thickness reductions for 12 days immersion in 150 $^{\circ}$C water. However, the TiO_2 coatings roughened.

This study validated an accelerated test method and an in situ optical measurement technique. Dissolution rates of thin films were measured in hours, rather than experimental durations up to years. As a result, we showed that we could predict the dissolution of SiO_2 films in water at physiological temperatures of 37 $^{\circ}$C in hours. We predicted dissolution rates of 3.7 nm/year and 2.2 nm/year for ALD SiO_2 (300 $^{\circ}$C deposition) and wtg-SiO_2, respectively at 37 $^{\circ}$C temperatures. Using our accelerated lifetime test method intrinsic material properties can be investigated and tailored in a short period of time.

Chapter 5 Summary and Future Work

5.1 Summary

In this dissertation work, we demonstrate the feasibility of an atmospheric pressure R2R ALD system for manufacturable, low-cost, and thin ALD coatings. This work focuses on critical issues of operating a R2R ALD system under atmospheric pressure, and also focuses on critical issues related to ALD barrier films. For an atmospheric pressure R2R ALD system, we address precursor carrier gas flows, web speeds, and coating uniformity. For R2R ALD coatings, we develop new characterization tools used to investigate the intrinsic quality of materials using water dissolution as a metric. We discover that extrinsic defects in ALD coatings are clustered and not random.

In **Chapter 2**, spectral reflectometry was implemented as a method for in situ thickness monitoring in a spatial ALD system. Al_2O_3 films were grown on a moving polymer web film at 100 º C using an atmospheric pressure ALD web coating system, with film growth of 0.11-0.13 nm/cycle. The modular coating head design and the in situ monitoring allowed for the characterization and optimization of the TMA and water precursor exposures, purge flows, and web speed. A thickness uniformity of $\pm$ 2 % was achieved across the web. ALD cycle times as low as 76 ms were demonstrated with a web speed of 1 m/s and a vertical gap height of 0.5 mm. WVTR were 10^{-2} g/m^2/day at 37.8 ºC and 100% RH. CVD reactions contribute to <0.1% the growth per cycle of the ALD reactions. Generation of particulates in size range from 0.3-5 μm were observed, and were determined to be a result of excess TMA reacting with ambient moisture. Overall, this atmospheric pressure ALD system with in situ process control demonstrates the feasibility of low-cost, high throughput roll-to-roll (R2R) ALD.

In Chapter 3, partial pinhole defect footprints in atomic layer deposition (ALD) coatings were measured in an area of 30 cm^2 in a Beneq TFS 200 ALD reactor, and these partial defect footprints were represented by a probabilistic cluster model and a random model. Pinhole defect footprints were measured in a R2R ALD and MLD reactor. The cluster model predictive residuals were <10%. A random model had predictive residuals >10%. For irremovable faults, a predictive probabilistic cluster model was used to simulate the total defect footprint over a manufacturing scale surface area of ~1 m^2. Large-area pinhole defect simulations were used to develop an improved and enhanced design method for ALD-based devices. A flexible thermal ground plane (FTGP) device requiring ALD hermetic coatings was used as an example. Using a single defect density value, it was determined that for an application with operation temperatures higher than 60 ^{o}C, the FTGP device would not be possible. The new probabilistic cluster model shows that up to 40.3% of the FTGP would be acceptable. With this new approach the manufacturing yield of ALD-enabled or other thin film based devices with different design configurations can be determined. It is important to guide process optimization and control and design for manufacturability.

In **Chapter 4**, reflectometry was implemented as an in situ thickness measurement technique for rapid characterization of the dissolution dynamics of thin film protective barriers in elevated water temperatures above 100 ^{o}C. Using this technique multiple types of coatings were simultaneously evaluated in days rather than years. This technique enabled the uninterrupted characterization of dissolution rates for different coating deposition temperatures, post-deposition annealing conditions, and locations on the coating surfaces. Atomic layer deposition (ALD) SiO$_2$ and wet thermally grown SiO$_2$ (wtg-SiO$_2$) thin films were demonstrated to be dissolution-predictable barriers for the protection of metals such as copper. A ~49% reduction in dissolution

rate was achieved for ALD SiO_2 films by increasing the deposition temperatures from 150 $^{\circ}$C to 300 $^{\circ}$C. ALD SiO_2 deposited at 300 $^{\circ}$C and followed by annealing in an inert N_2 environment at 1065 $^{\circ}$C resulted in a further ~51% reduction in dissolution rate compared with the non-annealed sample. ALD SiO_2 dissolution rates were thus lowered to values that of wtg-SiO_2 in water by the combination of increasing the deposition temperature and post-deposition annealing. Thin metal films, such as copper, without a SiO_2 barrier corroded at an expected ~1-2 nm/day rate when immersed in room temperature water. ALD Al_2O_3 films deposited at 300 $^{\circ}$C were observed to fail ~2-4 hours after immersion in water at ~55 $^{\circ}$C. ALD TiO_2 deposited at 150 and 175 $^{\circ}$C were observed with no thickness reductions immersed in 150 $^{\circ}$C water up to the measurement period of 12 days. This measurement technique can be applied to any optically transparent coating.

5.2 Proposed Future Work

In this dissertation work we investigate a conventional Beneq TFS 200 reactor, an atmospheric pressure R2R ALD reactor, and a R2R ALD and MLD reactor for manufacturable ultrabarrier coatings. Based on this dissertation, we have identified future studies as the following.

5.2.1 Predictive Cluster Modeling

In this dissertation work the existence of different types of defect partial footprints in ALD and ALD/MLD bilayer coatings on polymeric substrates was discovered. A cluster model was shown to be more predictive than a random model. We suggest future studies investigate the predictive ability of the cluster model over a wider range of quadrat areas. For example, quadrat areas above 0.2553 mm^2 and smaller than 0.0156 mm^2 were not investigated in this dissertation work. Future work is needed to determine if the shape of the quadrats affects the cluster modeling. In this dissertation work rectangular quadrats were used. Lastly, it is advised that future work investigate a larger sample size for the cluster model.

5.2.2 Moisture Ultrabarriers

Extrinsic defect partial footprints in a R2R ALD and MLD reactor was measured to be <10 /cm^2. Further studies are recommended to investigate different MLD and ALD thickness. First, a simple defect footprint density can be used as a metric to compare different MLD and ALD thicknesses.

Intrinsic qualities of single-barrier ceramic films are suggested for investigation. Water dissolution and/or WVTR measurements can be used to identify reactor temperature, purge gas flow rate, and web speed effects. After investigating the parameters required to coat a single bilayer of ALD and MLD, it is suggested that multiple bilayers of ALD and MLD in terms of WVTR be investigated.

5.2.3 Corrosion Ultrabarriers

In this dissertation work we demonstrated a hyperbaric corrosion chamber with in situ monitoring of the film thickness. We observed no change in film thickness for ALD TiO_2 films in water at 150 ^{o}C. We suggest investigating ALD TiO_2 at different temperatures in water and over longer periods immersed in water. Localized crystallization observed in the ALD TiO_2 coatings immersed in water is suggested for more studies. Different configurations of laminates and alloys of ALD SiO_2 and TiO_2 films are suggested for studies. ALD SiO_2 films were observed to not crystallize and may inhibit top down crystallization in the ALD TiO_2 layer.

Bibliography

(1)   Schiller, N.; Fahlteich, J.; Fahland, M.; Straach, S. Transparent Barrier Coatings on Polymer Films. In *AIMCAL Fall Technical Conference 2009 and 23rd International Web Coating Conference*; 2009.

(2)   Wong, F.; Fung, M.; Tao, S.; Lai, S.; Tsang, W.; Kong, K.; Choy, W.; Lee, C.; Lee, S. Long-Lifetime Thin-Film Encapsulated Organic Light-Emitting Diodes. *J. Appl. Phys.* **2008**, *104*, 014509.

(3)   Garner, S.; Merz, G.; Tosch, J.; Chang, C.; Marshall, D.; Li, X.; Matusick, J.; Lin, J.; Kuo, C.; Lewis, S.; Kang, C.; Shih, J.; Lu, M. Flexible Glass Substrates for Roll-to-Roll Manufacturing. *Corning Tech. Inf. Pap.* **2011**.

(4)   Potts, S.; Schmalz, L.; Fenker, M.; Díaz, B.; Światowska, J.; Maurice, V.; Seyeux, A.; Marcus, P.; Radnóczi, G.; Tóth, L.; Kessels, W. Ultra-Thin Aluminium Oxide Films Deposited by Plasma-Enhanced Atomic Layer Deposition for Corrosion Protection. *J. Electrochem. Soc.* **2011**, *158*, C132–C138.

(5)   Graff, G.; Williford, R.; Burrows, P. Mechanisms of Vapor Permeation through Multilayer Barrier Films: Lag Time versus Equilibrium Permeation. *J. Appl. Phys.* **2004**, *96*, 1840–1849.

(6)   Yu, D.; Yang, Y.; Chen, Z.; Tao, Y.; Liu, Y. Recent Progress on Thin-Film Encapsulation Technologies for Organic Electronic Devices. *Opt. Commun.* **2016**, *362*, 43–49.

(7)   Lin, H.; Xu, L.; Chen, X.; Wang, X.; Sheng, M.; Stubhan, F.; Merkel, K.; Wilde, J.

Moisture-Resistant Properties of SiNx Films Prepared by PECVD. *Thin Solid Films* **1998**, *333*, 71–76.

(8) Kim, L.; Kim, K.; Park, S.; Jeong, J.; Kim, H. Al_2O_3 /TiO_2 Nanolaminate Thin Film Encapsulation for Organic Thin Film Transistors via Plasma-Enhanced Atomic Layer Deposition. *ACS Appl. Mater. Interfaces* **2014**, *6*, 6731–6738.

(9) Meyer, J.; Görrn, P.; Bertram, F.; Hamwi, S.; Winkler, T.; Johannes, H.; Weimann, T.; Hinze, P.; Riedl, T.; Kowalsky, W. Al_2O_3/ZrO_2 Nanolaminates as Ultrahigh Gas-Diffusion Barriers-A Strategy for Reliable Encapsulation of Organic Electronics. *Adv. Mater.* **2009**, *21*, 1845–1849.

(10) Carcia, P.; McLean, R.; Reilly, M. Permeation Measurements and Modeling of Highly Defective Al_2O_3 Thin Films Grown by Atomic Layer Deposition on Polymers. *Appl. Phys. Lett.* **2010**, *97*, 221901.

(11) Meyer, J.; Schmidt, H.; Kowalsky, W.; Riedl, T.; Kahn, A. The Origin of Low Water Vapor Transmission Rates through Al_2O_3/ZrO_2 Nanolaminate Gas-Diffusion Barriers Grown by Atomic Layer Deposition. *Appl. Phys. Lett.* **2010**, *96*, 243308.

(12) Sobrinho, A.; Czeremuszkin, G.; Latrèche, M.; Wertheimer, M. R. Defect-Permeation Correlation for Ultrathin Transparent Barrier Coatings on Polymers. *J. Vac. Sci. Technol. A Vacuum, Surfaces, Film.* **2000**, *18*, 149.

(13) Visser, R. *Barix Multilayers: A Water and Oxygen Barrier for Flexible Organic Electronics*; 2006.

(14) Cros, S. *Barrier Materials & Encapsulation for OPV*.

(15) Lewis, J.; Weaver, M. Thin-Film Permeation-Barrier Technology for Flexible Organic Light-Emitting Devices. *IEEE J. Sel. Top. Quantum Electron.* **2004**, *10*, 45–57.

(16) Kim, H.; Kim, S.; Kim, D.; Kang, J.; Kim, M.; Cho, W. Thin Film Passivation of Organic Light Emitting Diodes by Inductively Coupled Plasma Chemical Vapor Deposition. *Thin Solid Films* **2007**, *515*, 4758–4762.

(17) Huang, W.; Wang, X.; Sheng, M.; Xu, L.; Stubhan, F.; Luo, L.; Feng, T.; Wang, X.; Zhang, F.; Zou, S. Low Temperature PECVD SiNx Films Applied in OLED Packaging. *Mater. Sci. Eng. B Solid-State Mater. Adv. Technol.* **2003**, *98*, 248–254.

(18) Yan, M. *Ultra-High Barrier Plastic*; 2008.

(19) Fahlteich, J. *Transparent High Barrier Film for Organic Electronics Roll-to-Roll Pillot Production*.

(20) Moro, L.; Krajewski, T.; Rutherford, N.; Philips, O.; Visser, R.; Gross, M.; Bennett, W.; Graff, G. L. Process and Design of a Multilayer Thin Film Encapsulation of Passive Matrix OLED Displays. *Org. Light Emit. Mater. Devices VII* **2004**, *5214*, 83–93.

(21) Groner, M.; George, S.; McLean, R.; Carcia, P. Gas Diffusion Barriers on Polymers Using Al_2O_3 Atomic Layer Deposition. *Appl. Phys. Lett.* **2006**, *88*, 51907.

(22) Dameron, A.; Davidson, S.; Burton, B.; Carcia, P.; McLean, R.; George, S. Gas Diffusion Barriers on Polymers Using Multilayers Fabricated by Al_2O_3 and Rapid SiO_2 Atomic Layer Deposition. *J. Phys. Chem. C* **2008**, *112*, 4573–4580.

(23) Kim, H.; Singh, A.; Wang, C.; Fuentes-Hernandez, C.; Kippelen, B.; Graham, S. Experimental Investigation of Defect-Assisted and Intrinsic Water Vapor Permeation through Ultrabarrier Films. *Rev. Sci. Instrum.* **2016**, *87*, 033902.

(24) Dickey, E.; Barrow, W. High Rate Roll to Roll Atomic Layer Deposition, and Its Application to Moisture Barriers on Polymer Films. *J. Vac. Sci. Technol. A Vacuum, Surfaces, Film.* **2012**, *30*, 021502.

(25)   Dickey, E.; Barrow, K. Single Sided Ultra-Barrier Oxide Films on Flexible Substrates , Deposited Using High Speed Atomic Layer Deposition Based on Substrate Translation. In *54th Annual Technical Conference Proceedings*; Society of Vacuum Coaters: Chicago, 2011; pp 70–75.

(26)   Yersak, A.; Lee, Y.-C.; Spencer, J.; Groner, M. Atmospheric Pressure Spatial Atomic Layer Deposition Web Coating with in Situ Monitoring of Film Thickness. *J. Vac. Sci. Technol., A* **2014**, *32*, 01A130.

(27)   Zhang, Y. ALD Enabled Wafer Level Polymer Packaging for MEMS, Univeristy of Colorado, 2011.

(28)   Kang, S.-K.; Hwang, S.-W.; Cheng, H.; Yu, S.; Kim, B.; Kim, J.-H.; Huang, Y.; Rogers, J. Dissolution Behaviors and Applications of Silicon Oxides and Nitrides in Transient Electronics. *Adv. Funct. Mater.* **2014**, *24*, 4427–4434.

(29)   Correa, G.; Bao, B.; Strandwitz, N. Chemical Stability of Titania and Alumina Thin Films Formed by Atomic Layer Deposition. *ACS Appl. Mater. Interfaces* **2015**, 14816–14820.

(30)   Cleveland, C.; Moghaddam, S.; Orazem, M. Nanometer-Scale Corrosion of Copper in De-Aerated Deionized Water. *J. Electrochem. Soc.* **2013**, *161*, C107–C114.

(31)   Mohammed, H. A.; Bhaskaran, G.; Shuaib, N. H.; Saidur, R. Heat Transfer and Fluid Flow Characteristics in Microchannels Heat Exchanger Using Nanofluids: A Review. *Renew. Sustain. Energy Rev.* **2011**, *15*, 1502–1512.

(32)   Li, C.; Wang, Z.; Wang, P. I.; Peles, Y.; Koratkar, N.; Peterson, G. P. Nanostructured Copper Interfaces for Enhanced Boiling. *Small* **2008**, *4*, 1084–1088.

(33)   Ju, Y. S.; Kaviany, M.; Nam, Y.; Sharratt, S.; Hwang, G. S.; Catton, I.; Fleming, E.; Dussinger, P. Planar Vapor Chamber with Hybrid Evaporator Wicks for the Thermal

Management of High-Heat-Flux and High-Power Optoelectronic Devices. *Int. J. Heat Mass Transf.* **2013**, *60*, 163–169.

(34) Kim, H.; Lee, H.-B.-R.; Maeng, W.-J. Applications of Atomic Layer Deposition to Nanofabrication and Emerging Nanodevices. *Thin Solid Films* **2009**, *517*, 2563–2580.

(35) Munoz-Rojas, D.; MacManus-Driscoll, J. Spatial Atmospheric Atomic Layer Deposition: A New Laboratory and Industrial Tool for Low-Cost Photovoltaics. *Mater. Horizons* **2014**, *1*, 314–320.

(36) Poodt, P.; Cameron, D.; Dickey, E.; George, S.; Kuznetsov, V.; Parsons, G. N.; Roozeboom, F.; Sundaram, G.; Vermeer, A. Spatial Atomic Layer Deposition: A Route towards Further Industrialization of Atomic Layer Deposition. *J. Vac. Sci. Technol., A* **2012**, *30*, 010802.

(37) George, S. M. Atomic Layer Deposition: An Overview. *Chem. Rev.* **2010**, *110*, 111–131.

(38) Zhang, Y.; Seghete, D.; Abdulagatov, A.; Gibbs, Z.; Cavanagh, A.; Yang, R.; George, S.; Lee, Y. C. Investigation of the Defect Density in Ultra-Thin Al_2O_3 Films Grown Using Atomic Layer Deposition. *Surf. Coatings Technol.* **2011**, *205*, 3334–3339.

(39) George, S. M.; Ott, a. W.; Klaus, J. W. Surface Chemistry for Atomic Layer Growth. *J. Phys. Chem.* **1996**, 31, 13121–13131.

(40) Ritala, M.; Leskelä, M.; Dekker, J.; Mutsaers, C.; Soininen, P. J.; Skarp, J. Perfectly Conformal TiN and Al_2O_3 Films Deposited by Atomic Layer Deposition. *Chem. Vap. Depos.* **1999**, *5*, 7–9.

(41) Wilson, C.; Grubbs, R.; George, S. Nucleation and Growth during Al_2O_3 Atomic Layer Deposition on Polymers. *Chem. Mater.* **2005**, *17*, 5625–5634.

(42) Levy, D.; Nelson, S.; Freeman, D. Oxide Electronics by Spatial Atomic Layer Deposition.

J. Disp. Technol. **2009**, *5*, 484–494.

(43) Levy, D.; Freeman, D.; Nelson, S.; Cowdery-Corvan, P.; Irving, L. Stable ZnO Thin Film Transistors by Fast Open Air Atomic Layer Deposition. *Appl. Phys. Lett.* **2008**, *92*, 90–92.

(44) Fitzpatrick, R.; Gibbs, Z.; George, S. Evaluating Operating Conditions for Continuous Atmospheric Atomic Layer Deposition Using a Multiple Slit Gas Source Head. *J. Vac. Sci. Technol. A Vacuum, Surfaces, Film.* **2012**, *30*, 01A136.

(45) Muñoz-Rojas, D.; Sun, H.; Iza, D.; Weickert, J.; Chen, L.; Wang, H.; Schmidt-Mende, L.; MacManus-Driscoll, J. High-Speed Atmospheric Atomic Layer Deposition of Ultra Thin Amorphous TiO_2 Blocking Layers at 100°C for Inverted Bulk Heterojunction Solar Cells. *Prog. Photovolt Res. Appl.* **2013**, *21*, 393–400.

(46) Lecordier; Dalberth; Sershen; Ruffo; Coutu; Sundaram; Becker. Design Iterations and Process Optimization of a Spatial ALD System, for High Throughput Roll-to-Roll Applications. In *12th International Conference on Atomic Layer Deposition Deposition*; American Vacuum Society: Dresden, 2012; p 68.

(47) Poodt, P.; Illiberi, A.; Roozeboom, F. The Kinetics of Low-Temperature Spatial Atomic Layer Deposition of Aluminum Oxide. *Thin Solid Films* **2013**, *532*, 22–25.

(48) Poodt, P.; Knaapen, R.; Illiberi, A.; Roozeboom, F.; Asten, A. Low Temperature and Roll-to-Roll Spatial Atomic Layer Deposition for Flexible Electronics. *J. Vac. Sci. Technol. A Vacuum, Surfaces, Film.* **2012**, *30*, 01A142.

(49) Poodt, P.; Kniknie, B.; Branca, A.; Winands, H.; Roozeboom, F. Patterned Deposition by Plasma Enhanced Spatial Atomic Layer Deposition. *Phys. Status Solidi - Rapid Res. Lett.* **2011**, *5*, 165–167.

(50) Poodt, P.; Lankhorst, A.; Roozeboom, F.; Spee, K.; Maas, D.; Vermeer, A. High-Speed

Spatial Atomic-Layer Deposition of Aluminum Oxide Layers for Solar Cell Passivation. *Adv. Mater.* **2010**, *22*, 3564–3567.

(51) Poodt, P.; Tiba, V.; Werner, F.; Schmidt, J.; Vermeer, A.; Roozeboom, F. Ultrafast Atomic Layer Deposition of Alumina Layers for Solar Cell Passivation. *J. Electrochem. Soc.* **2011**, *158*, H937.

(52) Suh, S.; Park, S.; Lim, H.; Choi, Y.-J.; Hwang, C.; Kim, H.; Won, S.-J. Investigation on Spatially Separated Atomic Layer Deposition by Gas Flow Simulation and Depositing Al_2O_3 Films. *J. Vac. Sci. Technol. A Vacuum, Surfaces, Film.* **2012**, *30*, 051504.

(53) Maydannik, P.; Kääriäinen, T.; Cameron, D. An Atomic Layer Deposition Process for Moving Flexible Substrates. *Chem. Eng. J.* **2011**, *171*, 345–349.

(54) Maydannik, P.; Kaariainen, T.; Cameron, D. Continuous Atomic Layer Deposition: Explanation for Anomalous Growth Rate Effects. *J. Vac. Sci. Technol. A* **2012**, *30*, 01A122.

(55) Maydannik, P.; Kääriäinen, T.; Lahtinen, K. An Industrial Scale Roll-to-Roll Atomic Layer Deposition Process for Coating Flexible Web Substrates. In *AVS 13th International Conference on Atomic Layer Deposition*; American Vacuum Society: San Diego, 2013.

(56) Sharma, K.; Hall, R.; George, S. Spatial Atomic Layer Deposition on Flexible Substrates Using a Modular Rotating Cylinder Reactor. *J. Vac. Sci. Technol. A Vacuum, Surfaces, Film.* **2015**, *33*, 01A132.

(57) Lahtinen, K.; Lahti, J.; Johansson, P.; Seppänen, T.; Cameron, D. C. Influence of Substrate Contamination, Web Handling, and Pretreatments on the Barrier Performance of Aluminum Oxide Atomic Layer-Deposited BOPP Film. *J. Coatings Technol. Res.* **2014**, *11*, 775–784.

(58)   Klumbies, H.; Schmidt, P.; Hähnel, M.; Singh, A.; Schroeder, U.; Richter, C.; Mikolajick, T.; Hoßbach, C.; Albert, M.; Bartha, J. W.; Leo, K.; Müller-Meskamp, L. Thickness Dependent Barrier Performance of Permeation Barriers Made from Atomic Layer Deposited Alumina for Organic Devices. *Org. Electron. physics, Mater. Appl.* **2015**, *17*, 138–143.

(59)   Fahlteich, J.; Mogck, S.; Wanski, T.; Schiller, N.; Amberg-schwab, S.; Weber, U.; Miesbauer, O.; Noller, K.; Boeffel, C. The Role of Defects in Single- and Multi- Layer Barriers for Flexible Electronics. In *Society of Vacuum Coaters 57th Technical Conference Proceedings*; 2014; pp 36–43.

(60)   Hirvikorpi, T.; Laine, R.; Nissi, M.; Kilpi, V.; Salo, E.; Li, W.; Lindfors, S.; Vartiainen, J.; Kentt, E.; Nikkolä, J.; Harlin, A.; Kostamo, J. Barrier Properties of Plastic Films Coated with an Al_2O_3 Layer by Roll-to-Toll Atomic Layer Deposition. *Thin Solid Films* **2014**, *550*, 164–169.

(61)   Mousa, M.; Oldham, C.; Jur, J.; Parsons, G. Effect of Temperature and Gas Velocity on Growth per Cycle during Al_2O_3 and ZnO Atomic Layer Deposition at Atmospheric Pressure. *J. Vac. Sci. Technol. A* **2012**, *30*, 01A155–01A155.

(62)   Schubert, S.; Klumbies, H.; Müller-Meskamp, L.; Leo, K. Electrical Calcium Test for Moisture Barrier Evaluation for Organic Devices. *Rev. Sci. Instrum.* **2011**, *82*.

(63)   Klumbies, H.; Müller-Meskamp, L.; Mönch, T.; Schubert, S.; Leo, K. The Influence of Laterally Inhomogeneous Corrosion on Electrical and Optical Calcium Moisture Barrier Characterization. *Rev. Sci. Instrum.* **2013**, *84*.

(64)   Sundgren, J.-E. A Review of the Present State of Art in Hard Coatings Grown from the Vapor Phase. *J. Vac. Sci. Technol. A Vacuum, Surfaces, Film.* **1986**, *4*, 2259.

(65)   Tsai, C. C.; Knights, J. C.; Chang, G.; Wacker, B. Film Formation Mechanisms in the

         Plasma Deposition of Hydrogenated Amorphous Silicon. *J. Appl. Phys.* **1986**, *59*, 2998–

         3001.

(66)   Wuu, D.-S.; Chen, T.-N.; Wu, C.-C.; Chiang, C.-C.; Chen, Y.-P.; Horng, R.-H.; Juang, F.-

         S. Transparent Barrier Coatings for Flexible Organic Light-Emitting Diode Applications.

         Chem. Vap. Depos. **2006**, *12*, 220–224.

(67)   Knaapen, R. Equipment for Atmospheric, Spatial Atomic Layer Deposition in Roll-to-

         Roll Processes. *30th ASPE Annu. Meet.* **2015**, 1–24.

(68)   Kim, H.-K.; Cho, C.-K. Transparent SiON/Ag/SiON Multilayer Passivation Grown on a

         Flexible Polyethersulfone Substrate Using a Continuous Roll-to-Roll Sputtering System.

         Nanoscale Res. Lett. **2012**, *7*, 69.

(69)   Abdulagatov, A. I.; Yan, Y.; Cooper, J. R.; Zhang, Y.; Gibbs, Z. M.; Cavanagh, A. S.;

         Yang, R. G.; Lee, Y. C.; George, S. M. Al_2O_3 and TiO_2 Atomic Layer Deposition on

         Copper for Water Corrosion Resistance. *ACS Appl. Mater. Interfaces* **2011**, *3*, 4593–4601.

(70)   Leplan, H.; Robic, J. Y.; Pauleau, Y. Kinetics of Residual Stress Evolution in Evaporated

         Silicon Dioxide Films Exposed to Room Air. *J. Appl. Phys.* **1996**, *79*, 6926–6931.

(71)   Sammelselg, V.; Netšipailo, I.; Aidla, A.; Tarre, A.; Aarik, L.; Asari, J.; Ritslaid, P.;

         Aarik, J. Chemical Resistance of Thin Film Materials Based on Metal Oxides Grown by

         Atomic Layer Deposition. *Thin Solid Films* **2013**, *542*, 219–224.

(72)   Zarzycki, J. Glass Structure. *J. Non. Cryst. Solids* **1982**, *52* (1-3), 31–43.

(73)   Suntola, T.; Anston, J. Method for Producing Compound Thin Films. 4058430, November

         15, 1977.

(74)   Illiberi, A.; Roozeboom, F.; Poodt, P. Spatial Atomic Layer Deposition of Zinc Oxide

Thin Films. *ACS Appl. Mater. Interfaces* **2012**, *4*, 268–272.

(75) Baumert, E.; Pierron, O. Fatigue Properties of Atomic-Layer-Deposited Alumina Ultra-Barriers and Their Implications for the Reliability of Flexible Organic Electronics. *Appl. Phys. Lett.* **2012**, *101*.

(76) Elam, J.; Groner, M.; George, S. Viscous Flow Reactor with Quartz Crystal Microbalance for Thin Film Growth by Atomic Layer Deposition. *Rev. Sci. Instrum.* **2002**, *73*, 2981.

(77) Carcia, P.; McLean, R.; Li, Z.; Reilly, M.; Marshall, W. Permeability and Corrosion in ZrO2/Al2O3 Nanolaminate and Al2O3 Thin Films Grown by Atomic Layer Deposition on Polymers. *J. Vac. Sci. Technol. A Vacuum, Surfaces, Film.* **2012**, *30*, 041515.

(78) Paracchino, A.; Mathews, N.; Hisatomi, T.; Stefik, M.; Tilley, S. D.; Grätzel, M. Ultrathin Films on Copper(i) Oxide Water Splitting Photocathodes: A Study on Performance and Stability. *Energy Environ. Sci.* **2012**, *5*, 8673.

(79) Minton, T.; Wu, B.; Zhang, J.; Lindholm, N.; Abdulagatov, A.; O'Patchen, J.; George, S.; Groner, M. Protecting Polymers in Space with Atomic Layer Deposition Coatings. *ACS Appl. Mater. Interfaces* **2010**, *2*, 2515–2520.

(80) Shan, C.; Hou, X.; Choy, K.-L. Corrosion Resistance of TiO2 Films Grown on Stainless Steel by Atomic Layer Deposition. *Surf. Coatings Technol.* **2008**, *202*, 2399–2402.

(81) Meléndez-Ceballos, A.; Fernández-Valverde, S.; Barrera-Díaz, C.; Albin, V.; Lair, V.; Ringuedé, A.; Cassir, M. TiO2 Protective Coating Processed by Atomic Layer Deposition for the Improvement of MCFC Cathode. *Int. J. Hydrogen Energy* **2013**, *38*, 13443–13452.

(82) Spahr, H.; Bülow, T.; Nowak, C.; Hirschberg, F.; Reinker, J.; Hamwi, S.; Johannes, H.-H.; Kowalsky, W. Impact of Morphological Defects on the Electrical Breakdown of Ultra Thin Atomic Layer Deposition Processed Al2O3 Layers. *Thin Solid Films* **2013**, *534*, 172–

176.

(83)   Hyoungsub, K.; McIntyre, P. Atomic Layer Deposition of Ultrathin Metal-Oxide Films for Nano-Scale Device Applications. *J. Korean Phys. Soc.* **2006**, *48*, 5.

(84)   Qi, L.; Zhang, C.; Chen, Q. Properties of Plasma Enhanced Chemical Vapor Deposition Barrier Coatings and Encapsulated Polymer Solar Cells. *Plasma Sci. Technol.* **2014**, *16*, 45–49.

(85)   Li, Y.-S.; Tsai, C.-H.; Kao, S.-H.; Wu, I.-W.; Chen, J.-Z.; Wu, C.-I.; Lin, C.-F.; Cheng, I.-C. Single-Layer Organic–inorganic-Hybrid Thin-Film Encapsulation for Organic Solar Cells. *J. Phys. D. Appl. Phys.* **2013**, *46*, 435502.

(86)   Fahlteich, J.; Fahland, M.; Schönberger, W.; Schiller, N. Permeation Barrier Properties of Thin Oxide Films on Flexible Polymer Substrates. *Thin Solid Films* **2009**, *517*, 3075–3080.

(87)   Choi, J.; Kim, Y.; Park, Y.; Huh, J.; Ju, B.; Kim, I.; Hwang, H. Evaluation of Gas Permeation Barrier Properties Using Electrical Measurements of Calcium Degradation. *Rev. Sci. Instrum.* **2007**, *78*.

(88)   Zhang, Y.; Bertrand, J. A.; Yang, R.; George, S. M.; Lee, Y. C. Electroplating to Visualize Defects in Al2O3 Thin Films Grown Using Atomic Layer Deposition. *Thin Solid Films* **2009**, *517*, 3269–3272.

(89)   Ripley, B. *Spatial Statistics*; Wiley: Hoboken, 1981.

(90)   Stapper, C. H. On Yield, Fault Distributions, and Clustering of Particles. *IBM J. Res. Dev.* **1986**, *30*, 326–338.

(91)   Hess, C.; Weiland, L. Extraction of Wafer-Level Defect Density Distributions to Improve Yield Prediction. *IEEE Trans. Semicond. Manuf.* **1999**, *12*, 175–183.

(92)   Sato, H.; Ikota, M.; Sugimoto, A.; Masuda, H. A New Defect Distribution Metrology with a Consistent Discrete Exponential Formula and Its Applications. *IEEE Trans. Semicond. Manuf.* **1999**, *12*, 409–418.

(93)   Pagilla, P. R. *R2R ALD / MLD : Machine & Transport Behavior R2R Modular Machine Details*; 2015.

(94)   Zhang, Y.; Zhang, Y.-Z.; Miller, D.; Bertrand, J.; Jen, S.-H.; Yang, R.; Dunn, M.; George, S.; Lee, Y.-C. Fluorescent Tags to Visualize Defects in Al_2O_3 Thin Films Grown Using Atomic Layer Deposition. *Thin Solid Films* **2009**, *517*, 6794–6797.

(95)   Statistical Toolbox. The Mathworks, Inc.: Natick 2014.

(96)   Lewis, R.; Liew, L.-A.; Xu, S.; Lee, Y.-C.; Yang, R. Microfabricated Ultra-Thin All-Polymer Thermal Ground Planes. *Sci. Bull.* **2015**, *60*, 701–706.

(97)   Oshman, C.; Li, Q.; Liew, L.-A.; Yang, R.; Bright, V.; Lee, Y.-C. Flat Flexible Polymer Heat Pipes. *J. Micromechanics Microengineering* **2013**, *23*, 015001.

(98)   Lewis, R. Personal Communication. 2015.

(99)   Hoivik, N.; Elam, J.; Linderman, R.; Bright, V.; George, S.; Lee, Y.-C. Atomic Layer Deposited Protective Coatings for Micro-Electromechanical Systems. *Sens. Actuators, A* **2003**, *103*, 100–108.

(100) Zhou, W.; Dai, X.; Fu, T.-M.; Xie, C.; Liu, J.; Lieber, C. Long Term Stability of Nanowire Nanoelectronics in Physiological Environments. *Nano Lett. 2014* **2014**, *14*, 1614–1619.

(101) Li, D.; Abdulagatov, A.; Yang, F.; Zhang, D. C. Atomic Layer Deposited Protective Coatings for Integrated MEMS Flow Sensor. In *2012 7th IEEE International Conference on Nano/Micro Engineered and Molecular Systems, NEMS 2012*; IEEE: Kyoto, 2012; pp

747–750.

(102) Matero, R.; Ritala, M.; Leskelä, M.; Salo, T.; Aromaa, J.; Forsén, O. Atomic Layer Deposited Thin Films for Corrosion Protection. *J. Phys. IV* **1999**, *9*, 493–499.

(103) Marin, E.; Lanzutti, A.; Paussa, L.; Guzman, L.; Fedrizzi, L. Long Term Performance of Atomic Layer Deposition Coatings for Corrosion Protection of Stainless Steel. *Mater. Corros.* **2015**, *66*, 907–914.

(104) Marin, E.; Guzman, L.; Lanzutti, A.; Ensinger, W.; Fedrizzi, L. Multilayer Al_2O_3/TiO_2 Atomic Layer Deposition Coatings for the Corrosion Protection of Stainless Steel. *Thin Solid Films* **2012**, *522*, 283–288.

(105) Díaz, B.; Härkönen, E.; Światowska, J.; Maurice, V.; Seyeux, A.; Marcus, P.; Ritala, M. Low-Temperature Atomic Layer Deposition of Al_2O_3 Thin Coatings for Corrosion Protection of Steel: Surface and Electrochemical Analysis. *Corros. Sci.* **2011**, *53*, 2168–2175.

(106) WCS 500 Web Coating System for Roll-to-Roll ALD www.beneq.com (accessed Jun 15, 2016).

(107) Putkonen, M.; Bosund, M.; Ylivaara, O.; Puurunen, R.; Kilpi, L.; Ronkainen, H.; Sintonen, S.; Ali, S.; Lipsanen, H.; Liu, X.; Haimi, E.; Hannula, S.-P.; Sajavaara, T.; Buchanan, I.; Karwacki, E.; Vähä-Nissi, M. Thermal and Plasma Enhanced Atomic Layer Deposition of SiO_2 Using Commercial Silicon Precursors. *Thin Solid Films* **2014**, *558*, 93–98.

(108) Budini, N.; Rinaldi, P.; Schmidt, J.; Arce, R.; Buitrago, R. Influence of Microstructure and Hydrogen Concentration on Amorphous Silicon Crystallization. *Thin Solid Films* **2010**, *518*, 5349–5354.

(109) Icenhower, J. P.; Dove, P. M. The Dissolution Kinetics of Amorphous Silica into Sodium Chloride Solutions : Effects of Temperature and Ionic Strength. *Geochim. Cosmochim. Acta* **2000**, *64*, 4193–4203.

(110) Punckt, C.; Aksay, I. Dissolution Dynamics of Thin Films Measured by Optical Reflectance. *J. Chem. Phys.* **2009**, *131*, 1–5.

(111) Taking the mystery out of thin-film measurement www.fimetrics.com (accessed Jun 16, 2016).

(112) Yang, J.; Zhang, D.; Li, Y. How to Remove the Influence of Trace Water from the Absorption Spectra of SWNTs Dispersed in Ionic Liquids. *Beilstein J. Nanotechnol.* **2011**, *2*, 653–658.

(113) Bash, E. Defects in Amorphous SiO2: Reactions, Dynamics and Optical Properties, Vanderbilt University, 2012.

(114) Daey Ouwens J; Schropp, R. E. I.; Ouwens, J. D. Hydrogen Microstructure in Hydrogenated Amorphous Silicon. *Phys. Rev. B. Condens. Matter* **1996**, *54*, 17759–17762.

(115) Tanemura, T.; Sato, S.; Kundu, M.; Yamada, C.; Murata, Y. Growth of Single-Crystal SiO 2 Clusters on Si(001) Surface. *J. Appl. Phys.* **2009**, *105*, 074310.

(116) Kundu, M.; Murata, Y. Growth of Single-Crystal SiO 2 Film on Ni(111) Surface. *Appl. Phys. Lett.* **2002**, *80*, 1921–1923.

(117) Bettermann, P.; Liebau, F. The Transformation of Amorphous Silica to Crystalline Silica under Hydrothermal Conditions. *Contrib. Miner. Pet.* **1975**, *53*, 25–36.

(118) Mazer, J.; Walther, J. Dissolution Kinetics of Silica Glass as a Function of pH between 40 and 85°C. *J. Non-Cryst. Solids* **1994**, *170*, 32–45.

(119) Herrmann, M. Corrosion of Silicon Nitride Materials in Aqueous Solutions. *J. Am. Ceram. Soc.* **2013**, *96*, 3009–3022.

(120) Wang, Y.-Y.; Shen, H.-J.; Bai, Y.; Tang, Y.-D.; Liu, K.-A.; Li, C.-Z.; Liu, X.-Y. Influences of High-Temperature Annealing on Atomic Layer Deposited Al 2 O 3 /4H-SiC. *Chinese Phys. B* **2013**, *22*, 078102.

(121) Freij, S. J.; Parkinson, G. M.; Reyhani, M. M. Atomic Force Microscopy Study of the Growth Mechanism of Gibbsite Crystals. *Phys. Chem. Chem. Phys.* **2004**, *6*, 1049–1055.